Aminophosphines as Precursors for Doped and Phase Pure Metal Phosphide Nanocrystals: Synthesis Beyond $P(SiMe_3)_3$

Marja Elizabeth Mundy

A dissertation

submitted in partial fulfillment of the

requirements for the degree of

Doctor of Philosophy

University of Washington

2020

Reading Committee:

Brandi M. Cossairt, Chair

Daniel R. Gamelin

D. Michael Heinekey

Program Authorized to Offer Degree:

Chemistry

University of Washington

Abstract

Aminophosphines as Precursors for Doped and Phase Pure Metal Phosphide Nanocrystals: Synthesis Beyond $P(SiMe_3)_3$

Marja Elizabeth Mundy

Chair of the Supervisory Committee:
Associate Professor Brandi M. Cossairt
Chemistry

Colloidal metal phosphide nanocrystals represent attractive synthetic targets for researchers. They exemplify the diversity of emergent properties presented by nanomaterials, as the class encompasses both semiconductors and metals. When quantum confinement is accounted for, nanoscale semiconducting metal phosphides have optical properties that span the visible and NIR range of the spectrum, making them suitable for a wide range of applications. The metallic transition metal phosphides are consistently touted as earth-abundant alternatives for the hydrogen evolution reaction with competitive catalytic activity, particularly in the form of high surface area nanoparticles.

Transition metal phosphides are plagued by synthetic challenges. The reactions are either multistep with low yields, require high temperatures and extended reaction times, or produce

mixtures of crystalline phases. While high quality syntheses of several semiconducting metal phosphides exist, many are either capable of only producing nanocrystals in one size or rely on incomplete reactions for size tunability. Recent and exciting work synthesizing indium phosphide from aminophosphines demonstrated precursor-dependent size control based on the indium halide. Prior to the work discussed here, this reactivity was only known for indium phosphide. Chapter 2 discusses our efforts broadening the scope of aminophosphine-based nanocrystal synthesis to include II-V materials and transition metal phosphides. After establishing this versatile platform for the synthesis of phase-pure metal phosphides, Chapter 3 highlights research done establishing aminophosphine-derived InP as a substrate for copper doping and spectroscopic analysis of surface treated materials.

TABLE OF CONTENTS

List of Figures iii

List of Tables viii

Chapter 1. Introduction 1

1.1 Colloidal nanocrystals and their applications 1

1.2 Metal phosphide nanocrystal synthesis 2

1.3 Precursor-dependent size control in nanocrystal synthesis 5

1.4 Cation doping in nanocrystals 6

1.5 References 10

Chapter 2. Aminophosphines as Versatile Precursors for the Synthesis of Metal Phosphide Nanocrystals 14

2.1 Note regarding collaborator contributions 14

2.2 Introduction 14

2.3 Results and Discussion 15

2.3.1 Synthesis and Characterization of II-V materials 16

2.3.2 Synthesis and Characterization of Transition Metal Phosphides 21

2.3.3 Reactivity for HER and Proton Transfer 27

2.4 Conclusions 30

2.5 Experimental methods 30

2.5.1 Synthentic methods and basic sample preparation 31

2.5.2 X-ray absorption measurements 32

2.5.3 Electrochemical characterization 33

2.6 References 35

Chapter 3. Synthesis and Spectroscopy of Emissive, Surface-Modified, Copper-Doped Indium Phosphide Nanocrystals 38

3.1 Note regarding collaborator contributions 38

3.2 Introduction 38

3.3 Results and Discussion 40

3.3.1 Synthesis of Cu^{+}:InP 41

3.3.2 Post-synthetic modifications of doped NCs 46

3.3.3 Photophysical characterizations 53

3.4 Conclusions 56

3.5 Experimental Details 56

3.6 References 59

Appendix A: Attempts at the synthesis of InPZnE quaternary alloyed nanocrystals 63

LIST OF FIGURES

Figure 1.1. Model of a binary semiconducting nanocrystal surrounded by long-chain ligands stabilizing the surface. Reprinted from reference 5 with permission.[5] 2

Figure 1.2. Proposed mechanism showing the formation of InP from aminophosphines and indium chloride. Figure modified from reference 17.[17] 4

Figure 1.3. Highly monodisperse PbS nanocrystals with size dictated by the reactivity of the thiourea. Reprinted with permission from reference 25.[25] 5

Figure 1.4. General schematics of synthetic approaches to nanocrystal doping with E representing ion exchange within the previously formed lattice.[33] 8

Figure 2.1. Standard reaction scheme for metal phosphide nanocrystal formation. 16

Figure 2.2. A) TEM image (6.8 ± 0.5 nm), (B) UV-Vis spectrum, and (C) XRD pattern of Cd_3P_2 nanocrystals prepared at 250 °C from $CdCl_2$ using a 1:3.6 ratio of Cd:P (Cd_3P_2 reference pattern PDF 01-070-3099 47-1443). D) TEM image of Cd_3P_2 prepared from $CdCl_2$ at 250 °C using a 1:1.3 ratio of Cd:P (7.5 ± 0.3 nm). 17

Figure 2.3. (A) UV-Vis final traces of materials synthesized from CdX_2 precursors. (B) XRD spectra of materials showing two populations of particles including one subset with a crystalline domain size >30 nm, consistent with mild heterogeneity observed in synthesis. TEM images of (C) $CdBr_2$ (5.9 ± 0.7 nm) and (D) CdI_2 (5.6 ± 0.5) products showing the expected trend towards smaller nanocrystals as the halide becomes a better leaving group. 18

Figure 2.4. Synthesis of Zn_3P_2 from ZnX_2 (X = Cl, Br, I) and $P(NEt_2)_3$ at 250°C. (a) Representative UV-Vis absorbance spectra of the final products normalized at 400 nm. Inset: TEM of product from $ZnCl_2$ and $P(NEt_2)_3$. (b) Air-free powder X-ray diffraction data of the purified products with Zn_3P_2 reference pattern (PDF 01-071-6507). 20

Figure 2.5. 202.4 MHz ^{31}P NMR of reaction aliquots in C_6D_6 with a triphenylphosphine internal standard: (A) Zn_3P_2 synthesis at 250°C. (B) Cd_3P_2 synthesis at 250°C. 21

Figure 2.6. (A, B) TEM images (A: CoP 7.8 ± 0.7 nm; B: Co_2P of various morphologies with widths/diameters of 6.5 ± 0.6 nm) and (C) XRD pattern of CoP and Co_2P prepared at 250

°C and 200 °C, respectively. CoP (PDF 01-089-2598 29-497) and Co_2P (PDF 01-070-8358) reference patterns. The inset in figure (A) shows a zoomed in image of a single CoP nanocrystal with the corresponding FFT. 22

Figure 2.7. Synthesis of cobalt phosphides from CoI_2 at 250 °C. Powder X-ray diffraction data of products after different reaction times, showing the conversion from Co_2P to CoP with primary peaks of CoP (PDF 01-089-2598 29-497) and Co_2P (PDF 01-070-8358) from reference patterns. Reactions allowed to proceed for 30 minutes or less show a mixture of both phases. After two hours the material is now exclusively CoP. 23

Figure 2.8. XANES spectra for the synthesized CoP and Co_2P, $CoCl_2$ and Co metal commercial standards, and CoP produced by an established literature procedure.[4] The CoP species exhibits several characteristic spectral features. Specifically, inflection points on the rising edge of the CoP spectra are observed at approximately 7709.75 eV and 7715.75 eV. These same features are considerably lower in energy at 7709.0 eV and 7714.0 eV in the nominal Co_2P phase. While an empirical standard was not readily available for comparison to Co_2P, the shift of the shoulders on the rising edge to lower energy generally indicates a more reduced cobalt oxidation state.[30] 25

Figure 2.9. (A) P-XRD of scaled up reaction pre- and post-annealing for 7 hours with CoP (PDF 01-089-2598 29-497) and Co_2P (PDF 01-070-8358) reference patterns. The diffraction peaks in the annealed sample correspond exclusively to CoP, while a mixture of CoP and Co_2P is present in the as-synthesized sample. 26

Figure 2.10. (A) P-XRD of reaction of $NiCl_2$ with $P(NEt_2)_3$ at 250 °C with Ni_2P reference pattern (PDF 01-074-1385). (B) TEM of product showing nanocrystals of 8.2 ± 1.6 nm. .. 27

Figure 2.11. Linear sweep voltammograms at 5mV/s of the TMPs with I mg/cm^2 loadings annealed at 450 °C under a flow of 5%H_2/95% N_2 on carbon fiber electrodes in 0.5 M H_2SO_4 using a graphite counter electrode and a Ag/Ag_2SO_4 reference electrode. All materials demonstrate electrocatalytic activity, with Co_2P exhibiting the lowest overpotential. 29

Figure 3.1. (Left) P-XRD spectrum of product of reaction of $P(NEt_2)_3$ and $CuCl_2$ (orange) with Cu_3P standard pattern (blue, pdf 01-071-2261 ICSD) and (right) TEM image showing clear evidence of crystalline copper phosphide. 40

Figure 3.2. Reaction scheme for bottom-up Cu^+:InP synthesis. 41
Figure 3.3. A) TEM image of Cu^+:InP NCs derived from aminophosphines and $InCl_3$ showing *d* = 3.2 ± 0.3 nm NCs. B) UV-Vis absorption spectra of reaction progress and final steady-state PL spectrum of representative synthesis of Cu^+:InP NCs (10% PLQY). C) Powder X-ray diffraction pattern of the same NCs showing the only crystalline phase present to be InP (pdf 01-070-2513 ICSD). D) Normalized steady-state PL spectra of copper-doped InP NCs synthesized with different halide precursors to tune the size of the NCs and resulting emission energy. 42
Figure 3.4. Photoluminescence excitation monitored at 825 nm. The feature at 585 nm corresponds to the excitonic absorbance in the UV-Vis spectrum shown in Figure 3.3B. 43
Figure 3.5. P-XRD spectrum (gray) of nanocrystals formed by reacting $InCl_3$ and $P(NEt_2)_3$ according to Scheme 1 and doped using $CuBr_2$ instead of $CuCl_2$ as the copper precursor. Reference bulk InP pattern (yellow, pdf 01-070-2513 ICSD). 45
Figure 3.6. TEM images of Cu^+:InP NCs synthesized from $InBr_3$ (left) and InI_3 (right). 46
Figure 3.7. Photoluminescence spectra of copper doped samples during standard Lewis acid treatment with zinc stearate (top) and using a modified ZnSeS shelling procedure (bottom). Both spectra show the emergence of excitonic luminescence below 600 nm. 47
Figure 3.8. TEM of zinc carboxylate treated Cu:InP NCs (left) and UV-Vis and final PL spectrum showing the continued presence of copper in the nanocrystal (right). 48
Figure 3.9. Photoluminescence spectra of Cu:InP NCs after cadmium oleate treatment at 200 °C (top) or 100 °C (bottom). 49
Figure 3.10. Absorption spectra of Cu^+:InP NCs thickly shelled *in-situ* with ZnSeS. The UV-Vis (top) shows the development of sub-band gap absorbance associated with the so-called "copper foot" and retention of the InP excitonic absorption while the PL spectra (bottom) show both the distinct copper luminescence and the presence of excitonic luminescence around 565 nm. 50
Figure 3.11. A) TEM of Cu^+:InP/ZnSe NCs showing *d* = 4.2 ± 0.4 nm NCs. B) UV-Vis absorption spectra of reaction progress and final steady-state PL spectrum of a representative synthesis of Cu^+:InP/ZnSe NCs (40% PLQY). C) Powder X-ray diffraction

pattern of the same NCs showing crystalline phase present to be primarily InP (pdf 01-070-2513 ICSD) with slight shifts towards ZnSe (pdf 01-071-5977 ICSD)..... 51
Figure 3.12. A) TEM Absorption and PL spectra collected during post-synthetic treatment of thickly shelled InP/ZnSeS NCs with a copper chloride and oleylamine solution at 210 °C for a period of 22 h. The UV-Vis absorption spectra (top) show the development of sub-band gap absorbance associated with the so-called “copper foot” while the PL spectra (bottom) show the diminishment of the excitonic luminescence and the emergence of the distinct copper luminescence. 52
Figure 3.13. Normalized PL decay dynamics of the copper PL for Cu^+:InP NCs (red), Cu^+:InP/Zn NCs (blue), and Cu^+:InP/ZnSe NCs (black). The inset shows the first 20 ns of data collected in a 100 ns window (Figure S10). All data were collected at room temperature on NCs suspended in dry toluene. The untreated Cu^+:InP NCs (red) show the fastest decay and have the lowest PLQY of 10%, followed by the Cu^+:InP/Zn (blue, PLQY of 20%), and finally the shelled Cu^+:InP/ZnSe NCs (black) show the longest lifetime and highest PLQY of 40%. PL decay curves were obtained by integrating between 880 and 780 nm. 54
Figure A1. Color range comparison of traditional phosphors with quantum dot displays. Reprinted with permission from reference 3……..64
Figure A2. Nanocrystals formed from the two-injection Nanoco procedure modified to a laboratory scale, confirming validity of approach……..67
Figure A3. UV-Vis spectra of a typical (top) heat up using MSCs and (bottom) two injection (IJ) Nanoco reaction using individual molecular precursors…….69
Figure A4. Large, anisotropic nanostructures formed by heatup of InP MSCs and myristic acid. …….70
Figure A5. XRD patterns of quantum dots synthesized via the different methods. The shift in values of 2 theta suggests alloying of the materials. The lines are a visual aid and correspond to major InP peaks from reference bulk pattern (pdf 01-070-2513 ICSD). The ZnS reference pattern is pdf 01-071-5976 ICSD…….71
Figure A6. TEM images of particles synthesized with A) decreased and B) increased amounts of $[Zn_{10}S_4(SPh)_{16}][N(Me)_4]_4$……73

Figure A7. Nanostructures formed by slow addition of $P(SiMe_3)_3$ to zinc, selenium, and indium precursors with selenium source A)TOPSe and B) **)** N-butyl-N'-cyclohexylselenourea. ……..77

LIST OF TABLES

Table 2.1. Overpotentials for materials under reported conditions. The lowest overpotential is seen for Co_2P annealed on titanium, but the Meerwein's treatment produces competitive activities under significantly milder conditions. 28

Table 3.2. ICP-OES elemental ratios of nanocrystals formed under various synthetic conditions. 44

Table 3.3. Fitting parameters for time resolved photoluminescence decay dynamics (fitting window of 1μs – Figure 3.13). 55

Table A4. Elemental ratios determined by ICP-AES for final materials generated from different InPZnS syntheses……71

Table A5. Characterization of final nanocrystal products synthesized via a heat up method from different selenium precursors…….75

Table A6. Selenium content of final nanomaterials synthesized via a slow injection of $P(SiMe_3)_3$ and various selenium precursors…….76

ACKNOWLEDGEMENTS

So, here we are. The end of an era that's been more bittersweet than I expected. Before I started grad school, I imagined that my thesis would be an opus of some import, perhaps with a dash of genius. It's a bit more humble than I anticipated, but I'm so proud of it nonetheless.

There are many people who made this work possible that deserve my eternal gratitude. I'd like to start with my collaborators, without whom this would literally not exist. Thank you for doing the work that I couldn't and for being so good at it. To the Cossairt lab, y'all are the worst and without you my graduate experience would have been so much poorer. Thank you for your constant support, making me laugh until I cried, and saving me from innumerable stomachaches by eating my baked goods. I'm so fortunate to have found a home here and I know that I'll never find a group of coworkers that will hold a candle to you. I'd like to particularly thank Dr. Ben Glassy for teaching me how to be a good chemist and a better labmate. To David and Michael for going through it all with me, because boy did we have some times. Finally, to Madison, my mini-me, for being the best morning buddy, having a constant supply of adorable dog photos, and for really acting as my lifeline for the past few years.

The tone of the lab comes from the top, and I would be remiss not to thank Brandi for creating a space that's fostered this intense comradery and a sense of family. I didn't quite know what I was in for when I joined the lab of a third-year professor, but I've learned so much because of it. The road hasn't been easy, but Brandi has been a constant source of support and guidance. No matter what, she's always had my back and pushed me to do my best at whatever I wanted. We

had some growing pains and it wasn't always easy, but she is a remarkable advisor and I'm fortunate to have stumbled into this group. Brandi – thank you for never giving up on me, even when I had.

I'm lucky to have found a support system outside of lab. The Chemistry department has the best support staff at UW, who are not only great at their jobs, but they're great people too. I always know I can count on Diana, Kim, or Cathy to make literally anything happen or go down and hear Loch crack a joke and make me laugh on a rough day. I'm not sure if it's like this everywhere or we're just lucky here, but I'm grateful nonetheless. One of the best things I did during grad school was join WCS (now InCS) and the Ligand Fielders. WCS gave me opportunities, a community, and kept me connected with friends throughout the department. WCS was one of the reasons I came to UW and I'm so glad it exceeded my expectations. If I could give one piece of advice to future grad students, join a departmental IM team. Being on the Ligand Fielders was a highlight of my springs and summers and the most encouraging hour of my week. Plus the 3 championships didn't hurt (we do it for the t-shirt). I have some fantastic friends who've helped keep me grounded. To Erin, whose coffee dates I've sorely missed, and Kate, who I literally can't imagine my life without, thank you. To the many friends who've commiserated, offered encouragement, or offered tea – y'all are the best.

I wouldn't be where I am today without the unconditional love and support from my family. They've always been there to listen, give advice whether I wanted it or not, and let me know no matter what they'll always be there. I've reconnected with old and gained some new family during grad school and they've helped make the west coast feel like home. Thank you to the Lanimals, and Nolan, Sarah, Natalie, Alice, and Trevor for having me for Thanksgivings and always being there. Uncle Bill and Aunt Kathy have been the best givers of accurate, but tough to follow advice

and support from those who know that there's light at the end of the grad school tunnel. To Mummu, thank you for showing me the world and how to be a strong person. To my parents – I can't imagine having a better pair. You've joined me on this emotional roller-coaster ride and it can't have been easy. Thank you for putting up with me and ensuring that I know I always have a safe place with you. None of what I've done or achieved would be possible without your ever-present love and support.

Finally, to Cam. Meeting you was the best part of grad school. I don't think I can adequately thank you for everything you've done, but I'll try. Thank you for constantly cooking dinners, for telling me I'll get through this, and for making me laugh when things are hard. I cannot imagine having found a better partner and I can't wait to see what the future holds. Thank you for being my rock for almost 5 years and making my life better in so many ways.

Chapter 1. INTRODUCTION

1.1 COLLOIDAL NANOCRYSTALS AND THEIR APPLICATIONS

Colloidal nanocrystals have garnered significant scientific attention across a range of disciplines for their solution processability and emergent properties.[1,2] These properties allow nanomaterials to be central to the development of current and next-generation technologies from catalysis, to lighting, to quantum information. Nanoparticles are highly suited to use as catalysts because of their high surface area-to-volume ratio.[3] In heterogenous catalysis only sites on the surface of the material can be catalytically active as the internal atoms are inaccessible to substrate and generally fully coordinatively saturated.[4] Thus, morphologies with high surface area-to-volume ratios, like nanocrystals, have more active sites per mass catalyst when compared to a more traditional pristine film or crystalline wafer. Semiconducting nanocrystals, also known as quantum dots (QDs), have been studied for a wide range of emissive applications because of their narrow luminescence linewidths and size-tunable emission.[2] In semiconductor crystals smaller than the material's Bohr exciton radius, the band gap of a semiconductor becomes dependent on the crystal size, increasing as size decreases. A single material's optical features can therefore span hundreds of nanometers allowing the absorbance and emission to be tailored to specific wavelengths for an application by changing the QD size.

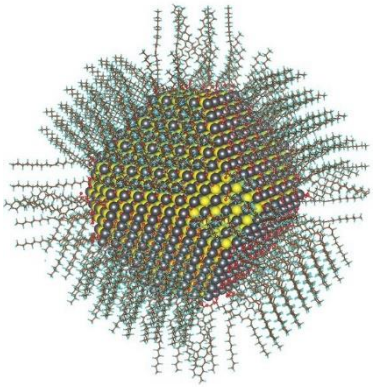

Figure 1.1. Model of a binary semiconducting nanocrystal surrounded by long-chain ligands stabilizing the surface. Reprinted from reference 5 with permission.[5]

1.2 METAL PHOSPHIDE NANOCRYSTAL SYNTHESIS

This work focuses on various metal phosphide nanocrystals, a wide class of nanomaterials united by the anionic phosphorous component, which commonly exhibit a high degree of covalency with the lattice cations.[6,7] This field has a rich history and has been well described in numerous publications.[8–11] Two major subclasses exist within the whole: metallic transition metal phosphides and semiconducting main group metal phosphides, such as III-Ps and II-Ps. The transition metal phosphides have received extensive attention as possible earth-abundant electrocatalysts for the hydrogen evolution reaction.[10] The semiconducting main group metal phosphides have optical features that span the visible and NIR range of the electromagnetic spectrum that coupled with their generally lower toxicity makes them of interest for applications ranging from phosphors in displays (InP) to photovoltaics (Zn_3P_2).[8,9] The synthesis of semiconducting metal phosphide nanocrystals generally involves the thermolysis of a highly reactive source of P^{3-}, such as PH_3 or $P(SiMe_3)_3$, and a metal precursor in non-coordinating solvent in the presence of long chain capping ligands.[12,13] They follow classical to semi-classical nucleation and growth steps with metal and phosphorus monomers directly bonding to form the

binary material in a single step. While several semiconducting metal phosphides have persistent cluster intermediates, these can be directly thermolyzed to generate larger nanoparticles. In contrast, TMP nanocrystal formation proceeds by two primary synthetic routes. First, and most prominently for cobalt phosphide, is a two-step process that starts with metallic nanocrystals that liberated phosphorus can diffuse into at very elevated temperatures in redox active conditions.[14] These syntheses are generally material, time, and energy intensive, making them challenging to scale up. Other TMPs can be synthesized directly from metal and phosphorus precursors, but the presence of multiple stable crystalline phases of different stoichiometries leads to problems of selectivity in terms of consistently forming a single material.[15]

Recent work demonstrated the utility of amino-pnictogen precursors for forming III-V and II-As nanocrystals, with the synthesis of InP from aminophosphines and indium halides being the most well-developed.[16–21] This synthesis has several advantages over the traditional thermolysis of $P(SiMe_3)_3$ as it allows for precursor-dependent size control of the final nanocrystal product and the use of non-pyrophoric phosphorus precursors. The reactions take place in a long-chain primary amine solvent that is involved in the initial step of generating the reactive phosphorus monomer via a transamination sequence as well as playing a role as a reducing agent in later steps of the mechanism proposed by the Hens group and seen in Figure 2.[17]

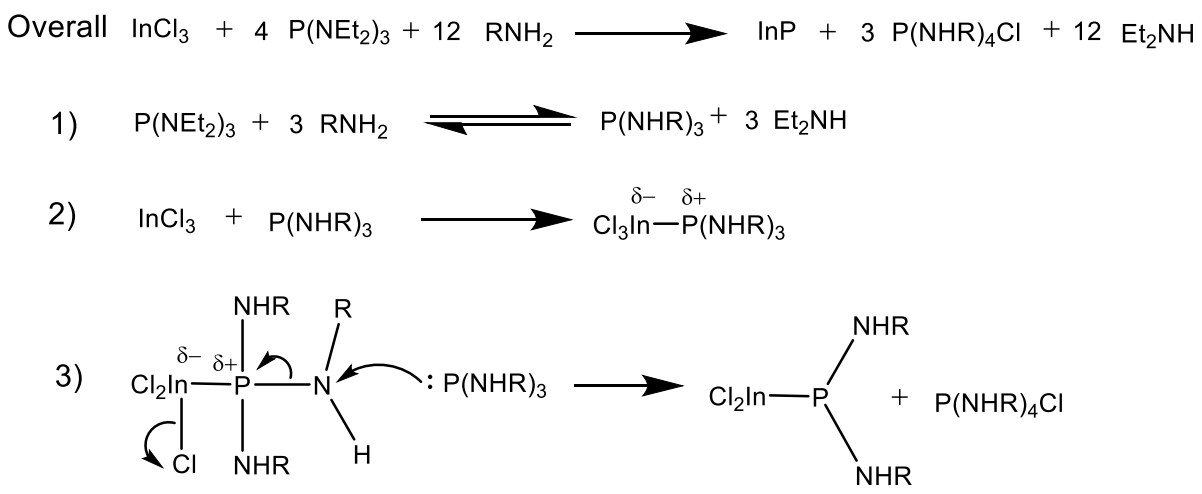

Figure 1.2. Proposed mechanism showing the formation of InP from aminophosphines and indium chloride. Figure modified from reference 17.[17]

The proposed mechanism involves the sacrificial self-reduction of the aminophosphine, which necessitates the use of excess phosphorus precursor. The exact nature of the mechanism has been debated in the literature, but this simplistic model suffices for broad comparative study.[18] This additionally excludes the large excess of $ZnCl_2$ present during nucleation, which has been theoretically modeled to assist in "activating" the transaminated aminophosphine and thus gate the reaction kinetics.[22] What is agreed in all cases is the necessity of excess aminophosphine and the importance of the long chain primary amine, generally oleylamine, to the synthesis. The presence of the type of high boiling point redox active solvent present in transition metal phosphide formation hints at the possibility of a single synthetic route to these diverse materials. While previously unproven, this aminophosphine-based reactivity and precursor-related tuning could provide a broadly applicable route to controllable synthesis of semiconducting main group and transition metal phosphides.

1.3 PRECURSOR-DEPENDENT SIZE CONTROL IN NANOCRYSTAL SYNTHESIS

A powerful ideological shift in synthetic development for nanocrystal chemistry has been the move toward systems exhibiting precursor-dependent control of size or composition.[23,24] A particularly beautiful example comes from the Owen group at Columbia, with their libraries of chalcogenoureas that give a wide range of nanocrystal sizes and compositions.[25–27] In these instances, as the nanocrystals form via a classical LaMer type nucleation and growth, altering the kinetics of monomer formation determines the number of nuclei and thus the final size of the nanocrystals at full completion. This approach is extremely material-efficient, as earlier syntheses obtained smaller sizes by simply halting the reaction prior to completion, wasting frequently expensive precursors. Another exciting direction stemming from the deep kinetic knowledge in the chalcogenourea system is the emergence of kinetically controlled alloyed nanostructures.[27] By strategically selecting chalcogenourea derivatives with similar or significantly different reactivities, cadmium seleno-sulfide alloys or heterostructures, respectively, were synthesized in a one-pot system rather than a multi-step or multi-injection process.

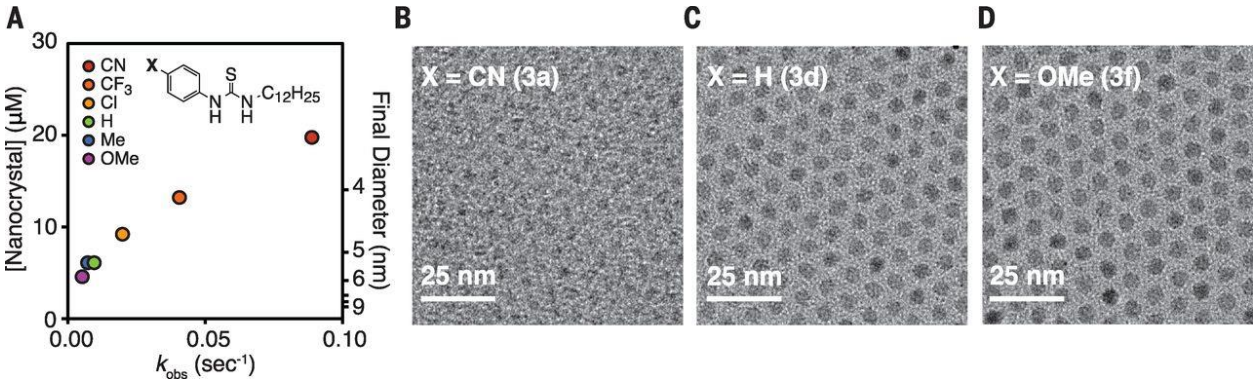

Figure 1.3. Highly monodisperse PbS nanocrystals with size dictated by the reactivity of the thiourea. Reprinted with permission from reference 25.[25]

For metal phosphides, the generally extreme reactivity of phosphorus precursors and non-classical nucleation kinetics of some materials has previously limited the approaches for precursor-dependent size tuning of nanocrystals.[28] The aminophosphine-based synthesis of indium phosphide relies on the differing reactivity of the indium halides to control the final QD size. This strategy succeeds where others failed for InP by utilizing different indium and phosphorus precursors to avoid the kinetically persistent cluster intermediates that prevent nanocrystals from forming via a simple classical nucleation process.[13,28–30] The hypothesized mechanism for monomer generation involves the formation of indium phosphorus bonds and the generation of a phosphonium halide byproduct, with the halide bonded to the indium acting as a leaving group.[17,18,22] The reactivity of the indium halide does correlate with the halide's facility as a leaving group, with the iodide the most reactive and chloride the least reactive.

1.4 CATION DOPING IN NANOCRYSTALS

In addition to phase pure materials, significant interest exists in developing routes for facile cationic doping of nanocrystal lattices.[31–33] Many of these cations possess interesting optical or magnetic properties when incorporated into a host lattice. For example, copper ions produce a characteristic photoluminescence spectrum that overlaps with the region of the spectrum where silicon efficiently absorbs light.[34] As such, these materials are of significant interest in the development of luminescent solar concentrators for combined use with silicon photovoltaics. Doping nanocrystals with functional cations has been well-studied in the relatively ionic chalcogenide materials, but the more covalent phosphides have proven more challenging .[6,35] This cannot be fully attributed to the general low solubility of many dopant ions in the III-V lattices as, for example, cadmium mobility is similar in order of magnitude within bulk InP and ZnSe lattices.[35–37] While diffusion in bulk semiconductors requires temperatures in excess of 500 ^{o}C, ion

diffusion in nanocrystals can be accessed at significantly lower temperatures, making these systems more amenable hosts.[38]

InP is a particularly desirable host lattice as it has optical properties that span the visible portion of the electromagnetic spectrum and is significantly less environmentally detrimental than the well-developed cadmium chalcogenide alternatives.[39] A primary route to synthesizing doped materials has been partial cation exchange with the host lattice to tune the composition and dopant concentration of the final nanocrystal product.[33] While an extensive cation exchange literature has been developed for metal chalcogenides, few examples exist for metal phosphides. While InP nanocrystals can be formed from either Cd_3P_2 or Cu_3P via elevated temperature exchange, neither of these processes are reversible.[40,41] Conversely, zinc selenide nanocrystals can undergo cation exchange to form ZnCdSe alloyed structures, with the zinc diffusing out and the cadmium diffusing in.[42] Exchange from InP to Cd_3P_2 has been observed when starting from magic-size clusters, but this is likely driven by the inherently strained nature of the InP cluster lattice.[43]

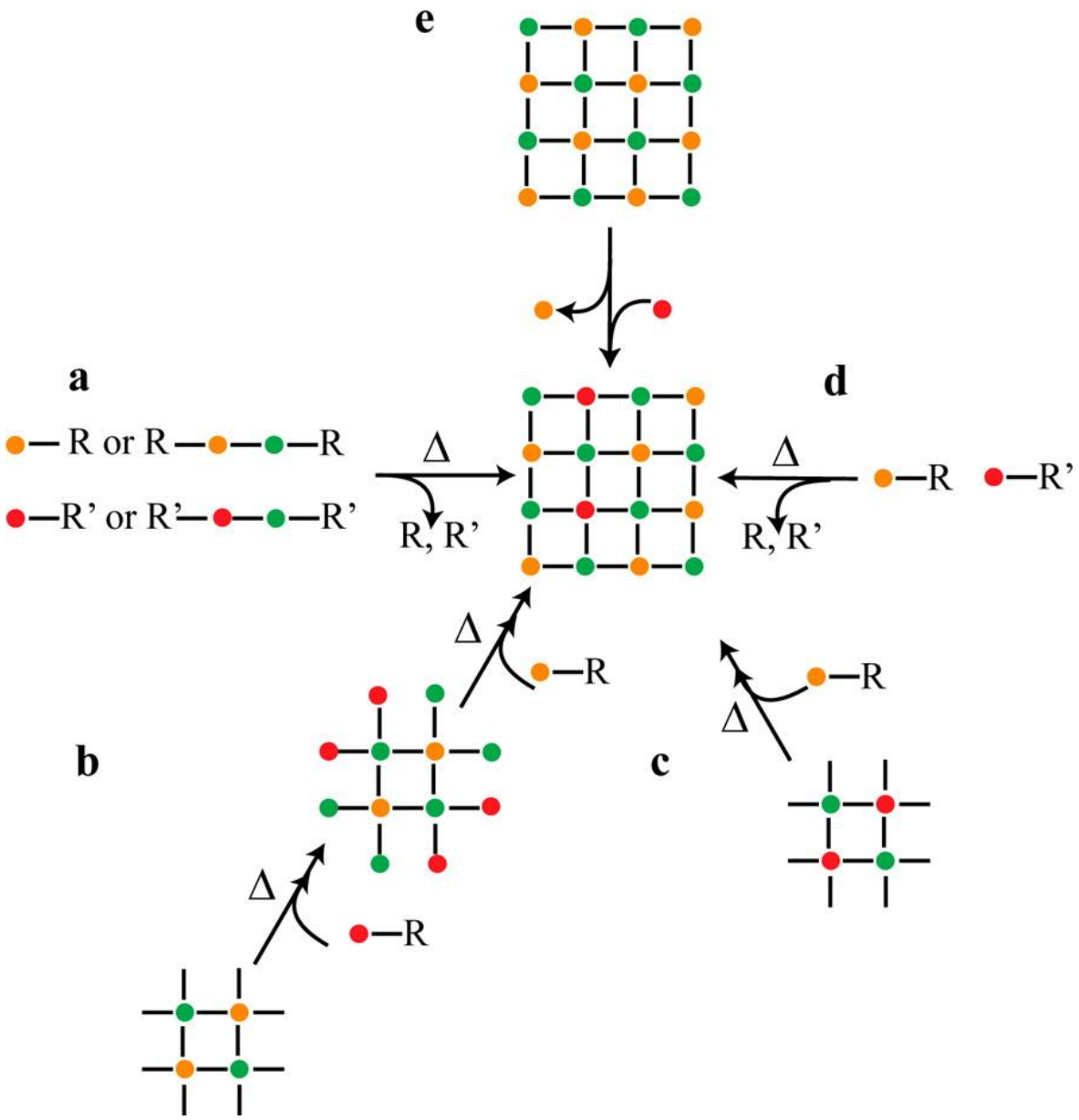

Figure 1.4. General schematics of synthetic approaches to nanocrystal doping with E representing ion exchange within the previously formed lattice. Reprinted with permission from Reference 33.[33]

While incorporating cations into an InP lattice is challenging at temperatures conducive to colloidal chemistry, it is by no means impossible. Multiple reports show diffusion of copper into traditionally synthesized InP nanocrystals at a range of sizes, followed by zinc chalcogenide shelling to generate NIR emitters with PLQYs of up to 40%.[38,44,45] Recent work synthesizing doped

nanoparticles using a copper cluster as a seed was successful, but the particles exhibit no photoluminescence.[46] Copper dopants are particularly interesting as the distinctive luminescence arises from the electron in the conduction band recombining with the hole that has been trapped at the copper.[34] This luminescent hole trap provides a spectroscopic handle for deconvolution of electron trapping processes from the mid-gap hole traps present in as-synthesized InP.[34] The nature of carrier trapping, a major source of decreased PLQY in InP, has received recent attention in the literature as synthetic procedures for producing otherwise high quality InP now exist, but the PLQYs of as-synthesized materials remain low.[47,48] A common way to increase the PLQY is to treat the surface with various methods hypothesized to remove some type of trap by an uncertain mechanism.[49] Materials shelled with thick gradient alloys of ZnSe/S have reached PLQY of over 95%, but much is still unknown about the fundamental methods of trap passivation.[50]

In this work, I focus on the use of tris-(diethylamino)phosphine as a versatile precursor for the synthesis of phase-pure and doped phosphide nanocrystals. Prior to my work, aminophosphines had only been studied as a route to size-tunable indium phosphide. However, there were hints in the literature that these precursors could be more broadly applied to the synthesis of other metal phosphides. In chapter 2, I will explore the synthesis of a range of metal phosphides with size or phase control, both semiconducting and metallic, from aminophosphines. This work showing the broad reactivity of aminophosphines, combined with hypotheses about the impact of differences in surface chemistry, led us to explore aminophosphine-derived InP as a platform for transition metal doping as detailed in chapter 3.

1.5 REFERENCES

(1) Talapin, D. V.; Lee, J.-S.; Kovalenko, M. V.; Shevchenko, E. V. Prospects of Colloidal Nanocrystals for Electronic and Optoelectronic Applications. *Chem. Rev.* **2010**, *110* (1), 389–458. https://doi.org/10.1021/cr900137k.
(2) Alivisatos, A. P. Semiconductor Clusters, Nanocrystals, and Quantum Dots. *Science* **1996**, *271*, 933.
(3) Xia, Y.; Yang, H.; Campbell, C. T. Nanoparticles for Catalysis. *Acc. Chem. Res.* **2013**, *46* (8), 1671–1672. https://doi.org/10.1021/ar400148q.
(4) Seh, Z. W.; Kibsgaard, J.; Dickens, C. F.; Chorkendorff, I.; Nørskov, J. K.; Jaramillo, T. F. Combining Theory and Experiment in Electrocatalysis: Insights into Materials Design. *Science* **2017**, *355* (6321), eaad4998. https://doi.org/10.1126/science.aad4998.
(5) Zherebetskyy, D.; Scheele, M.; Zhang, Y.; Bronstein, N.; Thompson, C.; Britt, D.; Salmeron, M.; Alivisatos, P.; Wang, L.-W. Hydroxylation of the Surface of PbS Nanocrystals Passivated with Oleic Acid. *Science* **2014**, *344* (6190), 1380. https://doi.org/10.1126/science.1252727.
(6) R. Heath, J. Covalency in Semiconductor Quantum Dots. *Chem. Soc. Rev.* **1998**, *27* (1), 65–71. https://doi.org/10.1039/A827065Z.
(7) Carenco, S.; Portehault, D.; Boissière, C.; Mézailles, N.; Sanchez, C. Nanoscaled Metal Borides and Phosphides: Recent Developments and Perspectives. *Chem. Rev.* **2013**, *113* (10), 7981–8065. https://doi.org/10.1021/cr400020d.
(8) Tamang, S.; Lincheneau, C.; Hermans, Y.; Jeong, S.; Reiss, P. Chemistry of InP Nanocrystal Syntheses. *Chem. Mater.* **2016**, *28* (8), 2491–2506. https://doi.org/10.1021/acs.chemmater.5b05044.
(9) Glassy, B. A.; Cossairt, B. M. II3V2 (II: Zn, Cd; V: P, As) Semiconductors: From Bulk Solids to Colloidal Nanocrystals. *Small* 1702038-n/a. https://doi.org/10.1002/smll.201702038.
(10) Callejas, J. F.; Read, C. G.; Roske, C. W.; Lewis, N. S.; Schaak, R. E. Synthesis, Characterization, and Properties of Metal Phosphide Catalysts for the Hydrogen-Evolution Reaction. *Chem. Mater.* **2016**, *28* (17), 6017–6044. https://doi.org/10.1021/acs.chemmater.6b02148.
(11) Shi, Y.; Zhang, B. Recent Advances in Transition Metal Phosphide Nanomaterials: Synthesis and Applications in Hydrogen Evolution Reaction. *Chem Soc Rev* **2016**, *45* (6), 1529–1541. https://doi.org/10.1039/C5CS00434A.
(12) Battaglia, D.; Peng, X. Formation of High Quality InP and InAs Nanocrystals in a Noncoordinating Solvent. *Nano Lett.* **2002**, *2* (9), 1027–1030. https://doi.org/10.1021/nl025687v.
(13) Gary, D. C.; Terban, M. W.; Billinge, S. J. L.; Cossairt, B. M. Two-Step Nucleation and Growth of InP Quantum Dots via Magic-Sized Cluster Intermediates. *Chem. Mater.* **2015**, *27* (4), 1432–1441. https://doi.org/10.1021/acs.chemmater.5b00286.
(14) Popczun, E. J.; Read, C. G.; Roske, C. W.; Lewis, N. S.; Schaak, R. E. Highly Active Electrocatalysis of the Hydrogen Evolution Reaction by Cobalt Phosphide Nanoparticles. *Angew. Chem.* **2014**, *126* (21), 5531–5534. https://doi.org/10.1002/ange.201402646.
(15) Muthuswamy, E.; Savithra, G. H. L.; Brock, S. L. Synthetic Levers Enabling Independent Control of Phase, Size, and Morphology in Nickel Phosphide Nanoparticles. *ACS Nano* **2011**, *5* (3), 2402–2411. https://doi.org/10.1021/nn1033357.

(16) Tessier, M. D.; Dupont, D.; De Nolf, K.; De Roo, J.; Hens, Z. Economic and Size-Tunable Synthesis of InP/ZnE (E = S, Se) Colloidal Quantum Dots. *Chem. Mater.* **2015**, *27* (13), 4893–4898. https://doi.org/10.1021/acs.chemmater.5b02138.
(17) Tessier, M. D.; De Nolf, K.; Dupont, D.; Sinnaeve, D.; De Roo, J.; Hens, Z. Aminophosphines: A Double Role in the Synthesis of Colloidal Indium Phosphide Quantum Dots. *J. Am. Chem. Soc.* **2016**, *138* (18), 5923–5929. https://doi.org/10.1021/jacs.6b01254.
(18) Buffard, A.; Dreyfuss, S.; Nadal, B.; Heuclin, H.; Xu, X.; Patriarche, G.; Mézailles, N.; Dubertret, B. Mechanistic Insight and Optimization of InP Nanocrystals Synthesized with Aminophosphines. *Chem. Mater.* **2016**, *28* (16), 5925–5934. https://doi.org/10.1021/acs.chemmater.6b02456.
(19) Song, W.-S.; Lee, H.-S.; Lee, J. C.; Jang, D. S.; Choi, Y.; Choi, M.; Yang, H. Amine-Derived Synthetic Approach to Color-Tunable InP/ZnS Quantum Dots with High Fluorescent Qualities. *J. Nanoparticle Res.* **2013**, *15* (6), 1750. https://doi.org/10.1007/s11051-013-1750-y.
(20) Srivastava, V.; Janke, E. M.; Diroll, B. T.; Schaller, R. D.; Talapin, D. V. Facile, Economic and Size-Tunable Synthesis of Metal Arsenide Nanocrystals. *Chem. Mater.* **2016**, *28* (18), 6797–6802. https://doi.org/10.1021/acs.chemmater.6b03501.
(21) Dupont, D.; Tessier, M. D.; Smet, P. F.; Hens, Z. Indium Phosphide-Based Quantum Dots with Shell-Enhanced Absorption for Luminescent Down-Conversion. *Adv. Mater.* **2017**, *29* (29), 1700686-n/a. https://doi.org/10.1002/adma.201700686.
(22) Laufersky, G.; Bradley, S.; Frécaut, E.; Lein, M.; Nann, T. Unraveling Aminophosphine Redox Mechanisms for Glovebox-Free InP Quantum Dot Syntheses. *Nanoscale* **2018**, *10* (18), 8752–8762. https://doi.org/10.1039/C8NR01286E.
(23) Smith, D. K.; Luther, J. M.; Semonin, O. E.; Nozik, A. J.; Beard, M. C. Tuning the Synthesis of Ternary Lead Chalcogenide Quantum Dots by Balancing Precursor Reactivity. *ACS Nano* **2011**, *5* (1), 183–190. https://doi.org/10.1021/nn102878u.
(24) Owen, J. S.; Chan, E. M.; Liu, H.; Alivisatos, A. P. Precursor Conversion Kinetics and the Nucleation of Cadmium Selenide Nanocrystals. *J. Am. Chem. Soc.* **2010**, *132* (51), 18206–18213. https://doi.org/10.1021/ja106777j.
(25) Hendricks, M. P.; Campos, M. P.; Cleveland, G. T.; Jen-La Plante, I.; Owen, J. S. A Tunable Library of Substituted Thiourea Precursors to Metal Sulfide Nanocrystals. *Science* **2015**, *348* (6240), 1226. https://doi.org/10.1126/science.aaa2951.
(26) Campos, M. P.; Hendricks, M. P.; Beecher, A. N.; Walravens, W.; Swain, R. A.; Cleveland, G. T.; Hens, Z.; Sfeir, M. Y.; Owen, J. S. A Library of Selenourea Precursors to PbSe Nanocrystals with Size Distributions near the Homogeneous Limit. *J. Am. Chem. Soc.* **2017**, *139* (6), 2296–2305. https://doi.org/10.1021/jacs.6b11021.
(27) Hamachi, L. S.; Yang, H.; Jen-La Plante, I.; Saenz, N.; Qian, K.; Campos, M. P.; Cleveland, G. T.; Rreza, I.; Oza, A.; Walravens, W.; et al. Precursor Reaction Kinetics Control Compositional Grading and Size of CdSe1−xSx Nanocrystal Heterostructures. *Chem Sci* **2019**, *10* (26), 6539–6552. https://doi.org/10.1039/C9SC00989B.
(28) Gary, D. C.; Glassy, B. A.; Cossairt, B. M. Investigation of Indium Phosphide Quantum Dot Nucleation and Growth Utilizing Triarylsilylphosphine Precursors. *Chem. Mater.* **2014**, *26* (4), 1734–1744. https://doi.org/10.1021/cm500102q.
(29) Xie, L.; Shen, Y.; Franke, D.; Sebastián, V.; Bawendi, M. G.; Jensen, K. F. Characterization of Indium Phosphide Quantum Dot Growth Intermediates Using MALDI-TOF Mass Spectrometry. *J. Am. Chem. Soc.* **2016**, *138* (41), 13469–13472. https://doi.org/10.1021/jacs.6b06468.

(30) Gary, D. C.; Flowers, S. E.; Kaminsky, W.; Petrone, A.; Li, X.; Cossairt, B. M. Single-Crystal and Electronic Structure of a 1.3 Nm Indium Phosphide Nanocluster. *J. Am. Chem. Soc.* **2016**, *138* (5), 1510–1513. https://doi.org/10.1021/jacs.5b13214.
(31) Erwin, S. C.; Zu, L.; Haftel, M. I.; Efros, A. L.; Kennedy, T. A.; Norris, D. J. Doping Semiconductor Nanocrystals. *Nature* **2005**, *436*, 91.
(32) Bhargava, R. N. Doped Nanocrystalline Materials—Physics and Applications. *J Lumin* **1996**, *70*, 85.
(33) Buonsanti, R.; Milliron, D. J. Chemistry of Doped Colloidal Nanocrystals. *Chem. Mater.* **2013**, *25* (8), 1305–1317. https://doi.org/10.1021/cm304104m.
(34) Knowles, K. E.; Hartstein, K. H.; Kilburn, T. B.; Marchioro, A.; Nelson, H. D.; Whitham, P. J.; Gamelin, D. R. Luminescent Colloidal Semiconductor Nanocrystals Containing Copper: Synthesis, Photophysics, and Applications. *Chem. Rev.* **2016**, *116* (18), 10820–10851. https://doi.org/10.1021/acs.chemrev.6b00048.
(35) Somaskandan, K.; Tsoi, G. M.; Wenger, L. E.; Brock, S. L. Isovalent Doping Strategy for Manganese Introduction into III-V Diluted Magnetic Semiconductor Nanoparticles: InP:Mn. *Chem. Mater.* **2005**, *17* (5), 1190–1198. https://doi.org/10.1021/cm048796e.
(36) Martin, W. E. Photoluminescence Determinations of Cd Diffusion in ZnSe. *J. Appl. Phys.* **1973**, *44* (12), 5639–5641. https://doi.org/10.1063/1.1662217.
(37) Wheeler, C. B.; Roedel, R. J.; Nelson, R. W.; Schauer, S. N.; Williams, P. Reproducible Leaky Tube Diffusion of Cd in InP at 500 °C. *J. Appl. Phys.* **1990**, *68* (3), 969–972. https://doi.org/10.1063/1.346662.
(38) Xie, R.; Peng, X. Synthesis of Cu-Doped InP Nanocrystals (d-Dots) with ZnSe Diffusion Barrier as Efficient and Color-Tunable NIR Emitters. *J. Am. Chem. Soc.* **2009**, *131* (30), 10645–10651. https://doi.org/10.1021/ja903558r.
(39) Tarantini, A.; Wegner, K. D.; Dussert, F.; Sarret, G.; Beal, D.; Mattera, L.; Lincheneau, C.; Proux, O.; Truffier-Boutry, D.; Moriscot, C.; et al. Physicochemical Alterations and Toxicity of InP Alloyed Quantum Dots Aged in Environmental Conditions: A Safer by Design Evaluation. *NanoImpact* **2019**, *14*, 100168. https://doi.org/10.1016/j.impact.2019.100168.
(40) Beberwyck, B. J.; Alivisatos, A. P. Ion Exchange Synthesis of III–V Nanocrystals. *J. Am. Chem. Soc.* **2012**, *134* (49), 19977–19980. https://doi.org/10.1021/ja309416c.
(41) De Trizio, L.; Gaspari, R.; Bertoni, G.; Kriegel, I.; Moretti, L.; Scotognella, F.; Maserati, L.; Zhang, Y.; Messina, G. C.; Prato, M.; et al. Cu3-XP Nanocrystals as a Material Platform for Near-Infrared Plasmonics and Cation Exchange Reactions. *Chem. Mater.* **2015**, *27* (3), 1120–1128. https://doi.org/10.1021/cm5044792.
(42) Groeneveld, E.; Witteman, L.; Lefferts, M.; Ke, X.; Bals, S.; Van Tendeloo, G.; de Mello Donega, C. Tailoring ZnSe–CdSe Colloidal Quantum Dots via Cation Exchange: From Core/Shell to Alloy Nanocrystals. *ACS Nano* **2013**, *7* (9), 7913–7930. https://doi.org/10.1021/nn402931y.
(43) Stein, J. L.; Steimle, M. I.; Terban, M. W.; Petrone, A.; Billinge, S. J. L.; Li, X.; Cossairt, B. M. Cation Exchange Induced Transformation of InP Magic-Sized Clusters. *Chem. Mater.* **2017**, *29* (18), 7984–7992. https://doi.org/10.1021/acs.chemmater.7b03075.
(44) Mei, S.; Wei, X.; Yang, D.; Su, D.; Yang, W.; Zhang, G.; Hu, Z.; Yang, B.; Dai, H.; Xie, F.; et al. Color-Tunable Optical Properties of Cadmium-Free Transition Metal Ions Doped InP/ZnS Quantum Dots. *J. Lumin.* **2019**, *212*, 264–270. https://doi.org/10.1016/j.jlumin.2019.04.040.

(45) Wei, X.; Mei, S.; Zhang, G.; Su, D.; Xie, F.; Zhang, W.; Guo, R. Enhanced Tunable Dual Emission of Cu:InP/ZnS Quantum Dots Enabled by Introducing Ag Ions. *Appl. Surf. Sci.* **2019**, *493*, 605–612. https://doi.org/10.1016/j.apsusc.2019.06.059.
(46) Hassan, A.; Zhang, X.; Liu, C.; Snee, P. T. Electronic Structure and Dynamics of Copper-Doped Indium Phosphide Nanocrystals Studied with Time-Resolved X-Ray Absorption and Large-Scale DFT Calculations. *J. Phys. Chem. C* **2018**, *122* (20), 11145–11151. https://doi.org/10.1021/acs.jpcc.8b02124.
(47) Hughes, K. E.; Stein, J. L.; Friedfeld, M. R.; Cossairt, B. M.; Gamelin, D. R. Effects of Surface Chemistry on the Photophysics of Colloidal InP Nanocrystals. *ACS Nano* **2019**. https://doi.org/10.1021/acsnano.9b07027.
(48) Janke, E. M.; Williams, N. E.; She, C.; Zherebetskyy, D.; Hudson, M. H.; Wang, L.; Gosztola, D. J.; Schaller, R. D.; Lee, B.; Sun, C.; et al. Origin of Broad Emission Spectra in InP Quantum Dots: Contributions from Structural and Electronic Disorder. *J. Am. Chem. Soc.* **2018**, *140* (46), 15791–15803. https://doi.org/10.1021/jacs.8b08753.
(49) Stein, J. L.; Mader, E. A.; Cossairt, B. M. Luminescent InP Quantum Dots with Tunable Emission by Post-Synthetic Modification with Lewis Acids. *J. Phys. Chem. Lett.* **2016**, *7* (7), 1315–1320. https://doi.org/10.1021/acs.jpclett.6b00177.
(50) Kim, Y.; Ham, S.; Jang, H.; Min, J. H.; Chung, H.; Lee, J.; Kim, D.; Jang, E. Bright and Uniform Green Light Emitting InP/ZnSe/ZnS Quantum Dots for Wide Color Gamut Displays. *ACS Appl. Nano Mater.* **2019**, *2* (3), 1496–1504. https://doi.org/10.1021/acsanm.8b02063.
.

Chapter 2. AMINOPHOSPHINES AS VERSATILE PRECURSORS FOR THE SYNTHESIS OF METAL PHOSPHIDE NANOCRYSTALS

2.1 NOTE REGARDING COLLABORATOR CONTRIBUTIONS

This work was performed in collaboration with Dr. Evan Jahrman, who at the time was a graduate student working under Professor Gerald Seidler in the Department of Physics at the University of Washington. All XANES measurements and fits to the XANES spectra were performed by Evan Jahrman. I am grateful to fellow members of Associate Professor Brandi Cossairt's lab David Ung, a graduate student who performed all the electrochemical measurements, and Nathan Lai, an exceptional undergraduate researcher who assisted in material synthesis and purification.

2.2 INTRODUCTION

Recently, interest in the synthesis of metal phosphide nanomaterials has increased due to their utility in light harvesting, energy conversion, and catalysis.[1–5] While colloidal syntheses for some phosphides have been well-established (i.e. – InP), a similar level of synthetic development has proven challenging for other phosphide materials.[1,6] Many of these syntheses have been constrained by the high reactivity of typical phosphorous precursors, like $P(SiMe_3)_3$ and PH_3.[7–12] The reaction kinetics for these reactive anion sources are often diffusion-controlled, forcing size

tuning to be accomplished via atom inefficient methods, such as halting the reaction before completion. The development of tunable precursor reactivity that allows for kinetic control of nanocrystal growth opens avenues for intelligent synthetic design.[13–18] One of these approaches recently developed for InP quantum dots (QDs) is based on $P(NR_2)_3$ (R = Me, Et) and InX_3 (X = Cl, Br, I), with the reactivity of the indium halide controlling QD nucleation.[15–19] This method is also advantageous in its implementation of less expensive and less hazardous aminophosphine precursors. However, this synthetic procedure has yet to be generalized to other phosphide materials.

In particular, the use of aminophosphine precursors appeared to be a promising option for the synthesis of both II-V semiconductors and transition metal phosphides. These materials are of significant interest due to the wide range of band gaps accessible via the II-V materials (Cd_3P_2: 0.55 eV, Zn_3P_2: 1.5 eV) and the high electrocatalytic activity of transition metal phosphides.[1,2] In this paper, we have broadened the scope of aminophosphine reactivity to include the synthesis of Cd_3P_2, Zn_3P_2, Co_2P, CoP, and Ni_2P. We show that highly crystalline Cd_3P_2 nanoparticles are accessible over a range of sizes via control of precursor reactivity, stoichiometry, and reaction temperature. In a similar vein, we demonstrate that in the case of cobalt phosphide, the phase of the material can be easily synthetically controlled.

2.3 Results and Discussion

Our typical aminophosphine-based synthesis is a modification of literature procedures,[15] with the MX_2 reagent dissolved in a long chain primary amine, degassed under vacuum at an elevated temperature to ensure the dryness of the highly hygroscopic metal halides, and then heated further (150 °C – 300 °C) under N_2 gas with the reaction temperature dictated by the relative

reactivity of the specific MX_2 reagent. Once the reaction temperature was reached, tris-diethylaminophosphine was rapidly injected and the nanocrystals formed over a time period ranging from 10 minutes to 4 hours (Figure 2.1).

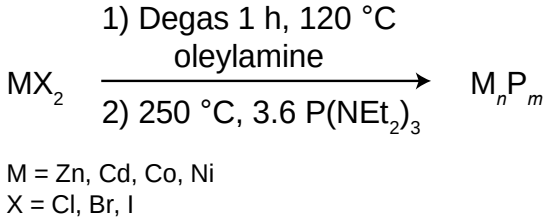

Figure 2.1. Standard reaction scheme for metal phosphide nanocrystal formation.

2.3.1 *Synthesis and Characterization of II-V materials*

Our initial experiments focused on the synthesis of Cd_3P_2, as prior literature reports led us to believe that cadmium halides would have affinity for aminophosphine precursors.[20] For example, the Hens group observed a red shift in the excitonic transition of indium phosphide upon Cd^{2+} addition prior to nucleation, which would be consistent with alloying or alteration of the indium phosphide nucleation kinetics.[21] Starting with a standard Cd:P ratio of 1:3.6 (the optimized conditions used for InP), we observe clear differences in the sizes of the nanocrystals formed at 250 °C from the various CdX_2 precursors as shown by statistical analysis of transmission electron microscopy (TEM) images (Figure 2.2, Figure 2.3).

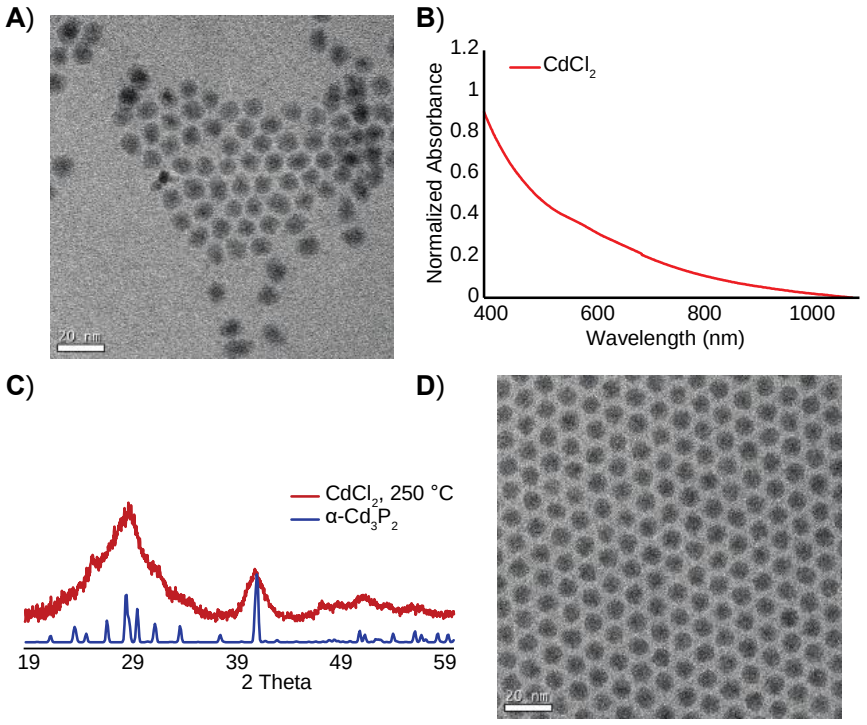

Figure 2.2. A) TEM image (6.8 ± 0.5 nm), (B) UV-Vis spectrum, and (C) XRD pattern of Cd_3P_2 nanocrystals prepared at 250 °C from $CdCl_2$ using a 1:3.6 ratio of Cd:P (Cd_3P_2 reference pattern PDF 01-070-3099 47-1443). D) TEM image of Cd_3P_2 prepared from $CdCl_2$ at 250 °C using a 1:1.3 ratio of Cd:P (7.5 ± 0.3 nm).

The particle sizes range from 6.8 ± 0.5 nm, 5.9 ± 0.7 nm, to 5.6 ± 0.5 nm from $CdCl_2$, $CdBr_2$, and CdI_2, respectively. The powder XRD patterns of all samples reflect the high degree of crystallinity in these samples (Figure 2.2C, Figure 2.3B), and show good agreement with the expected bulk pattern, with peak broadening due to the small crystalline domain size. Scherrer analysis indicates average crystalline domain sizes of 5.3 nm, 5.0 nm, or 4.0 nm for $CdCl_2$, $CdBr_2$, or CdI_2, respectively, consistent with the trend in average particle sizes extracted from TEM analysis. UV-Vis spectra of the final Cd_3P_2 nanocrystals show a steep rise in absorbance below 500 nm along with a structureless absorption tail at longer wavelengths. The absorbance onsets all

appear very similar, and distinct excitonic transitions are not observed despite the apparent crystallinity and monodispersity of the synthesized nanocrystals. This may be due to the presence of structural defects within the lattice that may result in indirect bandgap character in the as-synthesized material, as has been recently described for GaAs nanocrystals prepared under similar conditions.[22] This is the case even for materials synthesized under conditions optimized to result in very high monodispersity and crystallinity; for instance, conditions in which an effective excess of cadmium is used, Cd:P 1:1.3 at 250 °C, generate nanocrystals of 7.5 nm ± 0.3, as shown in Figure 2.2D. Due to the self-reducing nature of the aminophosphine precursor, four equivalents of $P(NEt_2)_3$ are necessary to produce one active phosphorous monomer. This results in an active Cd:P ratio of 1:0.33 in solution, leading to a metal rich environment in this optimized reaction.

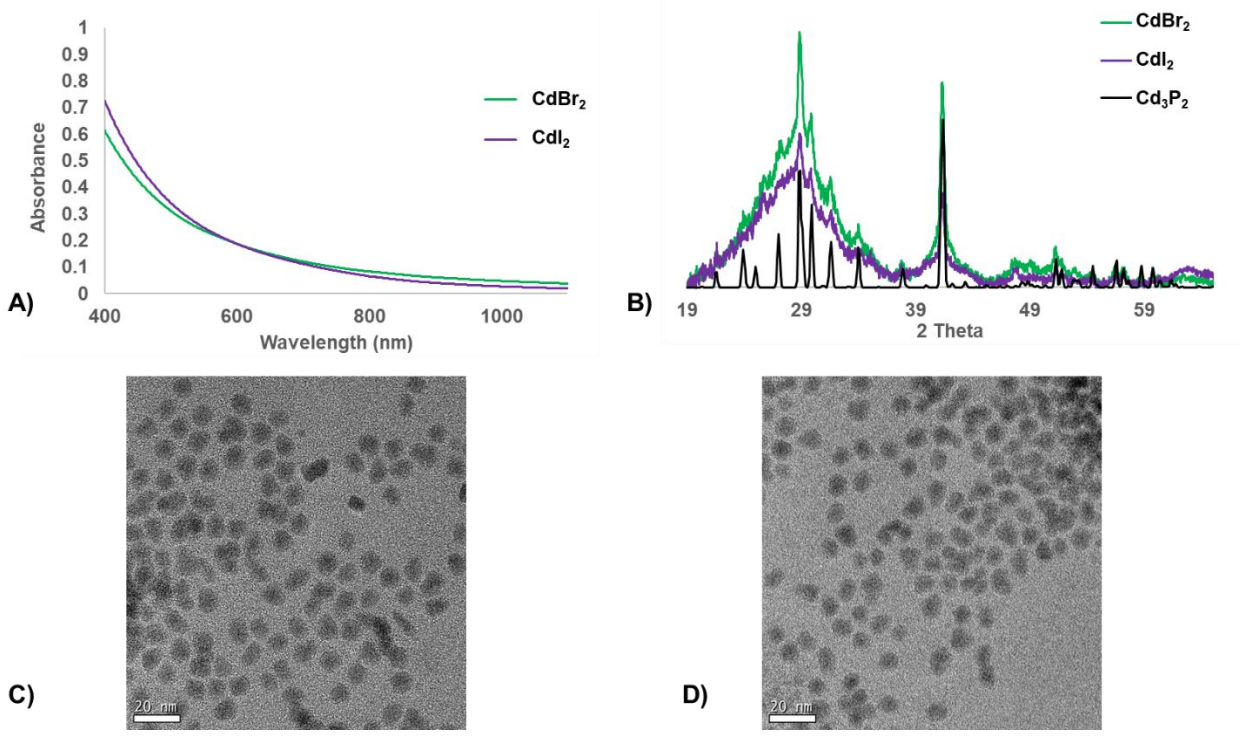

Figure 2.3. (A) UV-Vis final traces of materials synthesized from CdX_2 precursors. (B) XRD spectra of materials showing two populations of particles including one subset with a crystalline domain size >30 nm, consistent with mild heterogeneity observed in synthesis. TEM

images of (C) $CdBr_2$ (5.9 ± 0.7 nm) and (D) CdI_2 (5.6 ± 0.5) products showing the expected trend towards smaller nanocrystals as the halide becomes a better leaving group.

These data demonstrate the broader applicability of the size selective aminophosphine/metal halide precursor chemistry for the synthesis of metal phosphide nanocrystals. This reactivity does appear to be limited to softer metal ions with appreciable affinity for phosphorous based on Hard-Soft Acid-Base theory. A similar study performed with zinc halides shows that while Zn_3P_2 nanocrystals can be formed at 250 °C and higher, they do not exhibit the desired halide-controlled size tunability at any temperature (Figure 2.4). We hypothesize that this is due to the decreased relative reactivity of ZnX_2 sources with the aminophosphines and Zn-X bond cleavage no longer being involved in the rate-limiting step of the precursor conversion reaction mechanism.[16] It is worth noting that $ZnCl_2$ is typically included in the reaction mixture during the synthesis of InP QDs from aminophosphine precursors.[15–18] Extensive analysis suggests that under the conditions of the InP synthesis, namely 180 °C, significant quantities of zinc are not incorporated into the core of the InP QDs.[17] This is consistent with our observation that much higher temperatures are required to access Zn_3P_2 QDs using this chemistry.

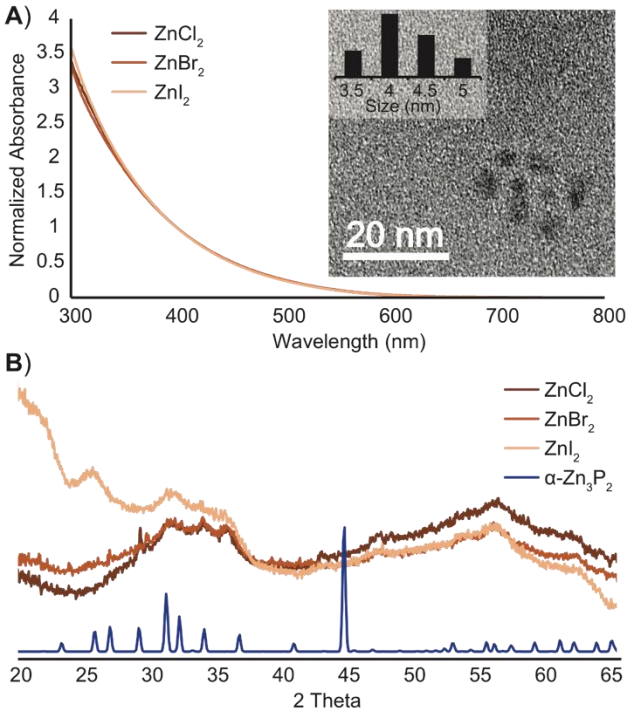

Figure 2.4. Synthesis of Zn_3P_2 from ZnX_2 (X = Cl, Br, I) and $P(NEt_2)_3$ at 250°C. (a) Representative UV-Vis absorbance spectra of the final products normalized at 400 nm. Inset: TEM of product from $ZnCl_2$ and $P(NEt_2)_3$. (b) Air-free powder X-ray diffraction data of the purified products with Zn_3P_2 reference pattern (PDF 01-071-6507).

Based on the above observations, we investigated the reaction progress between aminophosphine and MX_2 sources to test if the operative mechanism that has been characterized for InP is conserved in this system. A series of ^{31}P NMR experiments following the speciation of the aminophosphine precursor over the course of the reaction showed similarities across the group II metals tested, with transamination preceding aminophosphine tautomerization, and finally the release of phosphonium salts, consistent with what has been seen in the literature for InP (Figure 2.5).[16] This suggests that the basic mechanism of monomer formation is conserved in the case of MX_2, suggesting that the metal valence does not impact the operative chemistry.

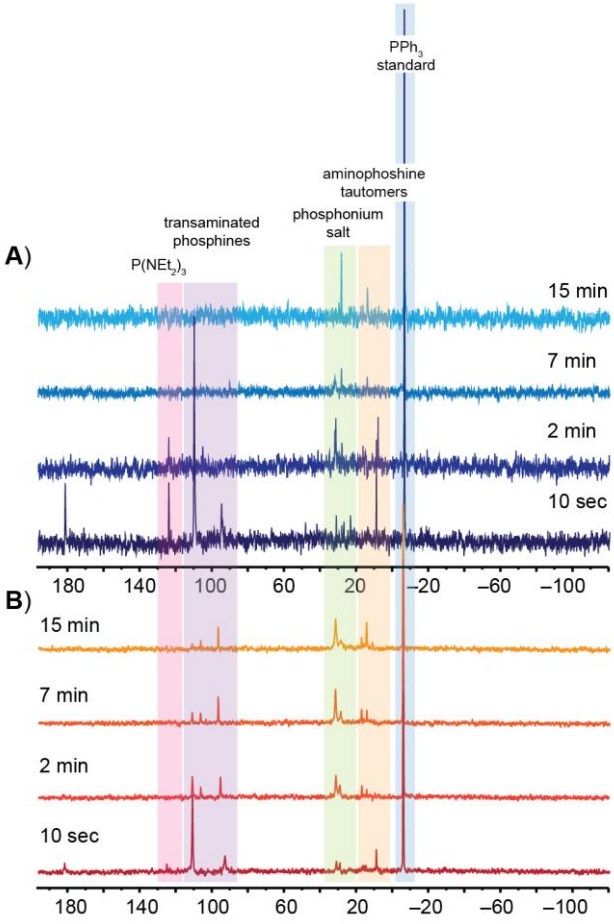

Figure 2.5. 202.4 MHz ^{31}P NMR of reaction aliquots in C_6D_6 with a triphenylphosphine internal standard: (A) Zn_3P_2 synthesis at 250°C. (B) Cd_3P_2 synthesis at 250°C.

2.3.2 *Synthesis and Characterization of Transition Metal Phosphides*

Given the success of the Cd_3P_2-based synthesis using aminophosphines and cadmium halides, we were interested to see if this synthesis could be translated to transition metal phosphides. The efficient synthesis of phase-pure nanoscale cobalt phosphide has historically been problematic, due to the high stability of both Co_2P and CoP and the substitution-inert nature of cobalt(III) precursors.[4,5,23–25] Traditional syntheses involve the formation of metallic ε-Co

nanoparticles followed by phosphorous intercalation via the Kirkendall effect to obtain the phosphide.[4,24] We hypothesized that the evident redox activity of the aminophosphine reaction would allow us to access the various cobalt oxidation states necessary to synthesize the phosphides directly without the intermediacy of a cobalt(0) phase.

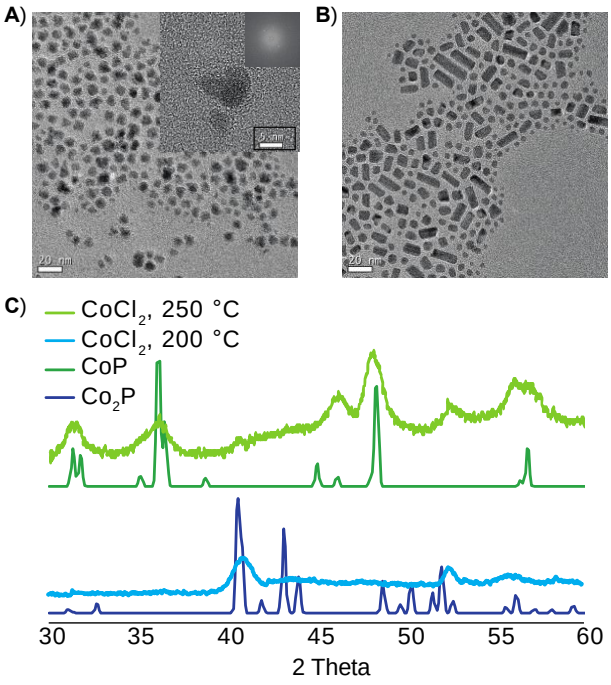

Figure 2.6. (A, B) TEM images (A: CoP 7.8 ± 0.7 nm; B: Co_2P of various morphologies with widths/diameters of 6.5 ± 0.6 nm) and (C) XRD pattern of CoP and Co_2P prepared at 250 °C and 200 °C, respectively. CoP (PDF 01-089-2598 29-497) and Co_2P (PDF 01-070-8358) reference patterns. The inset in figure (A) shows a zoomed in image of a single CoP nanocrystal with the corresponding FFT.

Following similar procedures as for the II-V materials, Figure 2.6A shows TEM images of the resulting nanoparticles formed from a reaction of $CoCl_2$ (1:3.6 Co:P) after 30 minutes at 250 °C. Based on the powder XRD pattern (Figure 2.6C) and lattice fringe analysis of the TEM images,

the nanocrystals are assigned as CoP. This observation was of particular interest because the conditions used here (30 min at 250 °C) are relatively mild for the synthesis of phase pure CoP when compared with material grown via the Kirkendall mechanism, which require 1 – 2.5 hrs at 320 – 350 °C.[4,24] Prior literature reports have shown that Co_2P often precedes the formation of CoP, and can be isolated at lower temperatures from those necessary to access CoP.[24] This holds true for the aminophosphine system. At 200 °C, Co_2P is exclusively formed under otherwise analogous reaction conditions (Figure 2.6 B, C).

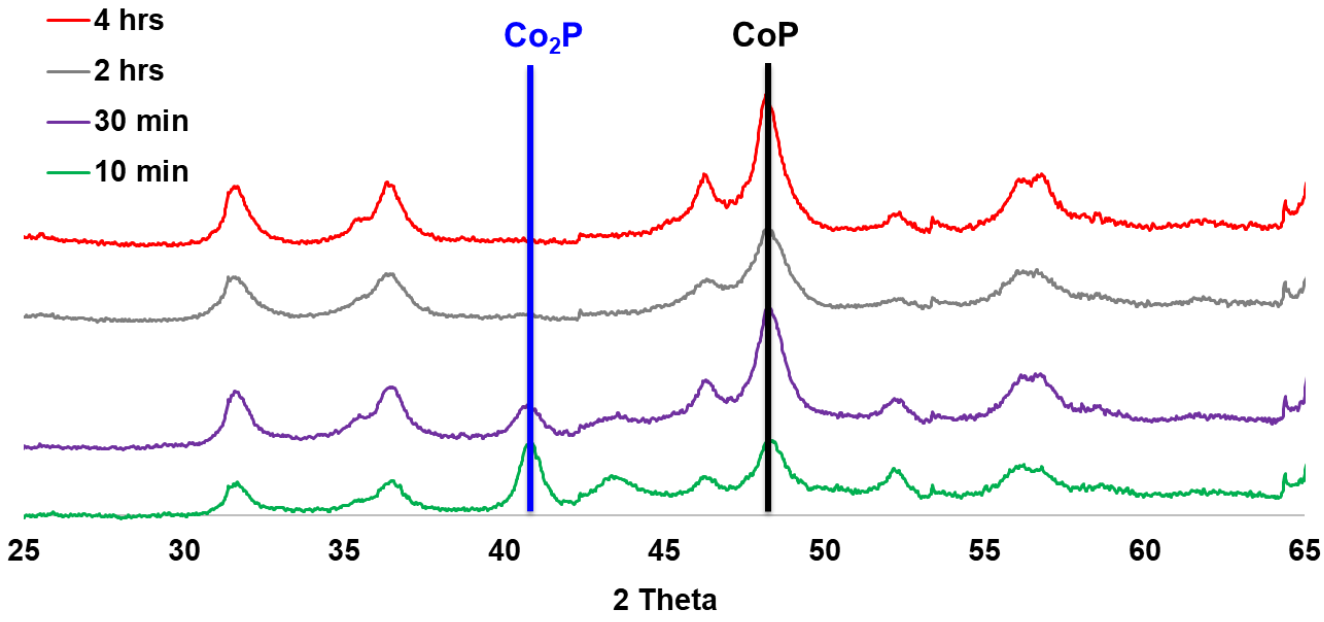

Figure 2.7. Synthesis of cobalt phosphides from CoI_2 at 250 °C. Powder X-ray diffraction data of products after different reaction times, showing the conversion from Co_2P to CoP with primary peaks of CoP (PDF 01-089-2598 29-497) and Co_2P (PDF 01-070-8358) from reference patterns. Reactions allowed to proceed for 30 minutes or less show a mixture of both phases. After two hours the material is now exclusively CoP.

Varying the halide precursor alters the phase purity of the nanocrystals formed at a given temperature, with the CoI_2 producing a mixture of Co_2P and CoP under analogous conditions to those used to access phase pure CoP from $CoCl_2$ (Figure 2.7). In addition, the Co_2P in the mixture can be converted to CoP through increased reaction times. At 10 and 30 minutes both phases are clearly visible, but by 2 hours the characteristic Co_2P peaks at 41 and 43.5 2θ disappear while the CoP pattern exhibits increased definition, indicative of increased CoP crystallinity and larger crystalline domain sizes. This provides insight into the chemistry of the Co(II) precursor, which is likely partially reduced to Co(I) during the initial phase of the reaction, generating Co_2P. From there we hypothesize that Co(III) is generated via disproportionation of Co(II) in the Co_2P product. This hypothesis is supported by information obtained by probing the cobalt K-edge via X-ray absorption near-edge structure (XANES). Figure 2.8 shows XANES data for Co_xP nanocrystals synthesized using our method compared to reference compounds. The near-edge regions of the XANES measurements show excellent agreement between the product of the present CoP synthesis procedure and a previously established methodology.[4] In addition, we observe clear spectral differences between the nominally CoP and Co_2P materials. A displacement of spectral features, including the first derivative's maxima, toward lower energies in Co_2P than for CoP is suggestive of a more reduced Co component in the product prepared at lower temperature.[26–29]

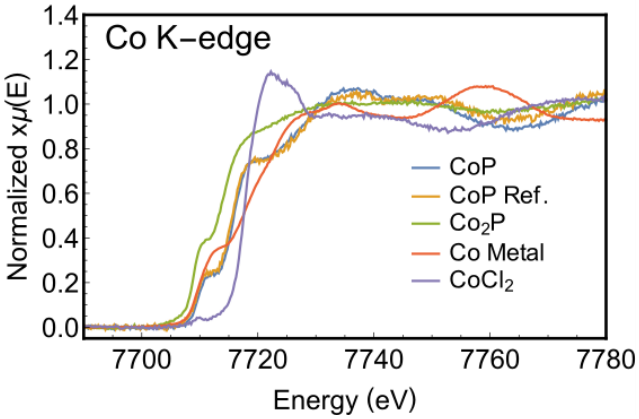

Figure 2.8. XANES spectra for the synthesized CoP and Co_2P, $CoCl_2$ and Co metal commercial standards, and CoP produced by an established literature procedure.[4] The CoP species exhibits several characteristic spectral features. Specifically, inflection points on the rising edge of the CoP spectra are observed at approximately 7709.75 eV and 7715.75 eV. These same features are considerably lower in energy at 7709.0 eV and 7714.0 eV in the nominal Co_2P phase. While an empirical standard was not readily available for comparison to Co_2P, the shift of the shoulders on the rising edge to lower energy generally indicates a more reduced cobalt oxidation state.[30]

One significant challenge with prior methods established to prepare transition metal phosphides has been obtaining larger quantities of phase pure material, particularly with respect to CoP.[31] As our synthesis proceeds rapidly at smaller scales, we decided to increase the scale four-fold with the aim of producing hundreds of milligrams of material. We found that when the scale was increased the reaction consistently yielded a mixture of CoP and Co_2P, despite extended reaction times and maintaining identical concentrations (Figure 2.9).

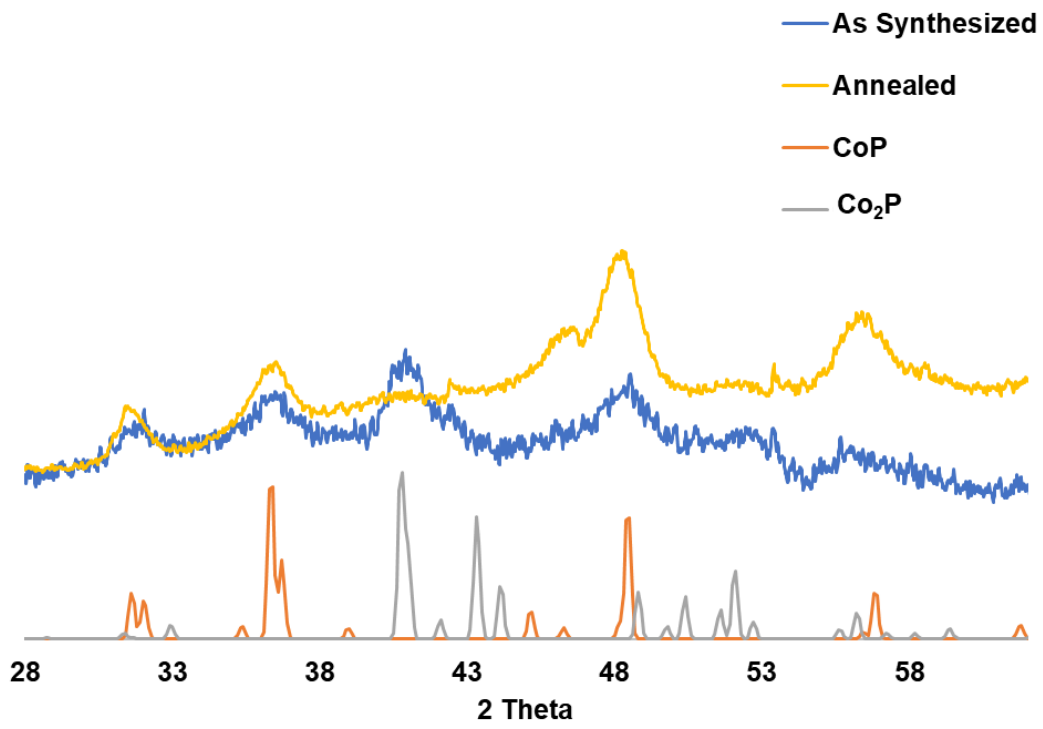

Figure 2.9. (A) P-XRD of scaled up reaction pre- and post-annealing for 7 hours with CoP (PDF 01-089-2598 29-497) and Co_2P (PDF 01-070-8358) reference patterns. The diffraction peaks in the annealed sample correspond exclusively to CoP, while a mixture of CoP and Co_2P is present in the as-synthesized sample.

We were able to synthesize 145 mg of CoP via a secondary annealing step. After purification, the original mixed phase nanocrystals were resuspended in oleylamine and heated to 250 °C. We found that 7 hours of reaction time was sufficient to convert the products completely to CoP via powder XRD analysis, however, the monodispersity does not suffer if the annealing continues overnight. While we cannot definitively state the mechanism that prevents conversion, we hypothesize that one of the byproducts of the reaction alters the chemical potential of the reaction solution and acts as an inhibitor to the formation of CoP.

Additional explorations of the synthesis of other transition metal phosphide nanocrystals are currently ongoing. Initial results regarding the synthesis of nickel phosphide are encouraging. Utilizing the standard conditions laid out above, Ni_2P can be easily prepared (Figure 2.10). At 250 °C we access phase-pure Ni_2P nanocrystals with an average diameter of 8.2 ± 1.6 nm as evidenced by XRD and TEM analysis.

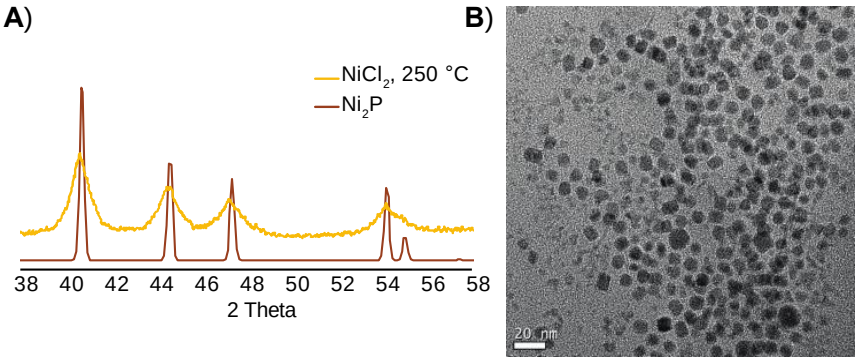

Figure 2.10. (A) P-XRD of reaction of $NiCl_2$ with $P(NEt_2)_3$ at 250 °C with Ni_2P reference pattern (PDF 01-074-1385). (B) TEM of product showing nanocrystals of 8.2 ± 1.6 nm.

2.3.3 *Reactivity for HER and Proton Transfer*

The CoP, Co_2P, and Ni_2P nanocrystals synthesized via the aminophosphine chemistry were examined as electrocatalysts for the hydrogen evolution reaction. Solutions of the nanoparticles were dropcast onto electrodes (carbon fiber or titanium) from toluene. In order to facilitate catalysis, the organic ligands were removed via two methods common in the literature; thermal annealing or chemical stripping.[4,32–37] Figure 2.11 shows the linear sweep voltammograms comparing the TMPs on thermally annealed carbon fiber electrodes. More traditional titanium electrodes were also studied, but film heterogeneity produced variable performance.

Table 2.1. Overpotentials for materials under reported conditions. The lowest overpotential is seen for Co_2P annealed on titanium, but the Meerwein's treatment produces competitive activities under significantly milder conditions.

Material	$\eta_{10mA/cm2}$ annealed on Ti	$\eta_{10mA/cm2}$ annealed on CF	$\eta_{10mA/cm2}$ Meerwein's treated on CF
CoP	676 mV	315 mV	314 mV
Co_2P	144 mV	147 mV	160 mV
Ni_2P	176 mV	169 mV	246 mV

While all materials are electrocatalytically active, a consistent trend in overpotentials at current densities of $10mA/cm^2$ emerges across all conditions (Table 2.1). The Co_2P is the most active material, followed by Ni_2P and CoP, with best observed overpotentials of 144 mV, 169 mV, and 314 mV, respectively. Similar results were obtained for the materials upon chemical stripping. Although CoP has been reported in the literature as the more active phase of cobalt phosphide, the consistency of our data suggests that Co_2P can have high activity when prepared via the aminophosphine method.[32,34]

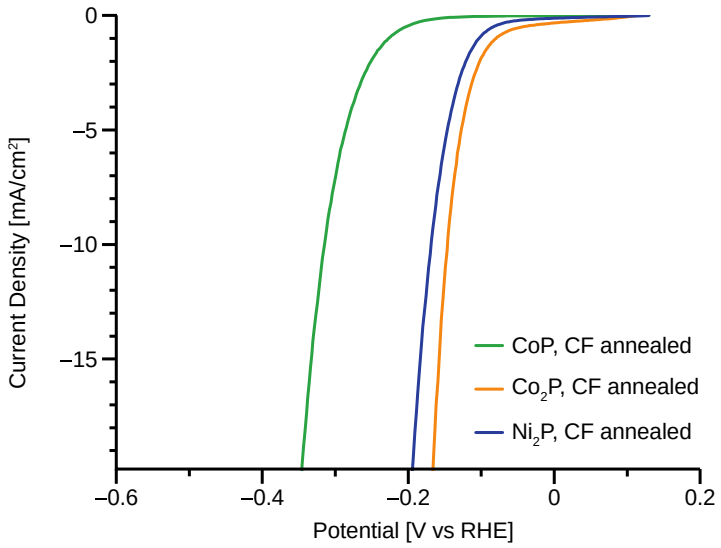

Figure 2.11. Linear sweep voltammograms at 5mV/s of the TMPs with I mg/cm^2 loadings annealed at 450 °C under a flow of 5%H_2/95% N_2 on carbon fiber electrodes in 0.5 M H_2SO_4 using a graphite counter electrode and a Ag/Ag_2SO_4 reference electrode. All materials demonstrate electrocatalytic activity, with Co_2P exhibiting the lowest overpotential.

Given the relative ease of the aminophosphine route towards synthesizing catalytically competent transition metal phosphides, the Mayer group at Yale University utilized these CoP nanocrystals to study the binding affinity of hydrogen on the material surface.[38] They found that the hydrogenated CoP could drive the conversion of phenylacetylene to styrene in THF. CoP was treated with H_2 gas at room temperature prior to mixing with phenylacetylene to "load" the CoP surface with H atoms and was then found to transfer 200 H atoms to the phenylacetylenes per nanoparticle. Although not studied on the nanocrystals, in the case of mesoscale CoP H_2 is not the only H atom transfer agent that can add to the CoP surface; a range of molecules can be used. Interestingly, by varying the strength of the donor-H bond different levels of H atom coverage were obtained. This indicates the presence of different binding sites with a range of activities.

2.4 CONCLUSIONS

In conclusion, we have demonstrated the utility of an aminophosphine precursor to synthesize non-InP metal phosphides. Size-tunable Cd_3P_2 was synthesized, and optimized conditions produced highly monodisperse nanocrystals. ^{31}P NMR studies showed that the hypothesized mechanism for monomer formation is consistent across cation oxidation states when redox inactive metal halides are used as precursors. Given the knowledge that this reactivity can be generalized across oxidation state, we then synthesized cobalt and nickel phosphide. By tuning the reaction conditions we were able to generate phase-pure Co_2P or CoP at mild temperatures compared to traditionally used syntheses. This approach shows promise for applications to additional TMPs, with encouraging results for Ni_2P. All TMPs synthesized via aminophosphines show electrocatalytic activity post ligand removal.

2.5 EXPERIMENTAL METHODS

All glassware was dried in a 160 °C oven overnight prior to use. All reactions were run under an inert atmosphere of nitrogen using a glovebox or standard Schlenk techniques. Zinc chloride (>98%), zinc bromide (98+%), zinc iodide (≥99.99% trace metal basis), cadmium chloride (anhydrous 99.0%), tris-diethylaminophosphine (97%), cobalt (II) chloride (≥98%), cobalt (II) bromide (99%), nickel (II) chloride (98%), H_2SO_4 (99.999%), and anhydrous methanol were purchased from Sigma-Aldrich Chemical Co., stored in a nitrogen glovebox, and used without further purification. Cadmium bromide (99%), cadmium iodide (99%), and cobalt iodide (min. 95%) were purchased from Strem Chemicals Inc., stored in a nitrogen glovebox, and used without further purification. All other solvents including oleylamine, pentane, toluene, and n-

methylformamide were purchased from Sigma Aldrich Chemical Co., dried over CaH_2, distilled, and stored over 4 Å sieves in a nitrogen glovebox. ^{31}P NMR spectra were collected on a 500 MHz Bruker Avance spectrometer. UV-vis spectra were collected on a Cary 5000 spectrophotometer from Agilent. TEM images were collected on a FEI Tecnai G2 F20 microscope using an ultrathin carbon film on holey carbon purchased from Ted Pella Inc. P-XRD diffractograms were collected on either a Bruker D8 Discover or Bruker Microfocus instrument. Solutions used for electrochemical measurement were prepared in 18 MΩ H_2O.

2.5.1 *Synthentic methods and basic sample preparation*

Standard metal phosphide reaction procedure

0.45 mmol of a metal(II) halide and 5 mL of dried and distilled oleylamine were added to a 25 mL 3-neck flask. The solution was then placed under vacuum at 120 °C and degassed for 1 hour. The vessel was then placed under an inert atmosphere and heated to temperature, ranging from 150 - 300 °C as described in the main text. Once the reaction temperature was reached, 0.45 mL of tris-diethylaminophosphine (1.6 mmol) was rapidly injected. The reaction began rapidly after injection and was allowed to proceed until the absorbance spectrum remained constant for a set amount of time (in the case of the cobalt phosphides). The flask was then cooled down to room temperature before being moved into a nitrogen glovebox for purification. The nanocrystals were precipitated with anhydrous methanol or isopropanol, centrifuged at 7830 rpm, and suspended in toluene. This procedure was repeated 5 times before any additional sample analysis was performed.

Standard cobalt phosphide scaled up reaction procedure

1.8 mmol of $CoCl_2$ and 20.0 mL of purified oleylamine were added to a 100 mL 3 neck flask. The solution was then placed under vacuum at 120 °C and degassed for 1 hour. The vessel was then placed under an inert atmosphere and heated to 250 °C. The reaction was allowed to proceed for a minimum of three hours before being halted and the nanocrystals were purified via the standard procedure outlined above. Once purified, the black solid was suspended in toluene, dried under vacuum, then resuspended in 15 mL of oleylamine. The solution was heated to 250 °C for a minimum of seven hours before being cooled and purified once again

Sample preparation for characterization

For PXRD samples, insoluble powders were placed onto a piece of double-sided tape on a silicon ⟨100⟩ single crystal wafer. Solvent was removed from colloidal samples until dryness was achieved and then the paste was spread on a silicon ⟨100⟩ single crystal wafer. For air-free spectra, the sample was sealed in a square with tape and covered with Kapton film. For TEM, samples were suspended in toluene or n-methylformamide with insoluble samples sonicated at room temperature for 15 minutes. The solutions were then drop cast onto a TEM grid and placed under vacuum overnight prior to imaging to ensure full solvent evaporation.

.

2.5.2 *X-ray absorption measurements*

Co K-edge X-ray absorption near edge structure (XANES) measurements were performed at the University of Washington with a laboratory-based instrument. The basic monochromator design is described in detail elsewhere, however, the present implementation benefits from three primary advantages.[39] The traditional 2-axis tilt is replaced in favor of the azimuthal orientation

method of Mortensen *et al.*, the position of the source and spherically bent crystal analyzer (SBCA) are maintained by passive mechanical coupling, and the source and detector translation stages are rotated symmetrically about the SBCA's direction of travel.[40] Furthermore, this study employed an X-ray tube source (Varex VF80 Pd anode) operated at 35 kV and 2.856 mA, i.e. 100 W total tube power, a Ge (444) spherically bent crystal analyzer (XRS Tech) to monochromatize the beam, and a silicon drift detector (Amptek SDD-X123).

XANES measurements were performed in transmission mode. Each XANES scan proceeded in 1 eV steps from at least 7655 eV to 7680 eV, 0.25 eV steps from 7680 to 7780, and 0.05 $Å^{-1}$ k steps until 9 $Å^{-1}$ beyond the edge. Analysis was performed using the software package Athena, in which spectra were background corrected and normalized after regressing a linear post-edge for the phosphides and a quadratic post-edge for the cobalt chloride and metal.[41,42] Empirical standards included anhydrous, 99.7 % metals basis cobalt chloride (Thermo Fischer Scientific) and a 4 μm thick foil of Co metal (EXAFS Materials). Prior to measurement, powder samples were diluted in a boron nitride binder, pressed into a pellet, and sealed in a polyimide pouch.

.

2.5.3 *Electrochemical characterization*

Electrochemical measurements were conducted in a custom four-neck cell fitted with a graphite rod counter electrode separated in a fritted compartment, a Ag/Ag_2SO_4 reference electrode separated by a Vycor frit, and a working electrode (carbon fiber or titanium). The carbon fiber working electrodes were fabricated from carbon fiber paper (Fuel Cell Store, Spectracarb 2050A 0850). For non-annealed experiments, the carbon fiber paper was cut into 1 cm x 3 cm rectangles and a copper wire was attached with a conductive silver epoxy to the electrode material. After

curing, the copper wire and silver epoxy were covered with gel epoxy to create a 1 cm x 1 cm working area on the electrode. The backside of the 1 cm x 1 cm working area of the electrode was not covered due to the porosity of the material and epoxy being able to leak onto both sides. Titanium working electrodes were fabricated in a similar fashion, using Ti foil (99.7%, Aldrich). However, the entire backsides of the titanium electrodes were covered with the gel epoxy. The TMP samples were then suspended in toluene and dropcasted in 10-20 µL aliquots onto the working electrodes for electrochemical measurements.

For the annealing experiments, the working electrodes were cut from carbon fiber or titanium, and the samples were drop-casted at low volumes on a 1 cm x 1 cm working area. The electrodes were brought into a MTI OTF-1200X tube furnace. The tube was evacuated and then refilled with 5% H_2/95% N_2 (Industrial Grade, Praxair) and the electrodes were annealed at 450 ºC for 30 min using the temperature ramp shown in figure S9. The tube furnace was allowed to cool down overnight in either vacuum or 5% H_2/95% N_2 and then cycled into a glovebox to be stored under inert atmosphere in order to keep the materials' exposure to air as minimal as possible. The electrodes were then brought out and silver epoxy was applied under an Ar atmosphere in an Ar bucket and cured at 50 ºC for one hour under a vacuum in a VWR Symphony vacuum oven. A 1 cm x 1 cm working area was masked out using gel epoxy and the gel epoxy cured for one hour in an Ar atmosphere before being transferred into Ar-flushed gas-tight headspace vials with magnetic caps with septa. These gas-tight vials with electrodes were brought into a Bel-Art Techni-Dome glove chamber for electrochemical measurements. For the chemical stripping experiments carbon fiber electrodes were prepared as above. The electrodes were then dipped in a solution of 0.1 M Meerwein's reagent (triethyloxonium tetrafluoroborate) in acetonitrile for 1-2 minutes and rinsed with acetonitrile in an Ar atmosphere.

2.6 REFERENCES

(1) Glassy, B. A.; Cossairt, B. M. II3V2 (II: Zn, Cd; V: P, As) Semiconductors: From Bulk Solids to Colloidal Nanocrystals. *Small* 1702038-n/a. https://doi.org/10.1002/smll.201702038.
(2) Shi, Y.; Zhang, B. Recent Advances in Transition Metal Phosphide Nanomaterials: Synthesis and Applications in Hydrogen Evolution Reaction. *Chem Soc Rev* **2016**, *45* (6), 1529–1541. https://doi.org/10.1039/C5CS00434A.
(3) Carenco, S.; Portehault, D.; Boissière, C.; Mézailles, N.; Sanchez, C. Nanoscaled Metal Borides and Phosphides: Recent Developments and Perspectives. *Chem. Rev.* **2013**, *113* (10), 7981–8065. https://doi.org/10.1021/cr400020d.
(4) Popczun, E. J.; Read, C. G.; Roske, C. W.; Lewis, N. S.; Schaak, R. E. Highly Active Electrocatalysis of the Hydrogen Evolution Reaction by Cobalt Phosphide Nanoparticles. *Angew. Chem.* **2014**, *126* (21), 5531–5534. https://doi.org/10.1002/ange.201402646.
(5) Huang, Z.; Chen, Z.; Chen, Z.; Lv, C.; Humphrey, M. G.; Zhang, C. Cobalt Phosphide Nanorods as an Efficient Electrocatalyst for the Hydrogen Evolution Reaction. *Nano Energy* **2014**, *9* (Supplement C), 373–382. https://doi.org/10.1016/j.nanoen.2014.08.013.
(6) Gary, D. C.; Terban, M. W.; Billinge, S. J. L.; Cossairt, B. M. Two-Step Nucleation and Growth of InP Quantum Dots via Magic-Sized Cluster Intermediates. *Chem. Mater.* **2015**, *27* (4), 1432–1441. https://doi.org/10.1021/acs.chemmater.5b00286.
(7) Miao, S.; Hickey, S. G.; Rellinghaus, B.; Waurisch, C.; Eychmüller, A. Synthesis and Characterization of Cadmium Phosphide Quantum Dots Emitting in the Visible Red to Near-Infrared. *J. Am. Chem. Soc.* **2010**, *132* (16), 5613–5615. https://doi.org/10.1021/ja9105732.
(8) Glassy, B. A.; Cossairt, B. M. Ternary Synthesis of Colloidal Zn3P2 Quantum Dots. *Chem. Commun.* **2015**, *51* (25), 5283–5286. https://doi.org/10.1039/C4CC08068H.
(9) Glassy, B. A.; Cossairt, B. M. Resolving the Chemistry of Zn3P2 Nanocrystal Growth. *Chem. Mater.* **2016**, *28* (17), 6374–6380. https://doi.org/10.1021/acs.chemmater.6b02782.
(10) Wang, R.; Ratcliffe, C. I.; Wu, X.; Voznyy, O.; Tao, Y.; Yu, K. Magic-Sized Cd3P2 II−V Nanoparticles Exhibiting Bandgap Photoemission. *J. Phys. Chem. C* **2009**, *113* (42), 17979–17982. https://doi.org/10.1021/jp907642b.
(11) Ojo, W.-S.; Xu, S.; Delpech, F.; Nayral, C.; Chaudret, B. Room-Temperature Synthesis of Air-Stable and Size-Tunable Luminescent ZnS-Coated Cd3P2 Nanocrystals with High Quantum Yields. *Angew. Chem. Int. Ed.* **2012**, *51* (3), 738–741. https://doi.org/10.1002/anie.201104864.
(12) Xie, R.; Zhang, J.; Zhao, F.; Yang, W.; Peng, X. Synthesis of Monodisperse, Highly Emissive, and Size-Tunable Cd3P2 Nanocrystals. *Chem. Mater.* **2010**, *22* (13), 3820–3822. https://doi.org/10.1021/cm1008653.
(13) Hendricks, M. P.; Campos, M. P.; Cleveland, G. T.; Jen-La Plante, I.; Owen, J. S. A Tunable Library of Substituted Thiourea Precursors to Metal Sulfide Nanocrystals. *Science* **2015**, *348* (6240), 1226. https://doi.org/10.1126/science.aaa2951.
(14) Campos, M. P.; Hendricks, M. P.; Beecher, A. N.; Walravens, W.; Swain, R. A.; Cleveland, G. T.; Hens, Z.; Sfeir, M. Y.; Owen, J. S. A Library of Selenourea Precursors to PbSe Nanocrystals with Size Distributions near the Homogeneous Limit. *J. Am. Chem. Soc.* **2017**, *139* (6), 2296–2305. https://doi.org/10.1021/jacs.6b11021.
(15) Tessier, M. D.; Dupont, D.; De Nolf, K.; De Roo, J.; Hens, Z. Economic and Size-Tunable Synthesis of InP/ZnE (E = S, Se) Colloidal Quantum Dots. *Chem. Mater.* **2015**, *27* (13), 4893–4898. https://doi.org/10.1021/acs.chemmater.5b02138.

(16) Tessier, M. D.; De Nolf, K.; Dupont, D.; Sinnaeve, D.; De Roo, J.; Hens, Z. Aminophosphines: A Double Role in the Synthesis of Colloidal Indium Phosphide Quantum Dots. *J. Am. Chem. Soc.* **2016**, *138* (18), 5923–5929. https://doi.org/10.1021/jacs.6b01254.
(17) Buffard, A.; Dreyfuss, S.; Nadal, B.; Heuclin, H.; Xu, X.; Patriarche, G.; Mézailles, N.; Dubertret, B. Mechanistic Insight and Optimization of InP Nanocrystals Synthesized with Aminophosphines. *Chem. Mater.* **2016**, *28* (16), 5925–5934. https://doi.org/10.1021/acs.chemmater.6b02456.
(18) Song, W.-S.; Lee, H.-S.; Lee, J. C.; Jang, D. S.; Choi, Y.; Choi, M.; Yang, H. Amine-Derived Synthetic Approach to Color-Tunable InP/ZnS Quantum Dots with High Fluorescent Qualities. *J. Nanoparticle Res.* **2013**, *15* (6), 1750. https://doi.org/10.1007/s11051-013-1750-y.
(19) Kim, K.; Yoo, D.; Choi, H.; Tamang, S.; Ko, J.-H.; Kim, S.; Kim, Y.-H.; Jeong, S. Halide–Amine Co-Passivated Indium Phosphide Colloidal Quantum Dots in Tetrahedral Shape. *Angew. Chem. Int. Ed.* **2016**, *55* (11), 3714–3718. https://doi.org/10.1002/anie.201600289.
(20) Srivastava, V.; Janke, E. M.; Diroll, B. T.; Schaller, R. D.; Talapin, D. V. Facile, Economic and Size-Tunable Synthesis of Metal Arsenide Nanocrystals. *Chem. Mater.* **2016**, *28* (18), 6797–6802. https://doi.org/10.1021/acs.chemmater.6b03501.
(21) Dupont, D.; Tessier, M. D.; Smet, P. F.; Hens, Z. Indium Phosphide-Based Quantum Dots with Shell-Enhanced Absorption for Luminescent Down-Conversion. *Adv. Mater.* **2017**, *29* (29), 1700686-n/a. https://doi.org/10.1002/adma.201700686.
(22) Srivastava, V.; Liu, W.; Janke, E. M.; Kamysbayev, V.; Filatov, A. S.; Sun, C.-J.; Lee, B.; Rajh, T.; Schaller, R. D.; Talapin, D. V. Understanding and Curing Structural Defects in Colloidal GaAs Nanocrystals. *Nano Lett.* **2017**, *17* (3), 2094–2101. https://doi.org/10.1021/acs.nanolett.7b00481.
(23) Maneeprakorn, W.; Malik, M. A.; O'Brien, P. The Preparation of Cobalt Phosphide and Cobalt Chalcogenide (CoX, X = S, Se) Nanoparticles from Single Source Precursors. *J Mater Chem* **2010**, *20* (12), 2329–2335. https://doi.org/10.1039/B922804G.
(24) Ha, D.-H.; Moreau, L. M.; Bealing, C. R.; Zhang, H.; Hennig, R. G.; Robinson, R. D. The Structural Evolution and Diffusion during the Chemical Transformation from Cobalt to Cobalt Phosphide Nanoparticles. *J Mater Chem* **2011**, *21* (31), 11498–11510. https://doi.org/10.1039/C1JM10337G.
(25) Zhang, H.; Ha, D.-H.; Hovden, R.; Kourkoutis, L. F.; Robinson, R. D. Controlled Synthesis of Uniform Cobalt Phosphide Hyperbranched Nanocrystals Using Tri-n-Octylphosphine Oxide as a Phosphorus Source. *Nano Lett.* **2011**, *11* (1), 188–197. https://doi.org/10.1021/nl103400a.
(26) Gaur, A.; Shrivastava, B. A Comparative Study of the Methods of Speciation Using X-Ray Absorption Fine Structure. *Acta Phys. Pol. A* **2012**, *121* (3), 647–652.
(27) Henderson, G. S.; de Groot, F. M. F.; Moulton, B. J. A. X-Ray Absorption Near-Edge Structure (XANES) Spectroscopy. *Rev. Mineral. Geochem.* **2014**, *78* (1), 75–138. https://doi.org/10.2138/rmg.2014.78.3.
(28) Ressler, T.; Wienold, J.; Jentoft, R. E.; Neisius, T. Bulk Structural Investigation of the Reduction of MoO3 with Propene and the Oxidation of MoO2 with Oxygen. *J. Catal.* **2002**, *210* (1), 67–83. https://doi.org/10.1006/jcat.2002.3659.
(29) Shulman, G. R.; Yafet, Y.; Eisenberger, P.; Blumberg, W. E. Observations and Interpretation of X-Ray Absorption Edges in Iron Compounds and Proteins. *Proc. Natl. Acad. Sci.* **1976**, *73* (5), 1384. https://doi.org/10.1073/pnas.73.5.1384.

(30) Bunker, G. *Introduction to XAFS: A Practical Guide to X-Ray Absorption Fine Structure Spectroscopy*; Cambridge University Press: Cambridge, 2010. https://doi.org/10.1017/CBO9780511809194.
(31) Tian, L.; Yan, X.; Chen, X.; Liu, L.; Chen, X. One-Pot, Large-Scale, Simple Synthesis of CoxP Nanocatalysts for Electrochemical Hydrogen Evolution. *J Mater Chem A* **2016**, *4* (33), 13011–13016. https://doi.org/10.1039/C6TA05503F.
(32) Callejas, J. F.; Read, C. G.; Roske, C. W.; Lewis, N. S.; Schaak, R. E. Synthesis, Characterization, and Properties of Metal Phosphide Catalysts for the Hydrogen-Evolution Reaction. *Chem. Mater.* **2016**, *28* (17), 6017–6044. https://doi.org/10.1021/acs.chemmater.6b02148.
(33) Popczun, E. J.; Roske, C. W.; Read, C. G.; Crompton, J. C.; McEnaney, J. M.; Callejas, J. F.; Lewis, N. S.; Schaak, R. E. Highly Branched Cobalt Phosphide Nanostructures for Hydrogen-Evolution Electrocatalysis. *J. Mater. Chem. A* **2015**, *3* (10), 5420–5425. https://doi.org/10.1039/C4TA06642A.
(34) Callejas, J. F.; Read, C. G.; Popczun, E. J.; McEnaney, J. M.; Schaak, R. E. Nanostructured Co2P Electrocatalyst for the Hydrogen Evolution Reaction and Direct Comparison with Morphologically Equivalent CoP. *Chem. Mater.* **2015**, *27* (10), 3769–3774. https://doi.org/10.1021/acs.chemmater.5b01284.
(35) Rosen Evelyn L.; Buonsanti Raffaella; Llordes Anna; Sawvel April M.; Milliron Delia J.; Helms Brett A. Exceptionally Mild Reactive Stripping of Native Ligands from Nanocrystal Surfaces by Using Meerwein's Salt. *Angew. Chem. Int. Ed.* **2011**, *51* (3), 684–689. https://doi.org/10.1002/anie.201105996.
(36) Henckel, D. A.; Lenz, O.; Cossairt, B. M. Effect of Ligand Coverage on Hydrogen Evolution Catalyzed by Colloidal WSe2. *ACS Catal.* **2017**, *7* (4), 2815–2820. https://doi.org/10.1021/acscatal.7b00074.
(37) Henckel, D. A.; Lenz, O. M.; Krishnan, K. M.; Cossairt, B. M. Improved HER Catalysis through Facile, Aqueous Electrochemical Activation of Nanoscale WSe2. *Nano Lett.* **2018**, *18* (4), 2329–2335. https://doi.org/10.1021/acs.nanolett.7b05213.
(38) Delley, M. F.; Wu, Z.; Mundy, M. E.; Ung, D.; Cossairt, B. M.; Wang, H.; Mayer, J. M. Hydrogen on Cobalt Phosphide. *J. Am. Chem. Soc.* **2019**, *141* (38), 15390–15402. https://doi.org/10.1021/jacs.9b07986.
(39) Seidler, G. T.; Mortensen, D. R.; Remesnik, A. J.; Pacold, J. I.; Ball, N. A.; Barry, N.; Styczinski, M.; Hoidn, O. R. A Laboratory-Based Hard x-Ray Monochromator for High-Resolution x-Ray Emission Spectroscopy and x-Ray Absorption near Edge Structure Measurements. *Rev. Sci. Instrum.* **2014**, *85* (11), 113906. https://doi.org/10.1063/1.4901599.
(40) Mortensen, D. R.; Seidler, G. T. Robust Optic Alignment in a Tilt-Free Implementation of the Rowland Circle Spectrometer. *J. Electron Spectrosc. Relat. Phenom.* **2017**, *215*, 8–15. https://doi.org/10.1016/j.elspec.2016.11.006.
(41) Ravel, B.; Newville, M. It ATHENA, It ARTEMIS, It HEPHAESTUS: Data Analysis for X-Ray Absorption Spectroscopy Using It IFEFFIT. *J. Synchrotron Radiat.* **2005**, *12* (4), 537–541. https://doi.org/10.1107/S0909049505012719.
(42) Ravel, B.; Newville, M. ATHENA and ARTEMIS: Interactive Graphical Data Analysis Using IFEFFIT. *Phys. Scr.* **2005**, *2005* (T115), 1007.

Chapter 3. SYNTHESIS AND SPECTROSCOPY OF EMISSIVE, SURFACE-MODIFIED, COPPER-DOPED INDIUM PHOSPHIDE NANOCRYSTALS

3.1 NOTE REGARDING COLLABORATOR CONTRIBUTIONS

This work was performed in collaboration with Forrest Eagle, who performed the transient optical spectroscopies. I am grateful for the insight of Prof. Daniel Gamelin and Dr. Kira Hughes Lund into the photophysics data and experimental design.

3.2 INTRODUCTION

Semiconductor nanocrystals (NCs), or quantum dots, have been of great fundamental interest over the past few decades due to their solution processability, and size, shape, and composition tunability. These features also make them attractive for commercial applications including displays, lighting, photovoltaics, and biological sensing.[1–4] Copper-doped NCs, however, have captured recent attention because they exhibit Stokes-shifted emission and long photoluminescence (PL) lifetimes, properties that reflect copper's presence as a dopant in the NC lattice.[5–11] These features are particularly attractive for the design of near-infrared emitters for use in luminescent solar concentrators due to the NCs' low reabsorption and the advantageous location of the copper-based PL relative to the band gap of traditional silicon photovoltaics.[12,13] The PL in copper-doped semiconductors is attributed to localization of photogenerated valence-band holes at the Cu^{+} dopants following inter-band photoexcitation, formally forming Cu^{2+} in a luminescent mid-gap charge-transfer (CT) excited state.[5,14] The nuclear reorganization associated with hole localization gives the copper-based PL its characteristic broad linewidth and the CT nature of the excited state contributes to its long lifetime.

Understanding charge-carrier traps is fundamental to developing the highly luminescent materials needed for a range of semiconductor technologies, including displays and photovoltaics. To be industrially relevant, NCs must have high PLQYs and narrow PL linewidths. Although CdSe NCs with near-unity PLQYs have been obtained and are now fundamentally well-understood, synthesizing NCs of non-toxic alternatives (*e.g.*, III-V materials) that possess similar physical properties has proven challenging.[15] Indium phosphide (InP) NCs are an exciting and commercially proven alternative to cadmium-based materials, given their inherently lower toxicity and similar optical properties.[16,17] Recent developments in InP NC syntheses have separately produced ensembles that are monodisperse and highly photo- and electroluminescent, albeit with broader PL line widths than their CdSe analogs.[18,19] Despite these advances, the underlying principles governing the increase in PLQY are still under question. Various literature reports highlight the passivation of electron or hole traps, but the extent to which each trapping mechanism impacts the PL of InP NCs is debated.[20–22]

Using copper as an "engineered" hole trap offers a unique opportunity to examine carrier dynamics in NCs that is complimentary to the study of undoped NCs. By preparing Cu^{+}:InP NCs via a new, bottom-up method enabled by an aminophosphine-based synthesis, we can analyze the charge-carrier dynamics as a function of different post-synthetic surface treatments and correlate increases in PLQY with reduction in surface carrier trapping. Copper can be incorporated into the InP NCs either through this bottom-up method during synthesis or via a post-synthetic cation exchange reaction. The copper-doped cores can then be treated with Lewis acids, specifically zinc carboxylate, to increase the PLQYs using a method pioneered by our lab, while maintaining dopant incorporation.[23,24] Similar to prior literature reports, shelling the doped cores proved challenging due to copper migration from the NCs under traditional shelling conditions.[6] However, we were

able to post-synthetically incorporate copper into thinly shelled InP/ZnSe NCs, inspired by an approach used for doping CdSe/CdS NCs.[14] All samples were then spectroscopically probed utilizing time-resolved photoluminescence spectroscopy (TRPL) to study the recombination dynamics of the conduction-band electron and copper-localized hole.

3.3 Results and Discussion

Aminophosphines have recently generated interest as relatively environmentally benign phosphorus sources for the synthesis of a range of metal phosphide NCs.[25–30] Changing the identity of the indium and cadmium halide precursors, for example, produces size tunable InP or Cd_3P_2 NCs.[26,29] Given the previously established reactivity of aminophosphines with transition metals, we hypothesized that this system may provide an excellent synthetic platform for generating doped InP NCs. Prior experiments in our lab showed the formation of crystalline Cu_3P platelets from $CuCl_2$ and tris(diethylamino)phosphine (Figure 3.1).

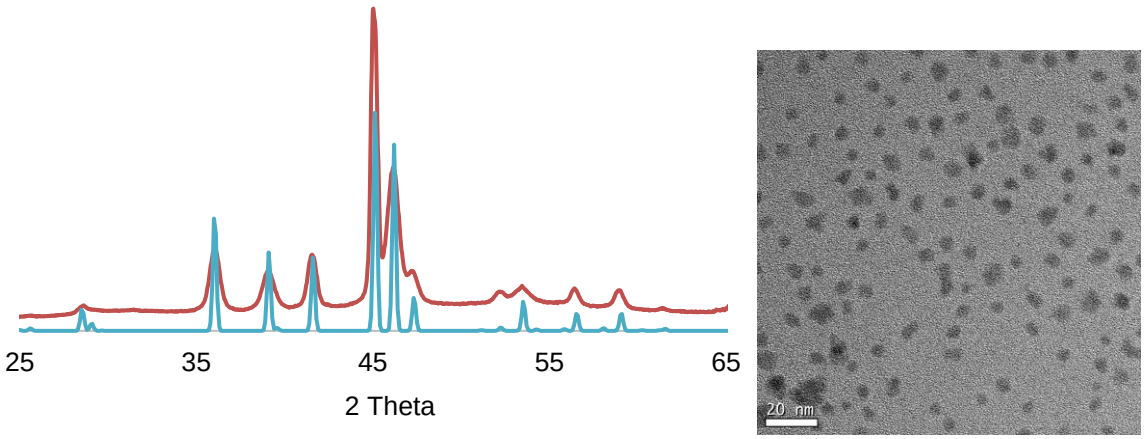

Figure 3.1. (Left) P-XRD spectrum of product of reaction of $P(NEt_2)_3$ and $CuCl_2$ (orange) with Cu_3P standard pattern (blue, pdf 01-071-2261 ICSD) and (right) TEM image showing clear evidence of crystalline copper phosphide.

3.3.1 *Synthesis of Cu^+:InP*

Although this result indicated the amenability of the system to forming Cu—P bonds, it also presented a challenge of preventing preferential formation of separate crystalline phases of Cu_3P and InP. This was recently seen in synthetic conditions where the presence of copper diverted significant phosphorus and allowed the formation of small InP NCs.[31] Although other reports gave no indication of formation of Cu_3P under doping conditions, we found that this impurity persisted when the aminophosphine was injected into a solution containing both the indium and copper halides.[32,33] To circumvent this detrimental reactivity, we delayed the introduction of the copper halide by 5 min allowing the InP to nucleate. Operationally, we used a syringe pump to add a solution of copper chloride in oleylamine over 30 min. The dropwise addition also maintained a relatively low concentration of copper to prevent monomers from reaching critical concentration and separately nucleating Cu_3P.

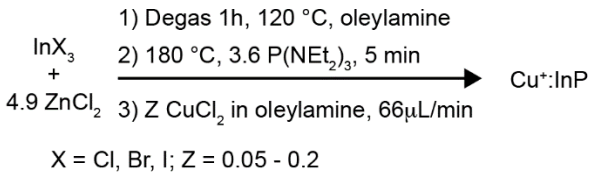

Figure 3.2. Reaction scheme for bottom-up Cu^+:InP synthesis.

With our procedure established, we successfully synthesized Cu^+:InP NCs. As seen in Figure 3.3, the NCs synthesized with Z = 0.2 equivalents of copper and $InCl_3$ exhibit the characteristic tetrahedral morphology and 3.2 nm diameter associated with aminophosphine-derived InP NCs.

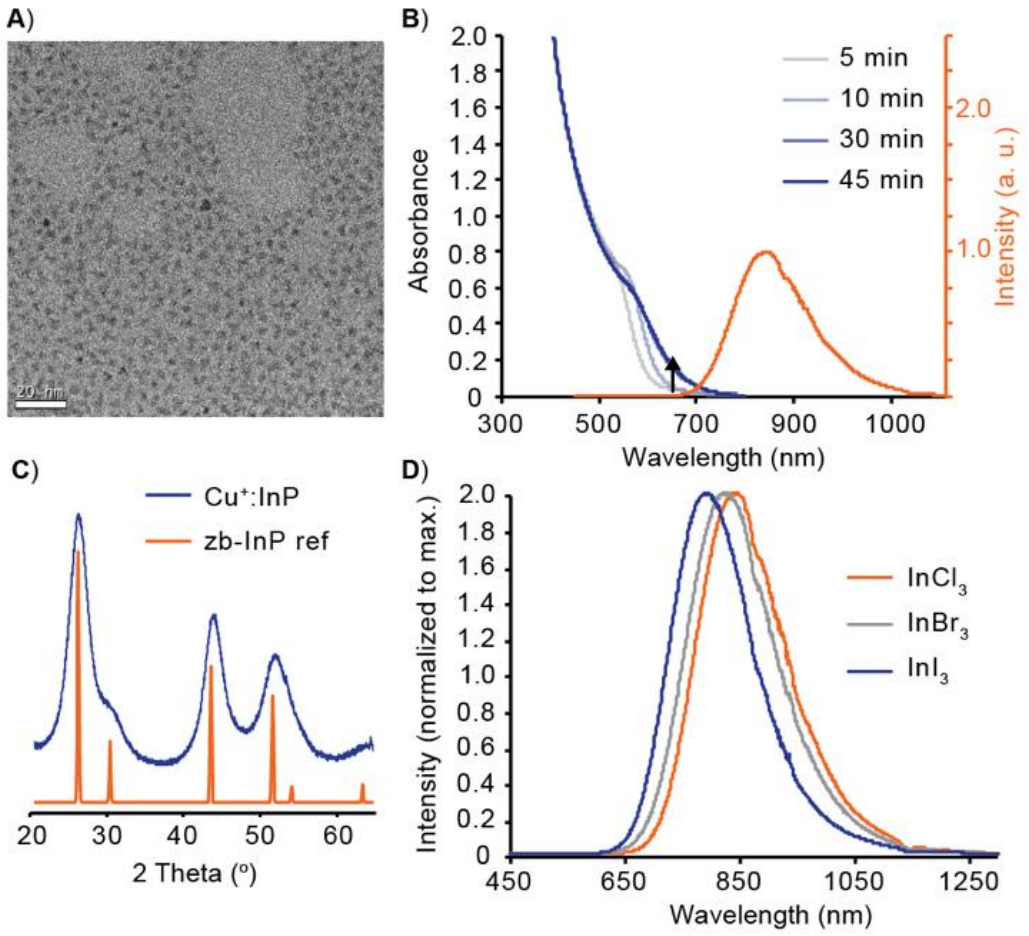

Figure 3.3. A) TEM image of Cu^+:InP NCs derived from aminophosphines and $InCl_3$ showing *d* = 3.2 ± 0.3 nm NCs. B) UV-Vis absorption spectra of reaction progress and final steady-state PL spectrum of representative synthesis of Cu^+:InP NCs (10% PLQY). C) Powder X-ray diffraction pattern of the same NCs showing the only crystalline phase present to be InP (pdf 01-070-2513 ICSD). D) Normalized steady-state PL spectra of copper-doped InP NCs synthesized with different halide precursors to tune the size of the NCs and resulting emission energy.

The optical spectra strongly support copper doping. Addition of copper results in appearance of a broad, red-shifted PL band with its maximum at ~850 nm, and the emergence of

weak near-band-edge absorption at ~650 nm that has been attributed to direct photoexcitation of the luminescent CT excited state.[34] Photoluminescence excitation (PLE) measurements monitoring the emission at 825 nm show that the NIR emission arises from NC photoexcitation (Figure 3.4).

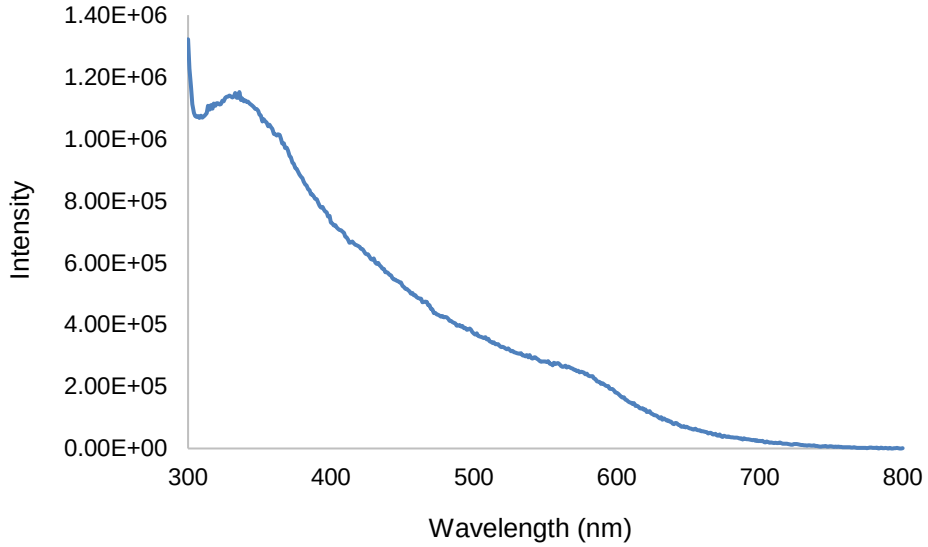

Figure 3.4. Photoluminescence excitation monitored at 825 nm. The feature at 585 nm corresponds to the excitonic absorbance in the UV-Vis spectrum shown in Figure 3.3B.

The X-ray powder diffraction pattern (Figure 3.3C) is consistent with InP as the sole crystalline phase and inductively coupled plasma optical emission spectroscopy (ICP-OES) confirms the presence of copper in the NCs. Together, these data constitute strong support for incorporation of copper ions in the NC lattice. These NCs exhibit a high PLQY directly out of synthesis, ranging from 8 – 25%. We found that the PLQY decreases when the reaction scale is increased, likely due to variations in heating profile that lead to less uninform copper incorporation.

We investigated the tunability of this reaction with regards to NC size and amount of copper incorporated. By altering the amount of copper added to the reaction (Z in Figure 3.2), the indium-to-copper ratio in the final products could be modestly tuned (Table 3.2).

Table 3.2. ICP-OES elemental ratios of nanocrystals formed under various synthetic conditions.

Sample	Indium	Phosphorous	Copper	Zinc	Selenium
$InCl_3$ 10:1 In:Cu	1.2	1	0.07	n/a	n/a
$InCl_3$ 20:1 In:Cu	1.3	1	0.08	n/a	n/a
$InCl_3$ 40:1 In:Cu	1.2	1	0.04	n/a	n/a
$InBr_3$	1	1	0.1	n/a	n/a
InI_3	1	1	0.13	n/a	n/a
Zinc treated	1	1	0.07	0.8	n/a
Thin shelled	1.3	1	0.1	0.2	0.8
$CuBr_2$	1	1	0.25	n/a	n/a

We found that the upper limit was an In:Cu ratio of 17:1 (5.6% replacement of In), achieved with a starting In:Cu ratio of 10:1 or 20:1 in the reaction mixture. This NC doping level corresponds to incorporation of approximately 12 copper atoms per NC. When the starting ratio of In:Cu was changed to 40:1 the corresponding In:Cu ratio was decreased to 33:1, corresponding to 6 copper per nanocrystal. Higher levels of copper incorporation could be attained by changing the copper source to the more reactive copper(II) bromide, which gave an In:Cu ratio of 4:1 while maintaining the InP crystal phase (Figure 3.5). However, this synthesis did not result in an increased PLQY or a dramatic shift in the PL peak position.

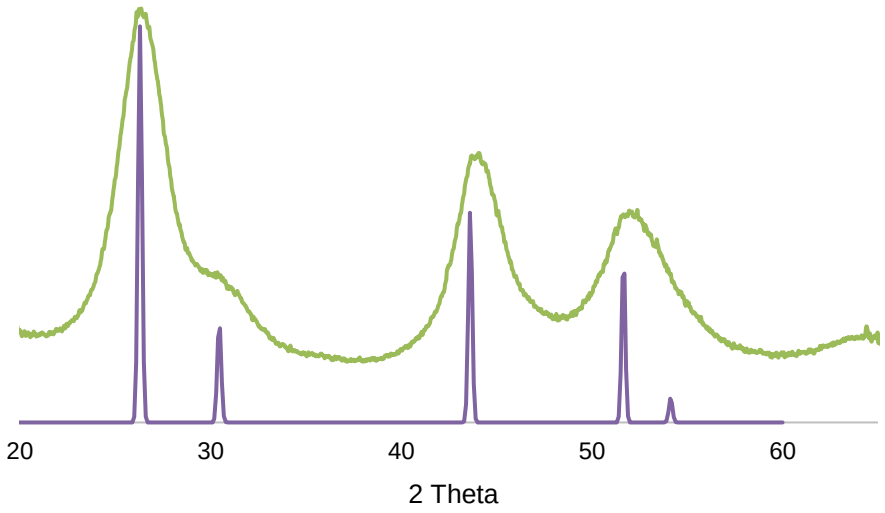

Figure 3.5. P-XRD spectrum (gray) of nanocrystals formed by reacting $InCl_3$ and $P(NEt_2)_3$ according to Scheme 1 and doped using $CuBr_2$ instead of $CuCl_2$ as the copper precursor. Reference bulk InP pattern (yellow, pdf 01-070-2513 ICSD).

The NC size could be tuned following established literature procedures for aminophosphine-derived InP NCs.[26] By replacing $InCl_3$ with either $InBr_3$ or InI_3 as the indium source and utilizing our standard slow injection procedure, we also synthesized 3.0 nm and 2.8 nm diameter Cu^+:InP NCs with PLQYs of 15% and 18%, respectively (Figure 3.6). These changes in size were accompanied by a corresponding blue shift in the copper PL peak for the smaller NCs, as seen in Figure 1D. Our data agree with prior reports of the tunability of both the copper PL and host NC size.[6] The size changes were accompanied by increases in the level of copper incorporation, which could be attributed to increased reactivity of the copper precursor due to partial ligand scrambling at elevated temperatures.[35,36]

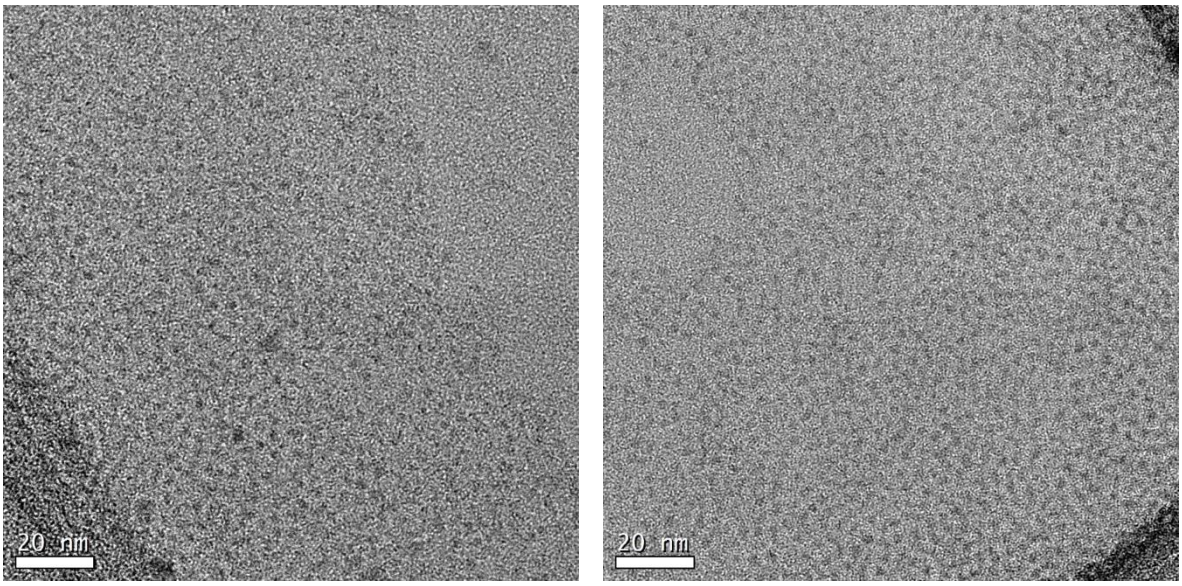

Figure 3.6. TEM images of Cu^{+}:InP NCs synthesized from $InBr_3$ (left) and InI_3 (right).

3.3.2 *Post-synthetic modifications of doped NCs*

An advantage of Cu^{+}:InP NCs as a material for photophysical study is the localization of the hole at the copper.[5] Recent work from our group has posited both hole trapping and electron trapping are present and account for the typically low PLQY of as-synthesized InP NCs.[20] It is hypothesized that the electron traps can be addressed by exchanging under-coordinated indium atoms at the surface via treatment with lower-valent Lewis acids, specifically for M^{2+} carboxylates.

Despite prior reports of moderate copper stability within InP NCs, under traditional shelling and Lewis acid treatment conditions, excitonic PL re-emerged, signaling copper loss from a subset of NCs (Figure 3.7).

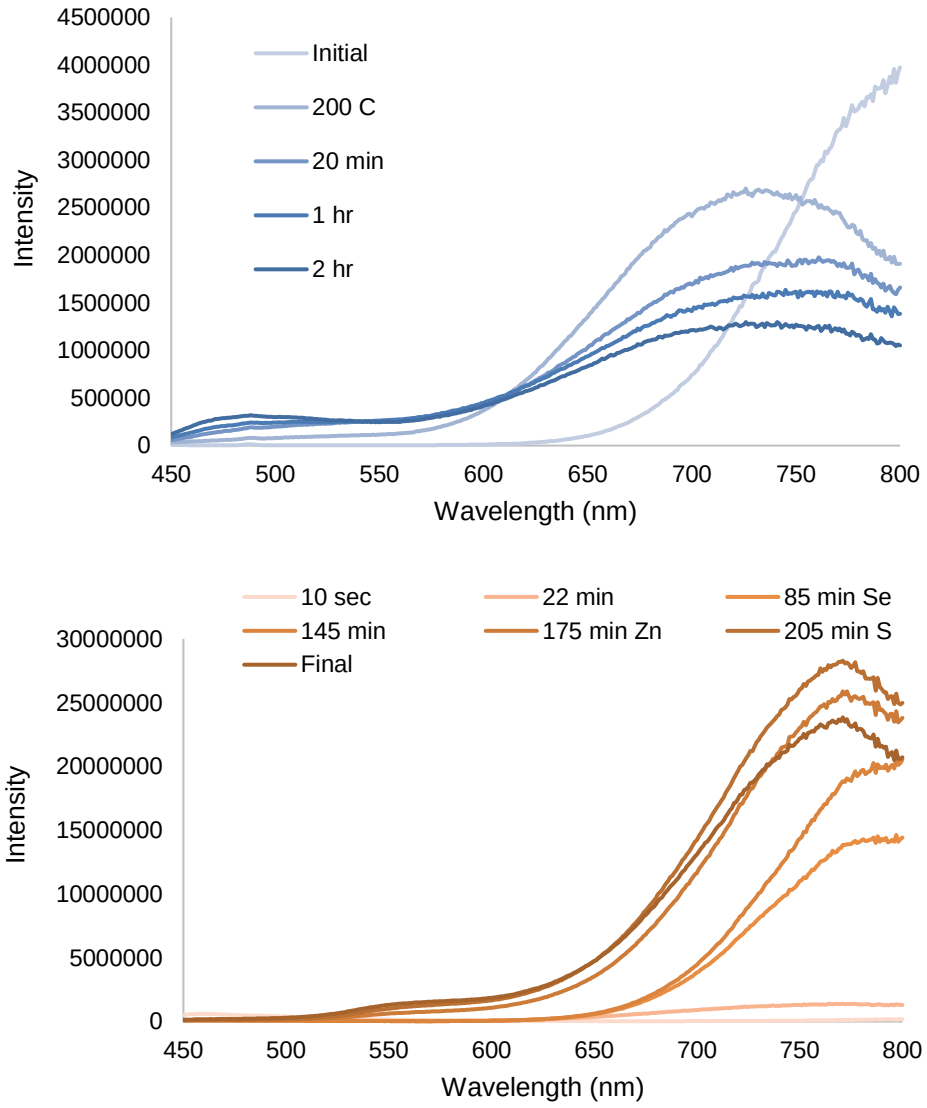

Figure 3.7. Photoluminescence spectra of copper doped samples during standard Lewis acid treatment with zinc stearate (top) and using a modified ZnSeS shelling procedure (bottom). Both spectra show the emergence of excitonic luminescence below 600 nm.

This instability necessitated using lower temperatures, 100 °C compared to 200 °C, for the Lewis acid treatment with zinc stearate. At 100 °C, treatment with zinc carboxylate results in the ratio of In:Cu being maintained by ICP (Table 3.2), while inducing an increase in PLQY from 10% to 20% for Cu^{+}:InP/Zn NCs with no evidence of excitonic luminescence (Figure 3.8). The standard

aminophosphine reaction contains an excess of zinc in the nucleation pot, which has been shown to increase the monodispersity of the final NCs and likely creates a zinc-rich surface that facilitates shell growth.[28,30] However, the treatment we performed with the zinc carboxylates clearly alters the surface chemistry and passivates defects in a way the zinc halides cannot.

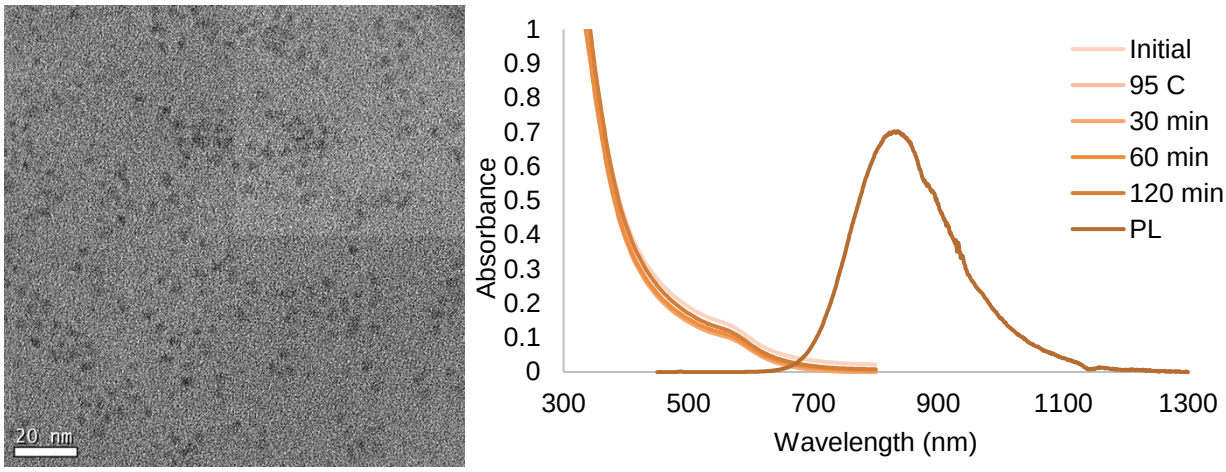

Figure 3.8. TEM of zinc carboxylate treated Cu:InP NCs (left) and UV-Vis and final PL spectrum showing the continued presence of copper in the nanocrystal (right).

Prior reports have shown cadmium carboxylates strongly interact with the InP surface and are highly successful agents for passivating electron traps.[20] In this study, we found cadmium treatment incompatible with the doped materials; at temperatures high enough for PLQY enhancement we observed the dopant leaving the NCs (Figure 3.9). This might be due to alloying of cadmium into the surface, disrupting the lattice and accelerating copper loss.[23,37]

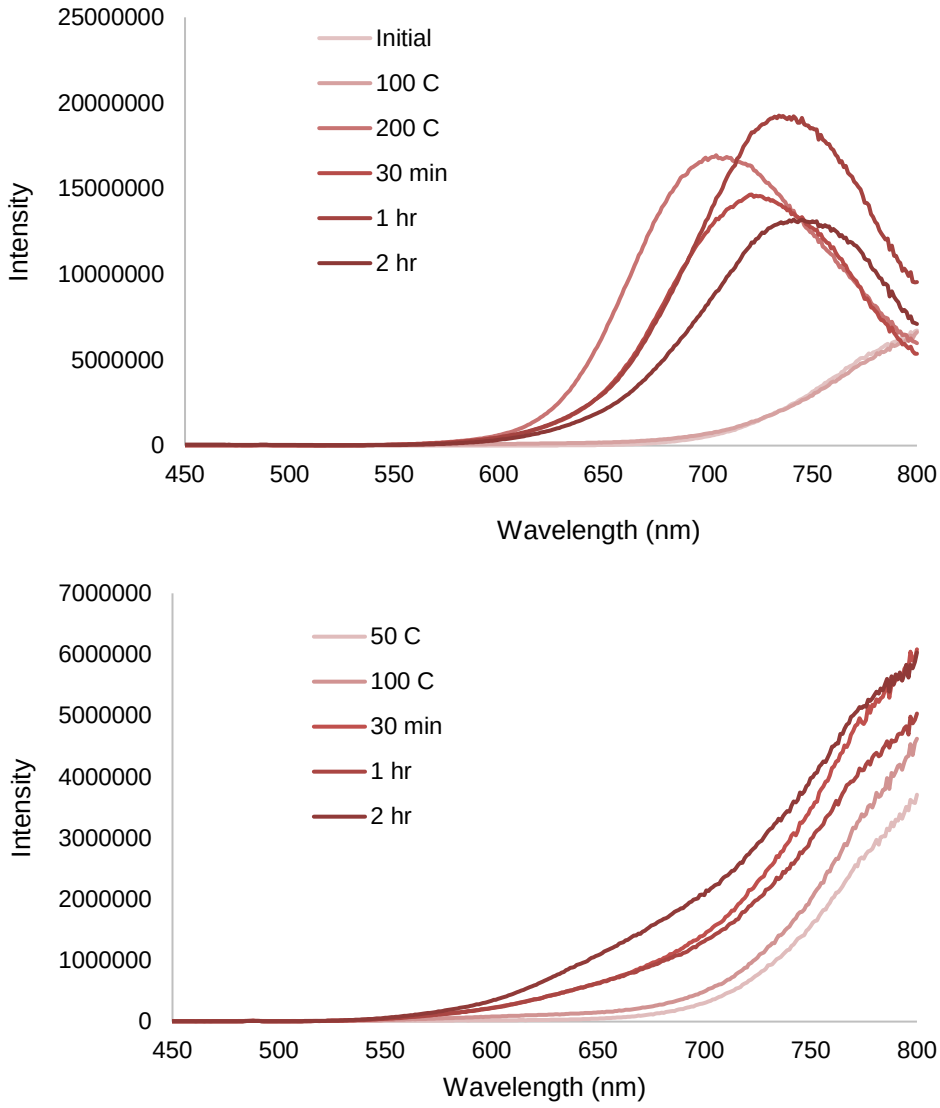

Figure 3.9. Photoluminescence spectra of Cu:InP NCs after cadmium oleate treatment at 200 °C (top) or 100 °C (bottom).

Shelling of previously doped NCs resulted in partial migration of copper from the lattice under a range of conditions, as reported in the literature.[26,33] Such samples demonstrated extremely high PLQY, over 60% for the copper peak alone, but the presence of both doped and undoped NC populations in the sample limited their usefulness for spectroscopic study (Figure 3.10). To our

knowledge, this quantum yield is the highest reported for Cu^{+}:InP, as prior studies report copper-based PLQY only up to 40%, making this a dramatic, 20% increase in PLQY.[6,9,11,32]

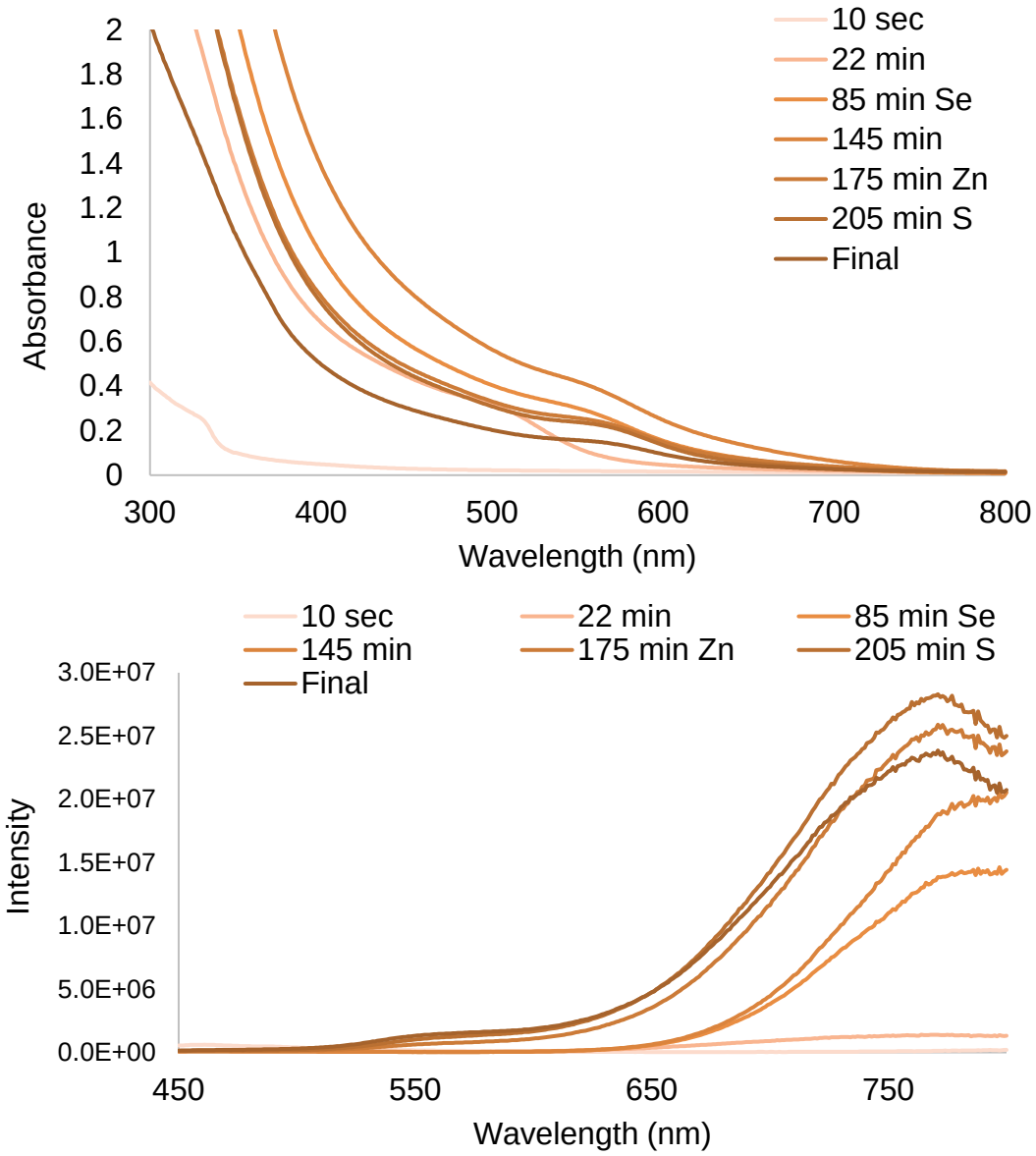

Figure 3.10. Absorption spectra of Cu^{+}:InP NCs thickly shelled *in-situ* with ZnSeS. The UV-Vis (top) shows the development of sub-band gap absorbance associated with the so-called "copper foot" and retention of the InP excitonic absorption while the PL spectra (bottom) show both the distinct copper luminescence and the presence of excitonic luminescence around 565 nm.

As mentioned above, copper can be post-synthetically doped into InP NC cores and has been previously shown to incorporate post-synthetically into II-VI NCs with thin shells.[6,14] Using this established precedent, we explored copper incorporation in thinly (~1 monolayer) ZnSe-shelled InP NCs via cation exchange.[6,14] A copper chloride solution was added after shelling, and within 2 h the excitonic PL disappeared and the characteristic copper PL dominated the spectrum, with a PLQY of 40% (Figure 3.11).

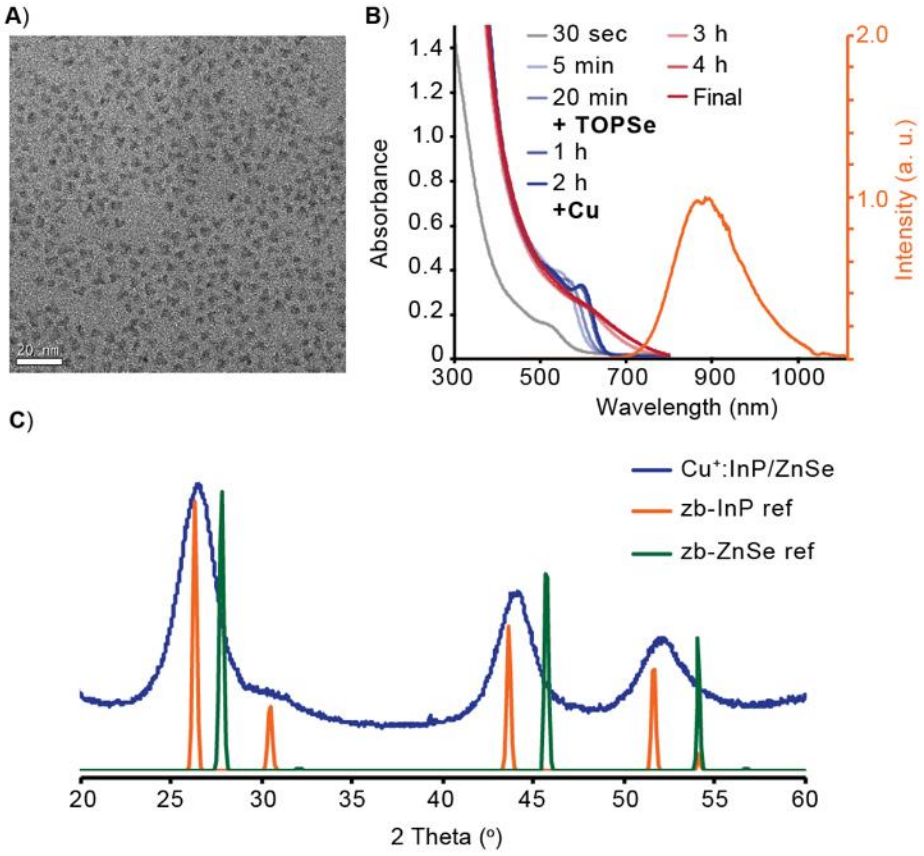

Figure 3.11. A) TEM of Cu^+:InP/ZnSe NCs showing $d = 4.2 \pm 0.4$ nm NCs. B) UV-Vis absorption spectra of reaction progress and final steady-state PL spectrum of a representative synthesis of Cu^+:InP/ZnSe NCs (40% PLQY). C) Powder X-ray diffraction pattern of the same NCs showing crystalline phase present to be primarily InP (pdf 01-070-2513 ICSD) with slight shifts towards ZnSe (pdf 01-071-5977 ICSD).

An initial 10:1 In:Cu molar ratio produced NCs with a final In:Cu ratio of 14:1, similar to the upper limit seen in the bottom-up synthesis. Thick-shelled InP NCs were also doped via the same method, however the time needed for copper diffusion exceeded 12 h (Figure 3.12) with no comparative increase in PLQY relative to the thinly shelled materials.

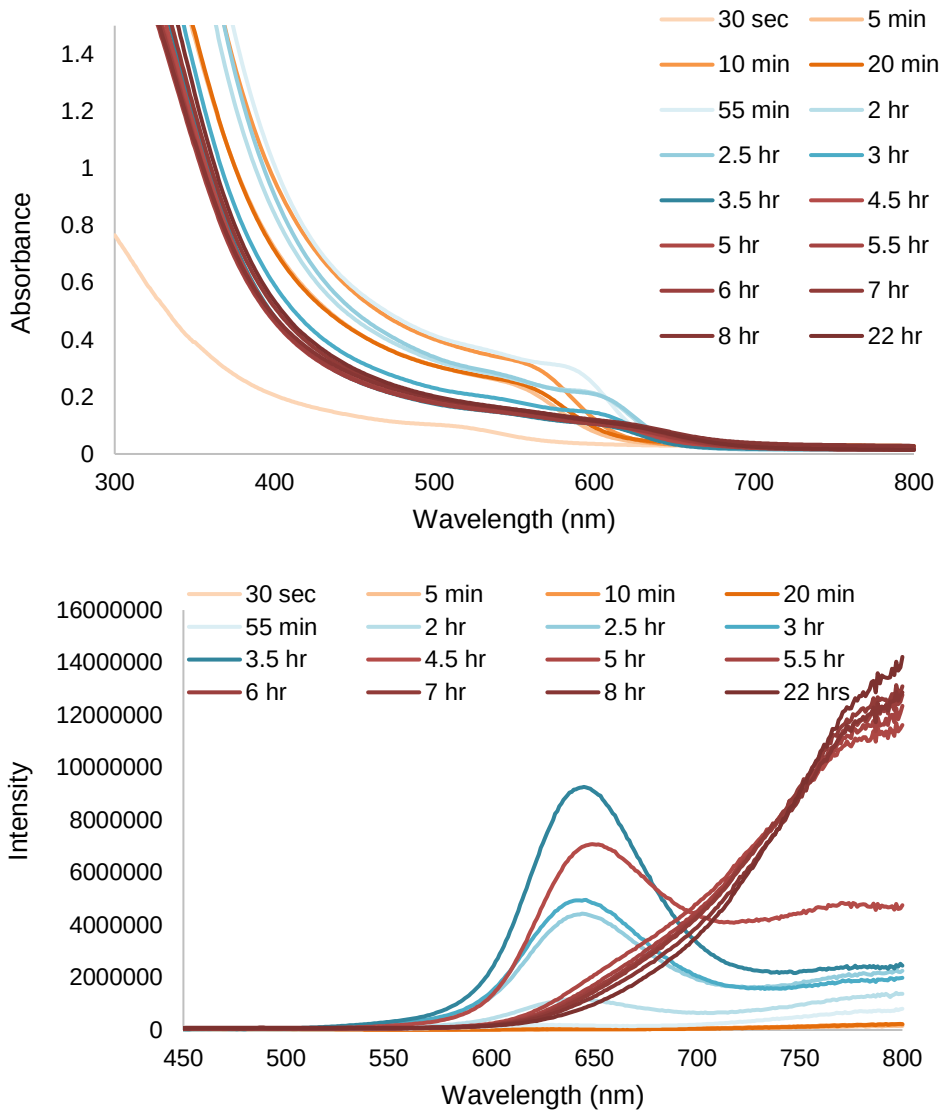

Figure 3.12. A) TEM Absorption and PL spectra collected during post-synthetic treatment of thickly shelled InP/ZnSeS NCs with a copper chloride and oleylamine solution at 210 °C for a period of 22 h. The UV-Vis absorption spectra (top) show the development of sub-band gap absorbance associated with the so-called “copper foot” while the PL spectra (bottom) show the

diminishment of the excitonic luminescence and the emergence of the distinct copper luminescence.

Previous work shows that native carboxylate-ligated InP NCs exhibit electron trapping at undercoordinated indium sites within ~10 ns and sub-nanosecond hole trapping.[20,21] These trap states can be passivated by various surface treatments; in the case of our aminophosphine NCs, a zinc carboxylate treatment passivates electron traps by either exchanging with under-coordinated indium ions on the NC surface or with datively bound Lewis bases like primary amine, while zinc chalcogenide shelling can passivate both electron and hole traps.[20]

3.3.3 *Photophysical characterizations*

As discussed above, upon introduction of Cu^+ into the InP NC lattice, the PLQY increases from ~1% to 10%, suggesting that the Cu^+ competes effectively with native surface traps for capture of the photogenerated hole. However, it is likely that a PLQY of only 10% still indicates the presence of significant carrier trapping at the NC surface. Therefore, the previously mentioned surface treatments should help remove potential trap sites and increase the sample PLQY. We used time-resolved photoluminescence (TRPL) spectroscopy to study recombination of the photogenerated delocalized conduction-band electron with the copper-localized hole as a function of these NC surface treatments.

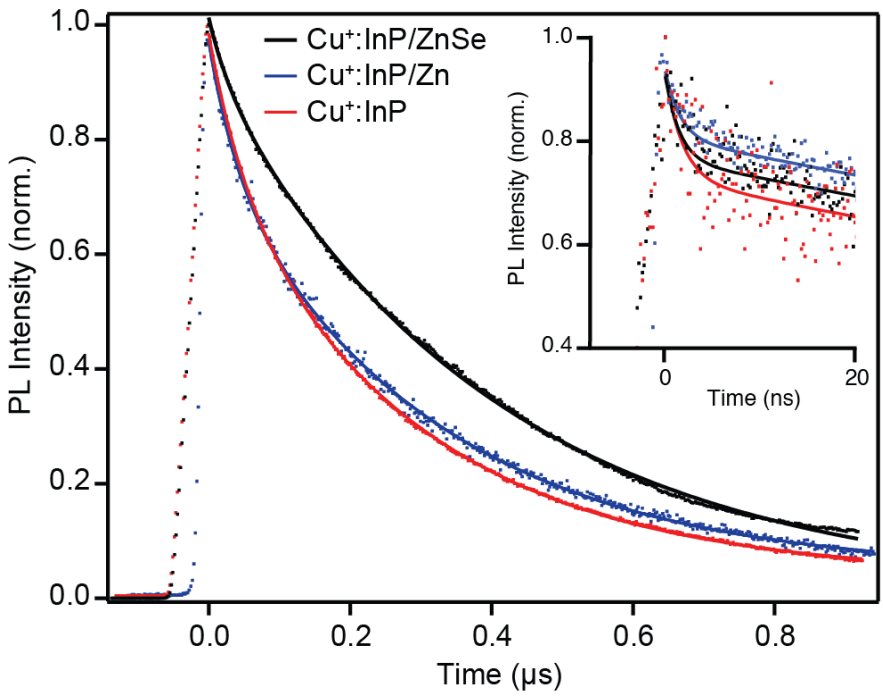

Figure 3.13. Normalized PL decay dynamics of the copper PL for Cu^+:InP NCs (red), Cu^+:InP/Zn NCs (blue), and Cu^+:InP/ZnSe NCs (black). The inset shows the first 20 ns of data collected in a 100 ns window (Figure S10). All data were collected at room temperature on NCs suspended in dry toluene. The untreated Cu^+:InP NCs (red) show the fastest decay and have the lowest PLQY of 10%, followed by the Cu^+:InP/Zn (blue, PLQY of 20%), and finally the shelled Cu^+:InP/ZnSe NCs (black) show the longest lifetime and highest PLQY of 40%. PL decay curves were obtained by integrating between 880 and 780 nm.

Figure 3.13 shows PL decay curves measured for Cu^+:InP, Cu^+:InP/Zn, and Cu^+:InP/ZnSe NCs, plotted on a 1 μs window. Fitting the PL decay of the untreated Cu^+:InP NCs to a biexponential function gives a weighted PL lifetime of 233 ns (see Table 3.3 for fitting parameters). This result aligns well with previous reports of long luminescence lifetimes in copper-doped NCs, but the decay here is slightly faster than the ~500 ns lifetime reported for Cu^+:InP/ZnS/InP/ZnS

NCs.[38] This discrepancy could be due to a difference in physical structures between the two materials, or it could indicate that our system still has competing carrier trapping pathways.[17] The PL decay of the Cu^+:InP/Zn NC sample is nearly identical (Figure 3.13), with a weighted lifetime of 251 ns. The Cu^+:InP/ZnSe NC sample, however, has a much longer lifetime of 367 ns, indicating the efficiency with which even a thin layer of ZnSe can eliminate surface traps. Because TRPL gives information about both photogenerated electrons and holes, we are not able to unambiguously identify the contributions of either charge carrier to these dynamics at this stage.

Table 3.3. Fitting parameters for time resolved photoluminescence decay dynamics (fitting window of 1μs – Figure 3.13).

	A1	**τ1 (us)**	**A2**	**τ2 (us)**	**Weighted τ**
Cu^+:InP:ZnSe	0.098	0.036	0.913	0.415	0.383
Cu^+:InP:Zn	0.315	0.078	0.632	0.430	0.313
Cu^+:InP	0.378	0.092	0.588	0.405	0.272

Despite similarities in the decay dynamics for the Cu^+:InP and the Cu^+:InP/Zn NC samples, the PLQY of the Cu^+:InP/Zn NCs is 20%, double that of the Cu^+:InP NCs. Therefore, we also examined the PL decay dynamics on a 100 ns timescale (Figure 3.13 inset) to attempt to observe faster processes. The Cu^+:InP and Cu^+:InP/Zn NCs appear to have very similar decay dynamics on this timescale as well, but the Cu^+:InP NCs decay almost twice as much as the Cu^+:InP/Zn NCs in the first ~2 ns. This result shows that the Zn-carboxylate surface treatment doubles the PLQY by eliminating trapping processes that occur on this timescale. The Cu^+:InP/ZnSe NCs also exhibit less ~2 ns decay than the Cu^+:InP NCs, and their slower decay on the 1 μs time scale accounts for their higher PLQY than the Cu^+:InP/Zn NCs.

3.4 Conclusions

In summary, we have developed a synthetic route to access highly luminescent copper-doped InP NCs from aminophosphine and metal-halide precursors. The copper content can be tuned by altering initial molar ratios or through post-synthetic cation exchange and the copper PL energy shifted by changing the indium precursor, which controls the size of the final NCs. Upon surface modification, either by Lewis acid treatment with zinc carboxylate or by growth of a thin ZnSe shell, the PLQY increases. This PLQY increase correlates with the decrease of a ~2 ns PL decay component, and in the case of the Cu^+:InP/ZnSe NCs also with slower PL decay over the subsequent hundreds of nanoseconds. This work demonstrates that similar trapping processes occur in doped and undoped InP NCs, and that surface treatments first developed for undoped InP NCs are effective in eliminating competing trap pathways in doped InP NCs as well. We are able to synthesize highly luminescent Cu^+:InP NCs and demonstrate the applicability of post-synthetic surface modification for doped NC emitters.

3.5 Experimental Details

All glassware was dried in a 160 °C oven overnight prior to use. All reactions were run under an inert atmosphere of nitrogen using a glovebox or standard Schlenk techniques. Zinc chloride (>98%), tris-diethylaminophosphine (97%), copper (II) chloride (≥98%), indium (III) chloride (97%), indium (III) bromide (99%), and anhydrous isopropanol were purchased from Millipore-Sigma, stored in a nitrogen glovebox or desiccator, and used without further purification. Indium iodide (99%), copper (I) chloride (anhydrous 97%+), and copper (II) bromide (99%) were purchased from Strem Chemicals Inc., stored in a nitrogen glovebox or desiccator, and used without further purification. All other solvents including oleylamine, pentane, and toluene were

purchased from Sigma Aldrich Chemical Co., dried over CaH_2, distilled, and stored over 4 Å sieves in a nitrogen glovebox. Omni Trace nitric acid was purchased from EMD Millipore and used without purification. 18.2 MΩ water was collected from an EMD Millipore water purification system. ^{31}P NMR spectra were collected on a 500 MHz Bruker Avance spectrometer. UV-Vis spectra were collected on a Cary 5000 spectrophotometer from Agilent. TEM images were collected on a FEI Tecnai G2 F20 microscope using an ultrathin carbon film on holey carbon purchased from Ted Pella Inc. P-XRD diffractograms were collected a Bruker Microfocus instrument. Luminescence spectra were collected on an Edinburgh FLS 1000 fluorimeter. Photoluminescence quantum yields were measured with a Hamamatsu integrating sphere.

Standard doped indium phosphide reaction procedure

0.45 mmol of an indium halide, 2.2 mmol $ZnCl_2$, and 5 mL of dried and distilled oleylamine were added to a 25 mL 3-neck flask. The solution was then placed under vacuum at 120 °C and degassed for 1 hour. The vessel was then placed under an inert atmosphere and heated to 180 °C. Once the reaction temperature was reached, 0.45 mL of tris-diethylaminophosphine (1.6 mmol) was rapidly injected. The reaction was allowed to proceed for 5 minutes after which the previously prepared copper halide solution was slowly injected (2 mL at 4 mL/hr). The flask was then cooled down to room temperature before being moved into a nitrogen glovebox for purification. The nanocrystals were precipitated with anhydrous methanol or isopropanol, centrifuged at 7830 rpm, and suspended in toluene. This procedure was repeated 5 times before any additional sample analysis was performed.

Thin shelled doped indium phosphide reaction procedure

0.23 mmol of an indium halide, 1.1 mmol of $ZnCl_2$, and 2.5 mL of dried and distilled oleylamine were added to a 15 mL 3-neck flask. The solution was then placed under vacuum at 120 °C and degassed for 1 hour. The vessel was then placed under an inert atmosphere and heated to 180 °C. Once the reaction temperature was reached, 0.23 mL of tris-diethylaminophosphine (0.8 mmol) was rapidly injected. The reaction was allowed to proceed for 20 minutes after which 0.5 mL of the previously prepared 1M TOPSe was slowly injected. At 60 minutes the temperature was increased to 200 °C and held there for an hour. At 120 minutes, the temperature was decreased to 150 °C. Once temperature was reached the copper halide solution was slowly injected (1 mL at 2 mL/hr). After the injection had completed the temperature was increased to 210 °C and held there for 1.5 hours. The flask was then cooled down to room temperature before being moved into a nitrogen glovebox for purification. The nanocrystals were precipitated with anhydrous methanol or isopropanol, centrifuged at 7830 rpm, and suspended in toluene. This procedure was repeated 5 times before any additional sample analysis was performed.

Zinc stearate treatment procedure

0.1 mmol zinc stearate was degassed in a 15 mL flask. Half of a previously prepared Cu:InP nanocrystal reaction at the 0.45 mmol scale was precipitated once and then resuspended in 4 mL of 1-octadecene. The solution containing approximately 0.2 mmol of indium was injected into the flask containing the zinc stearate at room temperature. The entire solution was gently heated while stirring to 100 °C and held at that temperature for 2 hours. The flask was then cooled down to room temperature before being moved into a nitrogen glovebox for purification. The nanocrystals were precipitated with anhydrous methanol or isopropanol, centrifuged at 7830 rpm, and

suspended in toluene. This procedure was repeated 5 times before any additional sample analysis was performed.

Sample preparation for characterization

For PXRD samples, insoluble powders were placed onto a piece of double-sided tape on a silicon ⟨100⟩ single crystal wafer. Solvent was removed from colloidal samples until dryness was achieved and then the paste was spread on a silicon ⟨100⟩ single crystal wafer. For TEM, samples were suspended in toluene and then drop cast onto a TEM grid and placed under vacuum overnight prior to imaging to ensure full solvent evaporation. ICP-OES: An aliquot of QD solution was dried to generate solid powder. The supernatant was discarded and hydrogen peroxide, followed by an equivalent amount of trace metal grade nitric acid (67%) was added to the powder and digested overnight. 18.2 MΩ water was added to the sample to dilute to a total of 2% acid concentration.

Photophysical characterization methods

Room-temperature TRPL measurements were performed by exciting colloidal NCs at 365 nm via a Coherent Inc./Light Source OPerA optical parametric amplifier, power measured at ∼50 μW. Time-resolved PL spectra were collected using a Hamamatsu streak camera with a synchroscan unit.

3.6 REFERENCES

(1) Talapin, D. V.; Steckel, J. Quantum Dot Light-Emitting Devices. *MRS Bulletin* **2013**, *38* (9), 685–691. https://doi.org/10.1557/mrs.2013.204.
(2) Talapin, D. V.; Lee, J.-S.; Kovalenko, M. V.; Shevchenko, E. V. Prospects of Colloidal Nanocrystals for Electronic and Optoelectronic Applications. *Chem. Rev.* **2010**, *110* (1), 389–458. https://doi.org/10.1021/cr900137k.
(3) Kramer, I. J.; Sargent, E. H. Colloidal Quantum Dot Photovoltaics: A Path Forward. *ACS Nano* **2011**, *5* (11), 8506–8514. https://doi.org/10.1021/nn203438u.

(4) Medintz, I.; Uyeda, H.; Goldman, E.; Mattoussi, H. Quantum Dot Bioconjugates for Imaging, Labelling and Sensing. *Nat. Mater.* **2005**, *4* (6), 435–446. https://doi.org/10.1038/nmat1390.
(5) Knowles, K. E.; Hartstein, K. H.; Kilburn, T. B.; Marchioro, A.; Nelson, H. D.; Whitham, P. J.; Gamelin, D. R. Luminescent Colloidal Semiconductor Nanocrystals Containing Copper: Synthesis, Photophysics, and Applications. *Chem. Rev.* **2016**, *116* (18), 10820–10851. https://doi.org/10.1021/acs.chemrev.6b00048.
(6) Xie, R.; Peng, X. Synthesis of Cu-Doped InP Nanocrystals (d-Dots) with ZnSe Diffusion Barrier as Efficient and Color-Tunable NIR Emitters. *J. Am. Chem. Soc.* **2009**, *131* (30), 10645–10651. https://doi.org/10.1021/ja903558r.
(7) Srivastava, B. B.; Jana, S.; Pradhan, N. Doping Cu in Semiconductor Nanocrystals: Some Old and Some New Physical Insights. *J. Am. Chem. Soc.* **2011**, *133* (4), 1007–1015. https://doi.org/10.1021/ja1089809.
(8) Grandhi, G. K.; Viswanatha, R. Tunable Infrared Phosphors Using Cu Doping in Semiconductor Nanocrystals: Surface Electronic Structure Evaluation. *J. Phys. Chem. Lett.* **2013**, *4* (3), 409–415. https://doi.org/10.1021/jz3021588.
(9) Knowles, K. E.; Nelson, H. D.; Kilburn, T. B.; Gamelin, D. R. Singlet–Triplet Splittings in the Luminescent Excited States of Colloidal Cu+:CdSe, Cu+:InP, and CuInS2 Nanocrystals: Charge-Transfer Configurations and Self-Trapped Excitons. *J. Am. Chem. Soc.* **2015**, *137* (40), 13138–13147. https://doi.org/10.1021/jacs.5b08547.
(10) Cooper, J. K.; Gul, S.; Lindley, S. A.; Yano, J.; Zhang, J. Z. Tunable Photoluminescent Core/Shell Cu+-Doped ZnSe/ZnS Quantum Dots Codoped with Al3+, Ga3+, or In3+. *ACS Appl. Mater. Interfaces* **2015**, *7* (18), 10055–10066. https://doi.org/10.1021/acsami.5b02860.
(11) Hassan, A.; Zhang, X.; Liu, X.; Rowland, C. E.; Jawaid, A. M.; Chattopadhyay, S.; Gulec, A.; Shamirian, A.; Zuo, X.; Klie, R. F.; et al. Charge Carriers Modulate the Bonding of Semiconductor Nanoparticle Dopants As Revealed by Time-Resolved X-Ray Spectroscopy. *ACS Nano* **2017**, *11* (10), 10070–10076. https://doi.org/10.1021/acsnano.7b04414.
(12) Sharma, M.; Gungor, K.; Yeltik, A.; Olutas, M.; Guzelturk, B.; Kelestemur, Y.; Erdem, T.; Delikanli, S.; McBride, J. R.; Demir, H. V. Near-Unity Emitting Copper-Doped Colloidal Semiconductor Quantum Wells for Luminescent Solar Concentrators. *Advanced Materials* **2017**, *29* (30), 1700821. https://doi.org/10.1002/adma.201700821.
(13) Bradshaw, L. R.; Knowles, K. E.; McDowall, S.; Gamelin, D. R. Nanocrystals for Luminescent Solar Concentrators. *Nano Lett.* **2015**, *15* (2), 1315–1323. https://doi.org/10.1021/nl504510t.
(14) Hughes, K. E.; Hartstein, K. H.; Gamelin, D. R. Photodoping and Transient Spectroscopies of Copper-Doped CdSe/CdS Nanocrystals. *ACS Nano* **2018**, *12* (1), 718–728. https://doi.org/10.1021/acsnano.7b07879.
(15) Hanifi, D. A.; Bronstein, N. D.; Koscher, B. A.; Nett, Z.; Swabeck, J. K.; Takano, K.; Schwartzberg, A. M.; Maserati, L.; Vandewal, K.; van de Burgt, Y.; et al. Redefining Near-Unity Luminescence in Quantum Dots with Photothermal Threshold Quantum Yield. *Science* **2019**, *363* (6432), 1199. https://doi.org/10.1126/science.aat3803.
(16) Tarantini, A.; Wegner, K. D.; Dussert, F.; Sarret, G.; Beal, D.; Mattera, L.; Lincheneau, C.; Proux, O.; Truffier-Boutry, D.; Moriscot, C.; et al. Physicochemical Alterations and Toxicity of InP Alloyed Quantum Dots Aged in Environmental Conditions: A Safer by Design Evaluation. *NanoImpact* **2019**, *14*, 100168. https://doi.org/10.1016/j.impact.2019.100168.

(17) Wegner, K. D.; Dussert, F.; Truffier-Boutry, D.; Benayad, A.; Beal, D.; Mattera, L.; Ling, W. L.; Carrière, M.; Reiss, P. Influence of the Core/Shell Structure of Indium Phosphide Based Quantum Dots on Their Photostability and Cytotoxicity. *Frontiers in Chemistry* **2019**, *7*, 466. https://doi.org/10.3389/fchem.2019.00466.
(18) Won, Y.-H.; Cho, O.; Kim, T.; Chung, D.-Y.; Kim, T.; Chung, H.; Jang, H.; Lee, J.; Kim, D.; Jang, E. Highly Efficient and Stable InP/ZnSe/ZnS Quantum Dot Light-Emitting Diodes. *Nature* **2019**, *575* (7784), 634–638. https://doi.org/10.1038/s41586-019-1771-5.
(19) Kim, Y.; Ham, S.; Jang, H.; Min, J. H.; Chung, H.; Lee, J.; Kim, D.; Jang, E. Bright and Uniform Green Light Emitting InP/ZnSe/ZnS Quantum Dots for Wide Color Gamut Displays. *ACS Appl. Nano Mater.* **2019**, *2* (3), 1496–1504. https://doi.org/10.1021/acsanm.8b02063.
(20) Hughes, K. E.; Stein, J. L.; Friedfeld, M. R.; Cossairt, B. M.; Gamelin, D. R. Effects of Surface Chemistry on the Photophysics of Colloidal InP Nanocrystals. *ACS Nano* **2019**. https://doi.org/10.1021/acsnano.9b07027.
(21) Janke, E. M.; Williams, N. E.; She, C.; Zherebetskyy, D.; Hudson, M. H.; Wang, L.; Gosztola, D. J.; Schaller, R. D.; Lee, B.; Sun, C.; et al. Origin of Broad Emission Spectra in InP Quantum Dots: Contributions from Structural and Electronic Disorder. *J. Am. Chem. Soc.* **2018**, *140* (46), 15791–15803. https://doi.org/10.1021/jacs.8b08753.
(22) Richter, A. F.; Binder, M.; Bohn, B. J.; Grumbach, N.; Neyshtadt, S.; Urban, A. S.; Feldmann, J. Fast Electron and Slow Hole Relaxation in InP-Based Colloidal Quantum Dots. *ACS Nano* **2019**. https://doi.org/10.1021/acsnano.9b07969.
(23) Stein, J. L.; Mader, E. A.; Cossairt, B. M. Luminescent InP Quantum Dots with Tunable Emission by Post-Synthetic Modification with Lewis Acids. *J. Phys. Chem. Lett.* **2016**, *7* (7), 1315–1320. https://doi.org/10.1021/acs.jpclett.6b00177.
(24) Kirkwood, N.; Monchen, J. O. V.; Crisp, R. W.; Grimaldi, G.; Bergstein, H. A. C.; du Fossé, I.; van der Stam, W.; Infante, I.; Houtepen, A. J. Finding and Fixing Traps in II–VI and III–V Colloidal Quantum Dots: The Importance of Z-Type Ligand Passivation. *J. Am. Chem. Soc.* **2018**, *140* (46), 15712–15723. https://doi.org/10.1021/jacs.8b07783.
(25) Tessier, M. D.; De Nolf, K.; Dupont, D.; Sinnaeve, D.; De Roo, J.; Hens, Z. Aminophosphines: A Double Role in the Synthesis of Colloidal Indium Phosphide Quantum Dots. *J. Am. Chem. Soc.* **2016**, *138* (18), 5923–5929. https://doi.org/10.1021/jacs.6b01254.
(26) Tessier, M. D.; Dupont, D.; De Nolf, K.; De Roo, J.; Hens, Z. Economic and Size-Tunable Synthesis of InP/ZnE (E = S, Se) Colloidal Quantum Dots. *Chem. Mater.* **2015**, *27* (13), 4893–4898. https://doi.org/10.1021/acs.chemmater.5b02138.
(27) Buffard, A.; Dreyfuss, S.; Nadal, B.; Heuclin, H.; Xu, X.; Patriarche, G.; Mézailles, N.; Dubertret, B. Mechanistic Insight and Optimization of InP Nanocrystals Synthesized with Aminophosphines. *Chem. Mater.* **2016**, *28* (16), 5925–5934. https://doi.org/10.1021/acs.chemmater.6b02456.
(28) Laufersky, G.; Bradley, S.; Frécaut, E.; Lein, M.; Nann, T. Unraveling Aminophosphine Redox Mechanisms for Glovebox-Free InP Quantum Dot Syntheses. *Nanoscale* **2018**, *10* (18), 8752–8762. https://doi.org/10.1039/C8NR01286E.
(29) Mundy, M. E.; Ung, D.; Lai, N. L.; Jahrman, E. P.; Seidler, G. T.; Cossairt, B. M. Aminophosphines as Versatile Precursors for the Synthesis of Metal Phosphide Nanocrystals. *Chem. Mater.* **2018**, *30* (15), 5373–5379. https://doi.org/10.1021/acs.chemmater.8b02206.
(30) Song, W.-S.; Lee, H.-S.; Lee, J. C.; Jang, D. S.; Choi, Y.; Choi, M.; Yang, H. Amine-Derived Synthetic Approach to Color-Tunable InP/ZnS Quantum Dots with High Fluorescent

Qualities. *Journal of Nanoparticle Research* **2013**, *15* (6), 1750. https://doi.org/10.1007/s11051-013-1750-y.
(31) Huang, F.; Bi, C.; Guo, R.; Zheng, C.; Ning, J.; Tian, J. Synthesis of Colloidal Blue-Emitting InP/ZnS Core/Shell Quantum Dots with the Assistance of Copper Cations. *J. Phys. Chem. Lett.* **2019**, *10* (21), 6720–6726. https://doi.org/10.1021/acs.jpclett.9b02386.
(32) Mei, S.; Wei, X.; Yang, D.; Su, D.; Yang, W.; Zhang, G.; Hu, Z.; Yang, B.; Dai, H.; Xie, F.; et al. Color-Tunable Optical Properties of Cadmium-Free Transition Metal Ions Doped InP/ZnS Quantum Dots. *Journal of Luminescence* **2019**, *212*, 264–270. https://doi.org/10.1016/j.jlumin.2019.04.040.
(33) Wei, X.; Mei, S.; Zhang, G.; Su, D.; Xie, F.; Zhang, W.; Guo, R. Enhanced Tunable Dual Emission of Cu:InP/ZnS Quantum Dots Enabled by Introducing Ag Ions. *Applied Surface Science* **2019**, *493*, 605–612. https://doi.org/10.1016/j.apsusc.2019.06.059.
(34) Yang, L.; Knowles, K. E.; Gopalan, A.; Hughes, K. E.; James, M. C.; Gamelin, D. R. One-Pot Synthesis of Monodisperse Colloidal Copper-Doped CdSe Nanocrystals Mediated by Ligand–Copper Interactions. *Chem. Mater.* **2016**, *28* (20), 7375–7384. https://doi.org/10.1021/acs.chemmater.6b02869.
(35) Ruberu, T. P. A.; Albright, H. R.; Callis, B.; Ward, B.; Cisneros, J.; Fan, H.-J.; Vela, J. Molecular Control of the Nanoscale: Effect of Phosphine–Chalcogenide Reactivity on CdS–CdSe Nanocrystal Composition and Morphology. *ACS Nano* **2012**, *6* (6), 5348–5359. https://doi.org/10.1021/nn301182h.
(36) Hunt, C. T.; Balch, A. L. Scrambling of Halide Ligands between Palladium(II) and between Palladium(I) Complexes of Bis(Diphenylphosphino)Methane. Observation of Unusual Temperature-Dependent Phosphorus-31 NMR Chemical Shifts. *Inorg. Chem.* **1982**, *21* (4), 1641–1644. https://doi.org/10.1021/ic00134a073.
(37) Stein, J. L.; Steimle, M. I.; Terban, M. W.; Petrone, A.; Billinge, S. J. L.; Li, X.; Cossairt, B. M. Cation Exchange Induced Transformation of InP Magic-Sized Clusters. *Chem. Mater.* **2017**, *29* (18), 7984–7992. https://doi.org/10.1021/acs.chemmater.7b03075.
(38) Zhang, Z.; Liu, D.; Li, D.; Huang, K.; Zhang, Y.; Shi, Z.; Xie, R.; Han, M.-Y.; Wang, Y.; Yang, W. Dual Emissive Cu:InP/ZnS/InP/ZnS Nanocrystals: Single-Source "Greener" Emitters with Flexibly Tunable Emission from Visible to Near-Infrared and Their Application in White Light-Emitting Diodes. *Chem. Mater.* **2015**, *27* (4), 1405–1411. https://doi.org/10.1021/cm5047269.

APPENDIX A: ATTEMPTS AT THE SYNTHESIS OF INPZNE QUATERNARY ALLOYED NANOCRYSTALS

A.1 INTRODUCTION AND RATIONALE

As the market for large, high quality displays continues to grow, new technologies need to be developed to increase the color gamut of these devices to more closely match the range of colors detectable by the human eye.[1] Of high importance is being able to access red, green and blue color pixels with high color purity. The narrow linewidths associated with quantum dot emission coupled with their facile solution-based synthesis has made them an attractive option for this commercial application.[2] Figure A1 shows the broader range of colors that are possible with a quantum dot sensitized display (black dots) when compared to a traditional HD display that makes use of a YAG phosphor (dashed triangle).[3] Quantum dots are currently used in a variety of displays, notably high-definition televisions and tablets, to produce images with vivid colors. Currently, the best material for these applications is cadmium selenide (CdSe).[4] For CdSe synthetic methods have been developed that allow for the preparation of monodisperse quantum dots with color-pure emission over a range of visible wavelengths, making it well suited to this type of application. However, the high toxicity of cadmium limits the long-term commercial viability of electronic devices containing this material.

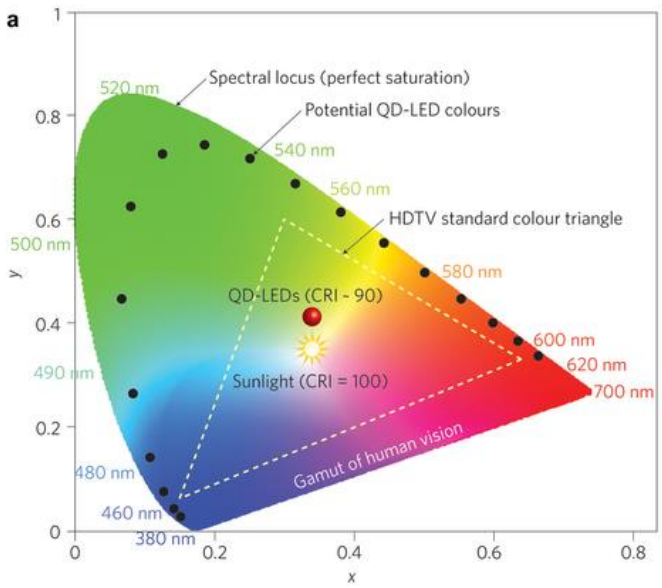

Figure A1. Color range comparison of traditional phosphors with quantum dot displays. Reprinted with permission from reference 3.[3]

In order to accelerate the commercialization of full color gamut display technologies, a material with similar spectroscopic properties and lower toxicity has been sought. Indium phosphide (InP) based materials have entered the display market as the leading non-toxic alternative to CdSe, as they possess similar optical properties without the environmental and health concerns.[4] A feature of InP QDs that has challenged the synthetic chemistry community is the broad luminescence linewidths that result from solution-grown samples.[5] Spectroscopic studies performed on single nanocrystals show that the intrinsic line widths of InP are similar to those of CdSe and that the broadness of the features is due to ensemble effects, specifically general core polydispersity and surface inhomogeneity.[5,6] Additionally, as prepared In-rich InP quantum dots have very low photoluminescence quantum yields, due to a defective surface that introduces mid-gap electron and hole traps.[6–8]

Due to the limitations of as-synthesized InP, new systems need to be devised with higher quantum yields and narrow emission line widths over a range of visible wavelengths. A promising alternative is the quaternary alloyed system InPZnE (E = S,Se), with the bulk of the work performed on the InPZnS system.[9–11] Alloying can be used to control the band gap via composition control rather than size as the zinc chalcogenides have wider band gaps and produce quantum dots with higher energy optical features.[12] Several synthetic methods have been designed to produce these types of alloyed quantum dots. The Reiss group developed a one-pot heat-up synthesis that combines independent molecular indium, phosphorus, zinc, and sulfur precursors.[9] The dots produced have emission maxima ranging from 487 – 587 nm with PLQY of up to 70% and high photostability, particularly when compared to pure InP. One feature of the Reiss method is that a ZnS shell is formed on the particles *in situ*. X-ray photoelectron spectroscopy has allowed for the elucidation of their internal structure; the core consists of a homogeneous alloy with a gradient region becoming more ZnS rich until the shell is reached.[11] A second synthetic method was developed by the Kim group and differs in significant ways.[10] Although four molecular precursors are still used, the indium, zinc, and sulfur precursors are heated to a specific temperature while the phosphorus precursor, $P(SiMe_3)_3$, is slowly added via a syringe pump. This slow addition allows for quantum dots with emission wavelengths of 490 – 630 nm and quantum yields of up to 40% to be formed. They observed that increasing the amount of ZnS hypsochromically shifted the emission features demonstrating that alloys allow for an additional avenue to control electronic properties in these systems.

These alloyed nanoparticle systems have attracted industrial attention due to their advantageous properties. One company, Nanoco, is producing QDs that are presumably alloyed InPZnS using a distinctive approach; a $[Zn_{10}S_4(SPh)_{16}][N(Me)_4]_4$ molecular cluster that acts as a

single source precursor for zinc and sulfur.[13] A similar approach to that of the Kim group is then taken; indium and phosphorus precursors are slowly injected to form QDs. However, the Nanoco procedure uses a series of injections at increasing temperatures to produce progressively larger quantum dots, with emission maxima ranging from 520 – 700 nm and quantum yields ranging from 35 – 90% after post-synthetic modification with HF etching and ZnS shelling. The first set of injections produces the alloyed core particles and we hypothesize that the subsequent sets of injections provide additional indium and phosphorus monomers that grow on the previously nucleated particles in a similar manner to shelling. Despite its appearance in the patent literature and presumed interest for industrial-scale synthesis, very little is known about the mechanism of alloyed QD formation from these types of syntheses.

Notably, the multiple injection synthesis used by Nanoco has disadvantages when compared to a one-pot synthesis. One major advantage of a one-pot synthesis is ease, particularly at an industrial scale. In addition, the multiple-injection process appears to proceed via growth of InP on top of an alloyed core, which may increase the lattice strain at the interface with the eventual ZnS shell. Another issue is that the indium and phosphorus precursors, particularly $P(SiMe_3)_3$, are very reactive when compared to the $[Zn_{10}S_4(SPh)_{16}][N(Me)_4]_4$ cluster. This difference in precursor reactivity could lead to inhomogeneously alloyed particles, as homogenous alloys are more readily accessed using precursors with similar reaction kinetics.[14]

A.2 RESULTS AND DISCUSSION OF INPZNS

Initial work focused on developing a new synthesis for InPZnS alloyed quantum dots based on the commercially utilized Nanoco procedure, but using $In_{37}P_{20}(O_2CR)_{51}$ magic sized clusters

(MSCs) discovered in the Cossairt lab as an indium and phosphorus source.[15] These MSCs have been shown to act as a single-source precursor to highly monodisperse 3 nm InP quantum dots.[16] The clusters can be isolated, purified, and exhibit long term stability under air free conditions. Our hypothesis was that by using a dual cluster approach, the reactivity of the precursors could be more closely matched and thus allow for control over the reaction kinetics leading to monodisperse, homogeneously alloyed quantum dots over a range of sizes. First, the Nanoco procedure was successfully reproduced at a decreased, research scale in our lab in order to provide material for comparison to aid in evaluating the success of the new syntheses. Syntheses using two and three sets of injections were performed to demonstrate that the reported size control could be replicated within the concentrations used in our modified approach. Figure A2 shows the 2.5 nm quantum dots formed in a typical two injection synthesis while the three-injection synthesis produced 3.0 nm dots. The conditions under which the Nanoco procedure was studied were used as starting point for all other new syntheses developed.

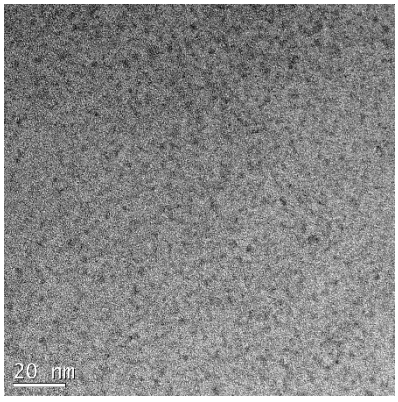

Figure A2. Nanocrystals formed from the two-injection Nanoco procedure modified to a laboratory scale, confirming validity of approach.

After determination of an appropriate concentration regime, an analogue of the two injection Nanoco synthesis was attempted. One slow injection of a solution of the InP MSCs, with

an equivalent amount of phosphorus based on the stoichiometry of the cluster to that used in the two injection Nanoco synthesis, was added to the solution of the $[Zn_{10}S_4(SPh)_{16}][N(Me)_4]_4$ molecular cluster at 175 °C. Although the Nanoco prepared QDs were synthesized at 140 °C, it was necessary to use higher temperatures to overcome the thermal stability of the InP MSCs and liberate In and P. Due to the deviation in heating temperature, the Nanoco procedure was additionally replicated at 175 °C in order to provide a valid comparison between synthetic methods. The MSC persists upon injection at 175 °C, which undermines its use in a hot injection synthesis, where rapid availability of monomers to enable burst-like nucleation is desired. Based on the high stability of the MSC under these reaction conditions, we explored the use of a heat up approach. The primary benefit to the heat up method is its ease; all precursors are added to the reaction mixture at the outset and the flask is then heated to the growth temperature. Additionally, because the clusters do not immediately decompose at 175 °C, the heat up method is more compatible with slow monomer release. Thus, the heat up method was used for additional studies on the nucleation and growth of the nanocrystals.

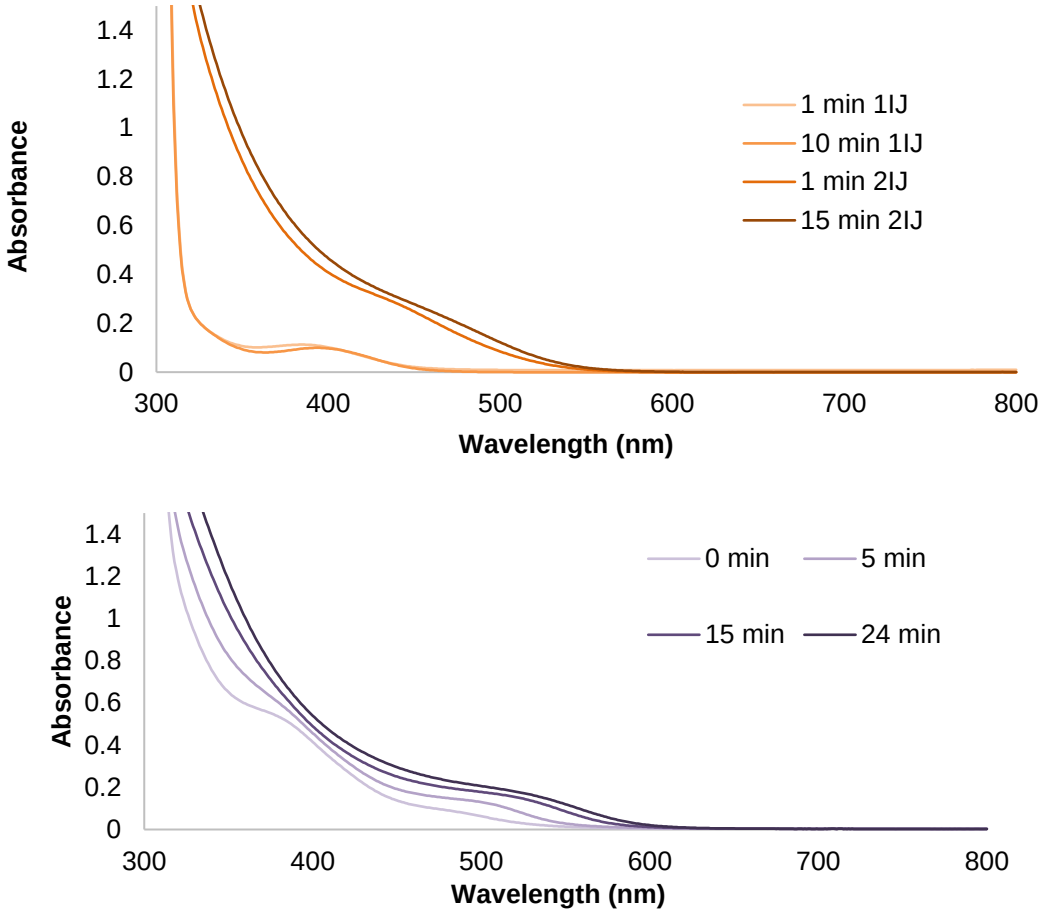

Figure A3. UV-Vis spectra of a typical (top) heat up using MSCs and (bottom) two injection (IJ) Nanoco reaction using individual molecular precursors.

In comparing the dots synthesized via the Nanoco procedure versus the dual cluster method, clear differences are seen. As shown in Figure A3, the lowest energy electronic transition (LEET) of the dots shifts towards longer wavelengths when the MSCs are used as the precursor, from 485 nm to 540 nm, implying the formation of larger or more InP rich dots. A significant size difference has been confirmed via TEM (TEM); the dots formed using the separate precursors are 2.5 ± 0.2 nm compared to 3.3 ± 0.3 nm for those formed with the MSCs. To confirm the interaction between the ZnS and InP clusters to form QDs, InP MSCs were thermalized in the absence of zinc

and sulfur as a control experiment. In the absence of $[Zn_{10}S_4(SPh)_{16}][N(Me)_4]_4$, large anisotropic InP was formed rather than spherical nanocrystals (Figure A4).

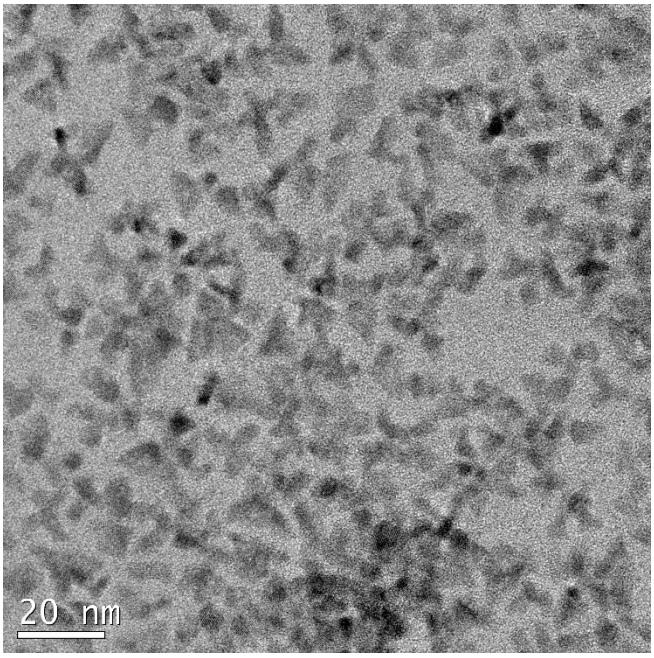

Figure A4. Large, anisotropic nanostructures formed by heatup of InP MSCs and myristic acid.

Based on these observations, compositional characterization was performed in order to elucidate whether the ZnS and InP react together to form an alloy (and to what degree of gradation), core-shell, or simply nucleate separately to give ZnS and InP particles. The use of powder X-ray diffraction measurements allows for comparison to literature structures of InP and ZnS. As seen in figure A5, the synthesized particle peaks are slightly shifted from the known bulk powder diffraction pattern peaks of both InP and ZnS. This deviation has been seen in the literature with alloyed systems, where the peaks of the material lie in between the peaks of the pure compounds consistent with Vegard's law.[12] This data is suggestive of alloying, but not conclusive.

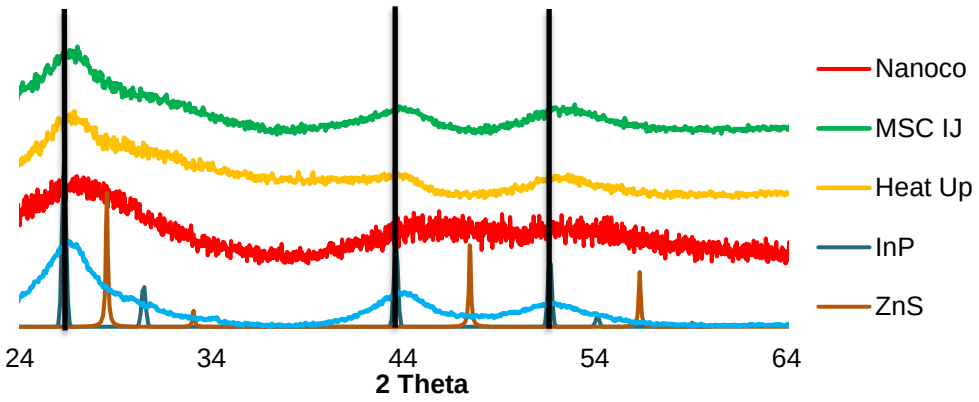

Figure A5. XRD patterns of quantum dots synthesized via the different methods. The shift in values of 2 theta suggests alloying of the materials. The lines are a visual aid and correspond to major InP peaks from reference bulk pattern (pdf 01-070-2513 ICSD). The ZnS reference pattern is pdf 01-071-5976 ICSD.

As shown in Table A4, ICP elemental analysis data confirmed that all samples contain indium, phosphorus, zinc, and sulfur. The ratios differ between the MSC methods and the Nanoco procedure, with the dots formed from the MSC significantly indium rich. All particles exhibit an approximate 1:1 ratio of Zn:S, but the amount of indium is highly variable. Due to the starting MSC stoichiometry, a roughly 50% excess of indium, when compared to phosphorus is present in syntheses using the MSCs as a precursor.

Table A4. Elemental ratios determined by ICP-AES for final materials generated from different InPZnS syntheses.

Element	Nanoco	MSC Heatup	MSC Injection
Indium	2.6	4.8	5.8
Zinc	1.3	0.8	1.1

Sulfur	1	1	1
Phosphorus	2.3	2.1	2.1

However, this does not correspond to the increase in indium content, which suggests that the structure of the QDs are different when prepared using the MSCs. This preliminary data suggests that the MSC-based syntheses lead to indium rich InP, whereas the Nanoco procedure leads to more stoichiometric particles. Additional structural data is needed to confirm this change and spectroscopic investigations will allow us to determine the implications of this difference with regards to the electronic structure of the particles.

Molecular clusters are commonly used as single source precursors for metal chalcogenide nanocrystals and several hypotheses for their effect on nucleation exist.[17] One is that the cluster remains intact and behaves as a monomer, another is that that the cluster completely decomposes into individual monomers, and finally that the cluster partially decomposes into a seed with smaller monomers present. Thus, a series of experiments was devised varying the concentration of ZnS cluster in order to determine the impact on the final particle size. It was indeed found that the initial amount of the $[Zn_{10}S_4(SPh)_{16}][N(Me)_4]_4$ cluster present in the reaction directly affects the final size of the quantum dot formed. As seen in figure A6, increasing the amount of the $[Zn_{10}S_4(SPh)_{16}][N(Me)_4]_4$ cluster decreases the dot size and vice versa.

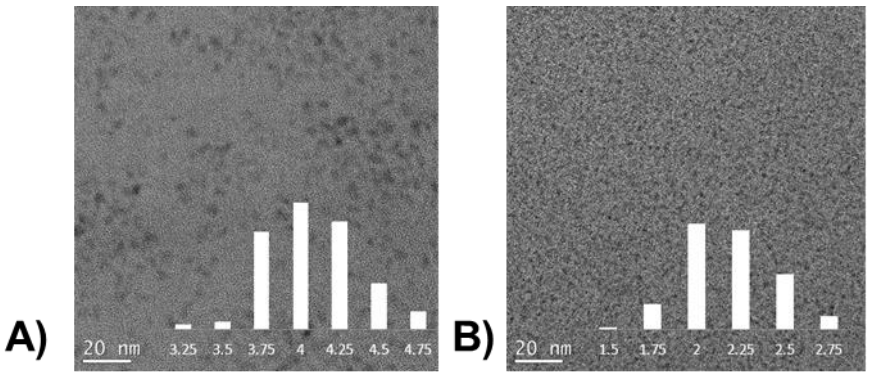

Figure A6. TEM images of particles synthesized with A) decreased and B) increased amounts of $[Zn_{10}S_4(SPh)_{16}][N(Me)_4]_4$.

This agrees with the expected result if the $[Zn_{10}S_4(SPh)_{16}][N(Me)_4]_4$ acts as a nucleation site; the lower concentration of cluster would result in fewer nuclei and larger particles. However, the final size of nanomaterials is controlled by a variety of factors and can be influenced by the processes of both nucleation and growth. Whether this effect is tied directly to the nucleation event or the growth of the particles is unclear with the data gathered at this point. What can be determined is that the $[Zn_{10}S_4(SPh)_{16}][N(Me)_4]_4$ cluster plays a vital role in the formation of the QDs. In order to determine whether or not InP particles would nucleate separately or if the cluster behaved similarly to the individual precursors, the multi injection nature of the Nanoco procedure was replicated at higher temperatures using the MSCs. When a second solution of InP MSCs was injected at 175 °C, no new particles were nucleated. Thus, the clusters exhibit similar behavior to the individual precursors when dispensed over multiple injections. Whether this is tied directly to the $[Zn_{10}S_4(SPh)_{16}][N(Me)_4]_4$ cluster or simply the presence of zinc and sulfur monomers has yet to be investigated.

A.3 CONLUSIONS OF INPZNS WORK

This work describes new synthetic methods targeting InPZnS alloyed QDs using InP MSCs as a single source precursor for both indium and phosphorus. The thermal stability of the MSC precursors allows for a heat-up synthesis of alloyed InPZnS quantum dots. Using the same amount of phosphorus as the two injection Nanoco procedure, the dual cluster method produces monodisperse, indium rich, and colloidally stable quantum dots of 3.4 ± 0.3 nm. When compared to the Nanoco procedure, the MSC QDs are larger with similar monodispersity and X-ray diffraction patterns. The primary noticeable difference is in the particle composition, with the MSC derived QDs being significantly more indium rich. Additional studies could be undertaken utilizing different sized ZnE nanoclusters or focused on shelling the previously mentioned materials to determine if the varied synthetic methods impacted the luminescence properties of the final quantum dots.

A.4 RESULTS AND DISCUSSION INPZNSE

The previous Nanoco-type approach is plagued by an inability to adequately tune the reactivities of either cluster. While the elemental ratios and number of potential nuclei can be altered by varying the concentrations of the respective clusters, this can be similarly accomplished with molecular precursors and the multi-cluster approach provides no significant advantage. However, the Owen lab developed a library of chalcogoureas with a wide range of known reactivities.[18,19] Using carefully selected thio- and selenoureas they were able to synthesize CdSeS nanocrystals with varying degrees of alloying based on the comparative reactivity of the anion precursor.[14]

With this as a guiding idea, I commenced work on synthesizing alloyed InPZnSe from molecular precursors. While thiourea sulfur precursors were also extensively described, the novelty of working with the selenium system, the better lattice match of ZnSe with InP, and smaller band gap shifted the focus of the work. The selenoureas necessary for this study are not commercially available and were thus synthesized according to literature procedures from selenium powder, amines, and isocyanides.[19] For this work I used TOPSe as a control and selected three selenoureas, named in order of increasing reactivity, to study – **1)** N'-cyclohexyl-N-ethyl-N-methylselenourea, **2)** N,N-dibutyl-N'-cyclohexylselenourea, and **3)** N-butyl-N'-cyclohexylselenourea. Initial experiments focused on heatup syntheses of individual molecular precursors (see scheme A1) based on literature reports for InPZnS.[9]

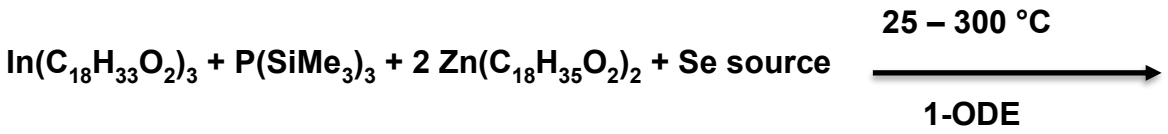

Scheme A1. General reaction scheme for InPZnSe heat up reaction.

While all selenium sources led to the formation of nanocrystals, minimal differences were seen in their size and optical features (Table A5). However, the TOPSe-derived material showed higher selenium incorporation than those derived from any selenourea, regardless of reactivity. In fact, no trends between reactivity and selenium content of the final materials could be obtained.

Table A5. Characterization of final nanocrystal products synthesized via a heat up method from different selenium precursors.

	TOPSe	1	2	3
LEET (nm)	462	468	469	463
PL maxima (nm)	520	520	530	525
QD size (nm)	3.6 ± 0.5	3.3 ± 0.3	3.7 ± 0.5	3.2 ± 0.5
Atom % Se	16	9	12	4

I attributed the lack of selenium incorporation to the well-known high reactivity of the molecular phosphorus precursor, $P(SiMe_3)_3$.[20] The presence of a highly active anionic species might gate the overall reactivity of the system and preclude any impact of the differing selenium reactivities. In order to potentially avoid this issue, I switched approaches to a synthesis via a slow injection of the $P(SiMe_3)_3$ into a hot reaction mixture of the rest of the precursors. The idea was that the slow introduction of $P(SiMe_3)_3$ into the reaction would allow the selenium reactivity to control monomer formation and thus the nucleation and growth of the final nanoparticles. Additionally, by starving the system of P^{3-}, the potential for nucleating pure InP would diminish. Unfortunately, once again minimal variations in selenium incorporation were observed for the selenoureas (Table A6).

Table A6. Selenium content of final nanomaterials synthesized via a slow injection of $P(SiMe_3)_3$ and various selenium precursors.

	TOPSe	1	3
Atom % Se	28	11	10

An additional issue with this approach was a lack of morphological control. In initial experiments at a growth temperature of 200 °C a mixture of spherical nanocrystals and large nanorods were observed via TEM, particularly evident in the selenourea-derived materials (Figure A7B). The nanostructures from TOPSe show an absence of large rods, but are small and anisotropic (Figure A7A). The mixed morphologies from the selenourea syntheses persisted across temperatures ranging from 150 °C to 300 °C, demonstrating the impossibility of thermally controlling morphology in this system.

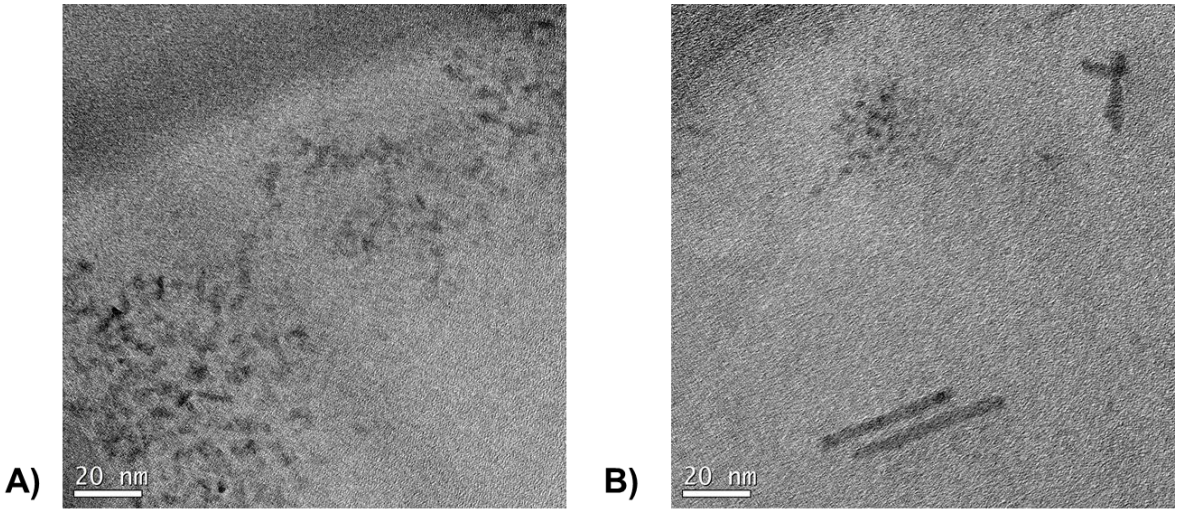

Figure A7. Nanostructures formed by slow addition of $P(SiMe_3)_3$ to zinc, selenium, and indium precursors with selenium source A)TOPSe and B) **)** N-butyl-N'-cyclohexylselenourea.

The level of anisotropy seen in these systems is intriguing as the traditional strongly coordinating ligands that promote rod growth, like phosphonates, are absent from the solution. This could be an effect of the decomposition of the selenourea, but other reports of nanocrystals synthesized from this class of precursors report no such issues.[14,18,19] Based on literature reports, though, it does seem like matching anionic precursor reactivity is extremely challenging even when operating in systems with analogous molecules.[14,21] The vastly different structures and

reactivities of the phosphorus and selenium precursors could create conditions that do not allow for control over nanocrystal properties in a rational way. Potential future work on a similar system could utilize a beautiful study published since the completion of this research to guide conditions and alternative precursors if desired.[14]

A.5 SELENOUREA CONCLUSIONS

Attempts to make a quaternary alloyed system with InPZnSe via selenoureas were met with mixed success. While I saw the incorporation of selenium via both heat up and slow injection methods, no trend based on precursor reactivity could be observed. Additionally, the slow injection method produced a mixture of nanostructure morphologies that could not be thermally controlled. Based on this work, I conclude that $P(SiMe_3)_3$ and the selenoureas used have incompatible reactivities for the synthesis of highly tunable alloyed nanoparticles.

A.6 EXPERIMENTAL

Sodium (dry stick, ACS reagent), potassium (in mineral oil, 98%), red phosphorus (99.999%), oleic acid (90%), indium acetate (99.99%) trimethylamine (≥99%), tetramethylammonium chloride (≥98%), zinc nitrate hexahydrate (98%), S_8 (99.5%), anhydrous acetonitrile (99.8%), methanol, and toluene were purchased from Sigma-Aldrich Chemical Company and used without further purification. Thiophenol (99%) was purchased from Acros and used without further purification. Omni Trace nitric acid was purchased from EMD Millipore and used without further purification. 18.2 MΩ water was collected from an EMD Millipore water purification system. Celite 545 was purchased from Sigma-Aldrich Chemical Company and heated at 150 ◦C under vacuum overnight and stored in a nitrogen filled inert glove box prior to

use. $P(SiMe_3)_3$ and $[Zn_{10}S_4(SPh)_{16}][N(Me)_4]_4$ were prepared according to literature procedures and stored in a nitrogen filled inert atmosphere glove box.[1,2] All solvents, including dioctyl terephthalate (≥96%), 1,2-dimethoxyethane (99%), and pentane were purchased from Sigma-Aldrich Chemical Company, dried by stirring overnight with CaH_2, distilled, and stored over 4 Å molecular sieves. C_6D_6 was purchased from Cambridge Isotope Labs and was similarly dried and stored. ^{1}H NMR spectra were collected on a 300 MHz Bruker Avance spectrometer. UV-Vis spectra were collected on a Cary 5000 spectrophotometer from Agilent. Powder XRD spectra were collected on a Bruker D8 Discover with GADDS 2-D XRD system. ICP-OES was performed using a Perkin Elmer Optima 8300. TEM images were collected on an FEI Tecnai G2 F20 microscope. TEM analysis was performed using manual analysis with the help of the ImageJ software package.[3] Unless noted, all syntheses were performed using air-free Schlenk techniques.

Synthesis of $In(C_{18}H_{34}O_2)_3$

In a typical synthesis 2.25 grams (7.74 mmol) of indium acetate and 7.15 g (25.3 mmol) of oleic acid were added to a flask and heated to 100°C overnight. The acetic acid was off-gassed and upon cooling under an inert atmosphere a colorless, gelatinous solid remained. The solid was then transferred to a glovebox.

Synthesis of $In_{37}P_{20}(C_{18}H_{34}O_2)_{51}$ magic sized clusters

In a typical synthesis 3.2766 g (11.6 mmol) of oleic acid and 0.93 g (3.20 mmol) of indium acetate were added to a 3-neck round bottom flask. The flask was then placed under vacuum and heated to 100 °C overnight to form indium oleate. The next morning the flask was filled with N_2 gas and 20 mL of dry toluene was injected to create a solution. In a glovebox, 465 µL of

$P(SiMe_3)_3$ (1.60 mmol) was added to 10 mL of dry toluene. The temperature of the indium oleate solution was then increased to 110 °C and the $P(SiMe_3)_3$ solution injected into it. The reaction was monitored by UV-Vis and allowed to proceed until no change in a characteristic peak at 386 nm was seen. The toluene was then removed under vacuum and the clusters brought into the glovebox for further purification. The clusters were dissolved in toluene, crashed out with acetonitrile, and centrifuged. This procedure was repeated until the NMR spectrum showed no significant free acid peak.

Modified Nanoco synthesis of InPZnS alloyed quantum dots

In a typical two injection synthesis, 0.3053 g of indium oleate (0.32 mmol) and 73 µL of $P(SiMe_3)_3$ (0.25 mmol) were individually dissolved in 0.75 mL of dioctyl terephthalate and stirred overnight. A dry solution of 0.0209 g of $[Zn_{10}S_4(SPh)_{16}][N(Me)_4]_4$ (0.007 mmol) and 0.0624 g (0.22 mmol) oleic acid in 2.5 mL of dioctyl terephthalate, which was then injected into a N_2 filled flask. The solution was heated to 90 °C and held there for 45 minutes. The temperature was then raised to 100 °C and the 0.25 mL of the solutions of first indium oleate then $P(SiMe_3)_3$ were slowly added to the reaction flask. The reaction progress was followed by UV-Vis spectroscopy. Once no change was seen in the spectra the temperature was increased to 160 °C and a second set of injections using the remaining solutions (0.5 mL) of indium oleate and $P(SiMe_3)_3$ were slowly injected before the temperature was further increased to 175 °C for particle growth. A red shift of the LEET of the dots was observed upon the second injection (see Figure 2). When no change was seen in the absorbance, the temperature of the reaction was lowered by 20 °C and the solution annealed for 48 hours. The reaction mixture was then cooled and brought into a glovebox for purification of the particles.

Injection synthesis of InPZnS alloyed quantum dots using InP MSCs

In a typical synthesis, a solution of 0.2406 g of $In_{37}P_{20}(C_{18}H_{34}O_2)_{51}$ magic sized clusters (MSCs) (0.013 mmol) were dissolved in 1.5 mL dioctyl terephthalate and stirred overnight. A dry solution of 0.0209 g of $[Zn_{10}S_4(SPh)_{16}][N(Me)_4]_4$ (0.007 mmol) and 0.0624 g oleic acid (0.22 mmol) in 2.5 mL of dioctyl terephthalate, which was then injected into a N_2 filled flask. The solution was heated to 90 °C and held there for 45 minutes. The temperature was then raised to 175 °C and the MSC solution slowly injected. The reaction progress was followed by UV-Vis spectroscopy. Once no change was seen in the spectra the temperature was decreased to 155 °C and the quantum dots annealed at that temperature for 48 hours. The reaction mixture was then cooled and brought into a glovebox for purification of the particles.

Heat-up synthesis of InPZnS alloyed quantum dots using InP MSCs

In a typical synthesis, a solution of 0.2406 g of $In_{37}P_{20}(C_{18}H_{34}O_2)_{51}$ magic sized clusters (0.013 mmol) were dissolved in 1.5 mL dioctyl terephthalate and stirred overnight. A dry solution of 0.0209 g of $[Zn_{10}S_4(SPh)_{16}][N(Me)_4]_4$ (0.22 mmol) and 0.0624 g oleic acid (0.007 mmol) in 2.5 mL of dioctyl terephthalate was combined with the MSC solution, then mixture was injected into a N_2 filled flask. The solution was heated to 90 °C and held there for 45 minutes. The temperature was then raised to 175 °C to decompose the MSCs and form the quantum dots. The reaction progress was followed by UV-Vis spectroscopy. Once no change was seen in the spectra the temperature was decreased to 155 °C and the quantum dots annealed at that temperature for 48 hours. The reaction mixture was then cooled and brought into a glovebox for purification of the particles.

InPZnS quantum dot workup procedure

The particles were crashed out from the reaction mixture using acetonitrile as the non-solvent and centrifuged. They were resuspended in toluene, crashed out with acetonitrile, and centrifuged. This procedure was repeated until no feature corresponding to the free acid peak was visible via NMR.

Synthesis of selenoureas

Equimolar (3 mmol) amounts of selenium powder, an isocyanide, and an amine were added to 3 mL toluene in a vial. The vial was taped up and removed from the glovebox. The solution was placed in a 100 ^{o}C oil bath and stirred for an hour, while the solution became homogenous and lightened in color. The solution was then brought back into the glovebox, filtered with a 0.45 μm syringe filter, and the toluene removed under vacuum. Specific purification procedures for each selenourea can be found in the supporting information of ref 19.[19]

InPZnSe quantum dot synthesis

For the heatup procedure, 0.05 mmol of indium oleate, the selenium source, zinc oleate, and $P(SiMe_3)_3$ were added to 4 mL ODE. The reaction mixture was heated to 300 °C and held at temperature until no further changes were seen in the optical spectra. The ODE was then removed via distillation and the QDs brought into the glovebox for purification. For the slow injection procedure, the zinc, selenium, and indium precursors were all heated to 200 °C in 3.5 mL of ODE. The $P(SiMe_3)_3$ was then dissolved in 0.5 mL ODE and slowly injected via a syringe

pump over a period of 10 mins. The reaction was allowed to proceed until no further changes in the optical spectra were seen and then purified as stated above.

Sample preparation for characterization

TEM: A 50/50 solution of pentane and toluene was used as the solvent. A few drops of the QD solution was added to this. The TEM grid was suspended and 1-2 drops was added and left to dry. The grid was put under vacuum overnight to remove any residual solvent. XRD: The suspended QDs were crashed out of solution and the solid was placed on a silicon wafer substrate. ICP: A small pipette tip of worked up particle solution was crashed out. The solvent was removed. Enough concentrated high purity nitric acid was added to dissolve the particles so the final solution could be diluted with 18.2 MΩ water in a volumetric flask to prepare a 2% nitric acid solution.

A.7 REFERENCES

(1) Kim, T.-H.; Jun, S.; Cho, K.-S.; Choi, B. L.; Jang, E. Bright and Stable Quantum Dots and Their Applications in Full-Color Displays. *MRS Bull.* **2013**, *38* (9), 712–720. https://doi.org/10.1557/mrs.2013.184.
(2) Talapin, D. V.; Steckel, J. Quantum Dot Light-Emitting Devices. *MRS Bull.* **2013**, *38* (9), 685–691. https://doi.org/10.1557/mrs.2013.204.
(3) Shirasaki, Y.; Supran, G. J.; Bawendi, M. G.; Bulović, V. Emergence of Colloidal Quantum-Dot Light-Emitting Technologies. *Nat. Photonics* **2013**, *7* (1), 13–23. https://doi.org/10.1038/nphoton.2012.328.
(4) Chen, O.; Wei, H.; Maurice, A.; Bawendi, M. G.; Reiss, P. Pure Colors from Core–Shell Quantum Dots. *MRS Bull.* **2013**, *38* (9), 696–702.
(5) Cui, J.; Beyler, A. P.; Marshall, L. F.; Chen, O.; Harris, D. K.; Wanger, D. D.; Brokmann, X.; Bawendi, M. G. Direct Probe of Spectral Inhomogeneity Reveals Synthetic Tunability of Single-Nanocrystal Spectral Linewidths. *Nat. Chem.* **2013**, *5*, 602–606.
(6) Janke, E. M.; Williams, N. E.; She, C.; Zherebetskyy, D.; Hudson, M. H.; Wang, L.; Gosztola, D. J.; Schaller, R. D.; Lee, B.; Sun, C.; et al. Origin of Broad Emission Spectra in InP Quantum Dots: Contributions from Structural and Electronic Disorder. *J. Am. Chem. Soc.* **2018**, *140* (46), 15791–15803. https://doi.org/10.1021/jacs.8b08753.
(7) Adam, S.; Talapin, D. V.; Borchert, H.; Lobo, A.; McGinley, C.; de Castro, A. R. B.; Haase, M.; Weller, H.; Moller, T. The Effect of Nanocrystal Surface Structure on the

Luminescence Properties: Photoemission Study of HF-Etched InP Nanocrystals. *J. Chem. Phys.* **2005**, *123*, 084706.
(8) Hughes, K. E.; Stein, J. L.; Friedfeld, M. R.; Cossairt, B. M.; Gamelin, D. R. Effects of Surface Chemistry on the Photophysics of Colloidal InP Nanocrystals. *ACS Nano* **2019**. https://doi.org/10.1021/acsnano.9b07027.
(9) Li, L.; Reiss, P. One-Pot Synthesis of Highly Luminescent InP/ZnS Nanocrystals without Precursor Injection. *J. Am. Chem. Soc.* **2008**, *130* (35), 11588–11589. https://doi.org/10.1021/ja803687e.
(10) Kim, T.; Kim, S. W.; Kang, M.; Kim, S.-W. Large-Scale Synthesis of InPZnS Alloy Quantum Dots with Dodecanethiol as a Composition Controller. *J. Phys. Chem. Lett.* **2012**, *3* (2), 214–218. https://doi.org/10.1021/jz201605d.
(11) Huang, K.; Demadrille, R.; Silly, M. G.; Sirotti, F.; Reiss, P.; Renault, O. Internal Structure of InP/ZnS Nanocrystals Unraveled by High-Resolution Soft X-Ray Photoelectron Spectroscopy. *ACS Nano* **2010**, *4* (8), 4799–4805. https://doi.org/10.1021/nn100581t.
(12) Regulacio, M. D.; Han, M.-Y. Composition-Tunable Alloyed Semiconductor Nanocrystals. *Acc. Chem. Res.* **2010**, *43* (5), 621–630. https://doi.org/10.1021/ar900242r.
(13) Pickett, N.; Naasani, I.; Harris, J. Semiconductor Nanoparticle-Based Materials. 8,957,401 B2.
(14) Hamachi, L. S.; Yang, H.; Jen-La Plante, I.; Saenz, N.; Qian, K.; Campos, M. P.; Cleveland, G. T.; Rreza, I.; Oza, A.; Walravens, W.; et al. Precursor Reaction Kinetics Control Compositional Grading and Size of CdSe1−xSx Nanocrystal Heterostructures. *Chem Sci* **2019**, *10* (26), 6539–6552. https://doi.org/10.1039/C9SC00989B.
(15) Gary, D. C.; Flowers, S. E.; Kaminsky, W.; Petrone, A.; Li, X.; Cossairt, B. M. Single-Crystal and Electronic Structure of a 1.3 Nm Indium Phosphide Nanocluster. *J. Am. Chem. Soc.* **2016**, *138* (5), 1510–1513. https://doi.org/10.1021/jacs.5b13214.
(16) Gary, D. C.; Terban, M. W.; Billinge, S. J. L.; Cossairt, B. M. Two-Step Nucleation and Growth of InP Quantum Dots via Magic-Sized Cluster Intermediates. *Chem. Mater.* **2015**, *27* (4), 1432–1441. https://doi.org/10.1021/acs.chemmater.5b00286.
(17) Cumberland, S. L.; Hanif, K. M.; Javier, A.; Khitrov, G. A.; Strouse, G. F.; Woessner, S. M.; Yun, C. S. Inorganic Clusters as Single-Source Precursors for Preparation of CdSe, ZnSe, and CdSe/ZnS Nanomaterials. *Chem. Mater.* **2002**, *14* (4), 1576–1584. https://doi.org/10.1021/cm010709k.
(18) Hendricks, M. P.; Campos, M. P.; Cleveland, G. T.; Jen-La Plante, I.; Owen, J. S. A Tunable Library of Substituted Thiourea Precursors to Metal Sulfide Nanocrystals. *Science* **2015**, *348* (6240), 1226. https://doi.org/10.1126/science.aaa2951.
(19) Campos, M. P.; Hendricks, M. P.; Beecher, A. N.; Walravens, W.; Swain, R. A.; Cleveland, G. T.; Hens, Z.; Sfeir, M. Y.; Owen, J. S. A Library of Selenourea Precursors to PbSe Nanocrystals with Size Distributions near the Homogeneous Limit. *J. Am. Chem. Soc.* **2017**, *139* (6), 2296–2305. https://doi.org/10.1021/jacs.6b11021.
(20) Gary, D. C.; Glassy, B. A.; Cossairt, B. M. Investigation of Indium Phosphide Quantum Dot Nucleation and Growth Utilizing Triarylsilylphosphine Precursors. *Chem. Mater.* **2014**, *26* (4), 1734–1744. https://doi.org/10.1021/cm500102q.
(21) Smith, D. K.; Luther, J. M.; Semonin, O. E.; Nozik, A. J.; Beard, M. C. Tuning the Synthesis of Ternary Lead Chalcogenide Quantum Dots by Balancing Precursor Reactivity. *ACS Nano* **2011**, *5* (1), 183–190. https://doi.org/10.1021/nn102878u.

VITA

Marja Elizabeth "Beth" Mundy grew up in rural North Carolina and received a B.S. in chemistry from Davidson College before spending a year in Finland on a Fulbright fellowship. During her time at UW she served as president of Women in Chemical Sciences – UW and is a current Science Communication Fellow at the Pacific Science Center. She has written articles for the Royal Society of Chemistry as a blogger on the *Chem. Comm.* and *Chem. Sci*. blogs. When not in the lab, she can be found most frequently with her nose in a book, sipping a cup of tea, or doing both simultaneously.